Telesurgery and Surgical Simulation: Design, Modeling, and Evaluation of Haptic Interfaces to Real and Virtual Surgical Environments

by

Murat Cenk Çavuşoğlu

B.S. (Middle East Technical University, Ankara, Turkey) 1995
M.S. (University of California, Berkeley) 1997

A dissertation submitted in partial satisfaction of the
requirements for the degree of
Doctor of Philosophy

in

Engineering — Electrical Engineering and Computer Sciences

in the

GRADUATE DIVISION
of the
UNIVERSITY of CALIFORNIA at BERKELEY

Committee in charge:

Professor S. Shankar Sastry, Chair
Professor Frank Tendick
Professor Brian Barsky
Professor Andrew Packard

Fall 2000

The dissertation of Murat Cenk Çavuşoğlu is approved:

Chair Date

Date

Date

Date

University of California at Berkeley

Fall 2000

Telesurgery and Surgical Simulation: Design, Modeling, and Evaluation of Haptic Interfaces to Real and Virtual Surgical Environments

Abstract

Telesurgery and Surgical Simulation: Design, Modeling, and Evaluation of Haptic Interfaces to Real and Virtual Surgical Environments

by

Murat Cenk Çavuşoğlu

Doctor of Philosophy in Engineering — Electrical Engineering and Computer Sciences

University of California at Berkeley

Professor S. Shankar Sastry, Chair

In this thesis, telesurgery and surgical simulation are treated as parallel research problems of haptic interfacing to real and virtual surgical environments, respectively. The analytical tools of systems and control theory and robotics are used to address several research problems in these areas.

The work on telesurgery is centered around the UC Berkeley/UC San Francisco Laparoscopic Telesurgical Workstation, focusing on the design and analysis of the system, with details of the design specifications, solution of the forward and inverse kinematics, and control issues. This is followed by a discussion on the general issues on the testing of the system. A novel approach using open surgical suturing motion data to evaluate the kinematics of a robotic telesurgical manipulator without prototyping a physical system is proposed within this context.

High fidelity teleoperation controller design for the telesurgical system is studied, and a theoretical and experimental framework is established for design and evaluation of teleoperation controllers for telemanipulation of deformable objects. In this study, the teleoperator control design is specifically for manipulation of deformable objects and uses a task based optimization scheme which explicitly takes into account human perceptual capabilities for the task at hand, telesurgery and stiffness discrimination. Integrated with this control design approach, two quantitative methods to analytically compare sensory schemes for teleoperators are proposed and a new experimental methodology to evaluate

teleoperation control algorithms is presented for a stiffness discrimination task.

Dynamic simulation of deformable objects for interactive virtual environments is explored with emphasis on formulation of the problem, enabling technologies, and various modeling methods in the literature, mostly focusing on putting the existing methodologies into a unifying framework.

Finally, the problem of high fidelity haptic interaction with deformable objects in virtual environments is studied from a control theory point of view. A novel method to interface with deformable objects addressing the issues resulting from the difference between the haptic and deformable model simulation update rates is motivated, developed, and analyzed using the tools of modern control theory.

Professor S. Shankar Sastry
Dissertation Committee Chair

Dedicated to Charles A. Desoer and Lawrence W. Stark,
my academic "grandfathers"...

Contents

List of Figures

List of Tables

Acknowledgements

I would like to express my sincere appreciation to my advisor Prof. S. Shankar Sastry, for his invaluable support and advice, and to my co-advisor Prof. Frank Tendick, for his help and guidance at every step of my research. I also would like to thank to Prof. Brian Barsky and Prof. Andy Packard for the advice they provided.

I would like to thank to Alana Sherman, who was a great research partner during the work on the design of teleoperation control algorithms and conducting experiments to evaluate teleoperation controllers. I am grateful to Joseph Yan, David Feygin, Yi Ma, and John Koo, for their collaboration and fruitful comments throughout the time. I also would like to thank colleagues and *friends* at the Robotics and Intelligent Machines Laboratory of UC Berkeley, for the pleasant working environment. This list includes the following people: Lauren Bentley, Matt Danning, Neel Dhruv, Michael Downes, Dmitry Derevyanko, Tolga Göktekin, Gunnar Proppe, Omid Shakernia, Metin Sitti, Isela Villenueva, Dr. Winthrop Williams, and Xunlei Wu (please forgive me if I left anybody out).

I owe gratitude to Prof. Ron Fearing for his advice throughout my Master's and PhD work.

Special thanks go to Erica Morrison and Peter Ray in the ERL office, and Ruth Gjerde and Mary Byrnes in the department graduate office for all the administrative help. I really couldn't have survived without their help.

I would like to express my appreciation to Lawrence W. Way, MD, the head of the Department of Surgery at the University of California, San Francisco, and surgical fellows there: Karen Whang, MD, Hirofumi Yamada, MD, and David Suh, MD.

I also would like to thank colleagues at the SHARP group of INRIA Rhone-Alpes, especially Deigo d'Aulignac, Dr. Sepanta Sekhavat, Anton Deuget, and Dr. Christian Laugier.

Last, but not least, I want to express my thanks to my parents, who encouraged and helped me to continue to pursue my dreams in this *New World*.

This research would not have been accomplished without the generous financial support from the National Science Foundation under grants IRI-95-31837 and CISE CDA 9726362, the Office of Naval Research under MURI grant N14-96-1-1200, the Army Research Office under MURI grant DaaH04-96-1-0341, the National Aeronautics and Space Administration under STTR grant NAS1-20288, and the France-Berkeley Fund.

Chapter 1

Introduction

Medical robotics and computer assisted surgery (MRCAS) is an emerging area of research on the application of computers and robotic technology to surgery, in planning and execution of surgical operations and in training of surgeons.

Telesurgery and surgical simulation are the two areas of MRCAS on which this thesis focuses. With robotic telesurgery, the goal is to develop robotic tools to augment or replace hand instruments used in surgery. In robotic telesurgery, the robotic tools are not automated robots but teleoperated systems under direct control of the surgeon, therefore giving the name *tele*surgery. Surgical simulation aims to develop an alternate training medium for surgery in the form of a virtual environments based surgical training simulator. This is similar to using flight simulators to train pilots.

Both of these will be discussed in the context of minimally invasive surgery (MIS), particularly laparoscopic surgery (minimally invasive surgery of the abdomen).

What is Laparoscopic Surgery ?

Laparoscopic surgery is a revolutionary technique [103]. It is minimally invasive, i.e., the surgery is performed with instruments and viewing equipment inserted through small incisions (less than 10mm in diameter) rather than by making a large incision to expose and provide access to the operation site. The main advantage of this technique is the reduced trauma to healthy tissue, which is the leading cause of patients' post-operative pain and long hospital stay. The hospital stay and rest periods, and therefore the procedure costs, can be significantly reduced with MIS, but MIS procedures are more demanding on

the surgeon, requiring more difficult surgical techniques.

Minimally invasive operations include laparoscopy (abdominal cavity), thoracoscopy (chest cavity), arthroscopy (joints), pelviscopy (pelvis), and angioscopy (blood vessels). The first major laparoscopic surgery, for cholecystectomy (removal of the gall bladder), was performed in 1985 by Mühe in (West) Germany. In less than a decade, there was a quick shift from open surgery to laparoscopic surgery for relatively simple procedures, with 67% of cholecystectomies performed laparoscopically in the US in 1993 [38]. Adoption of laparoscopic techniques has been slower in more complex procedures, largely because of the greater difficulty due to the surgeon's reduced dexterity and perception.

In laparoscopic surgery, the abdominal cavity, which is expanded by pumping carbon dioxide inside to open a workspace, is observed with a laparoscope inserted through one of the incisions. The laparoscope itself is composed of a chain of lens optics to transmit the image of the operation site to the CCD camera connected to its outer end, and optical fibers to carry light to illuminate inside. A monoscopic image of the operation site is displayed on a high resolution CRT screen. The instruments used for the operation are specially designed long and thin instruments with trigger-like handles. They are inserted through trocars placed at the incisions to air seal the abdomen. The instruments have only 4 degrees of freedom (DOF) (see Fig. 1.1), preventing the ability to arbitrarily orient the instrument tip [97]. Dexterity is significantly reduced because of the lost DOF's and motion reversal due to the fulcrum at the entry point. Force feedback is reduced due to the friction at the air tight trocar and the stiffness of the inflated abdominal wall. There is no tactile sensing, on which surgeons highly depend in open surgery to locate arteries and tumors hidden in tissue.

MIS also has problems related to spatial perception. In MIS, the surgeons look at, and interact with, the anatomy from a completely different perspective than they are used to. In open surgery, the operation site is at arm's length, and the visual and motor spaces are consistent. However, in MIS, the surgeon literally views the anatomy from inside through a camera, and the camera is controlled by an assistant who acts like the eyes of the surgeon. Visual and motor spaces are no longer consistent, since the surgeon watches the operation site on a CRT screen placed at a geometrically unrelated location, and the display covers a considerably smaller field of view relative to the eyes of the surgeon than the field of view of the camera. These conditions, in addition to the complications of a typical surgical scene, result in difficulties in spatial perception, particularly in identifying anatomical landmarks,

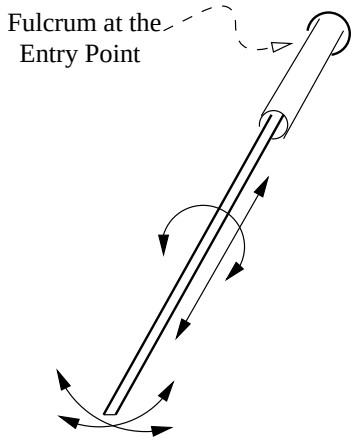

Figure 1.1: 4 DOF available in conventional laparoscopic instruments

navigating in the anatomy, planning for proper exposure, and handling the camera and instruments.

1.1 Telesurgical System Concept

Minimally invasive surgery is fundamentally telemanipulation as the surgeon is physically separated from the workspace. Therefore, telerobotics is a natural tool to extend capabilities in laparoscopic surgery. The surgical tools can be replaced with robotic instruments which are under direct control of the surgeon through teleoperation. (Fig. 1.2)

With the telesurgical workstation, the goal is to restore the manipulation and sensation capabilities of the surgeon which were lost due to minimally invasive surgery. A 6 DOF slave manipulator, controlled through a spatially consistent and intuitive master, will restore the dexterity, the force feedback to the master will increase the fidelity of the manipulation, and the tactile feedback will restore the lost tactile sensation.

Other telesurgical systems in the literature for abdominal surgery include the telesurgical system for open surgery with 4 DOF manipulators developed at SRI International [45] (a laparoscopic version has also been developed), the telerobotic assistant for laparoscopic surgery developed by Taylor et.al. [93], the Black Falcon manipulator by Madhani et.al. [66], and the telesurgery experiments performed between JPL, California and Polytechnic University of Milan, Italy [81], and between Nagoya and Tokyo in Japan [5]. Also, there are two commercial companies, Computer Motion Inc., Goleta, CA, and Intu-

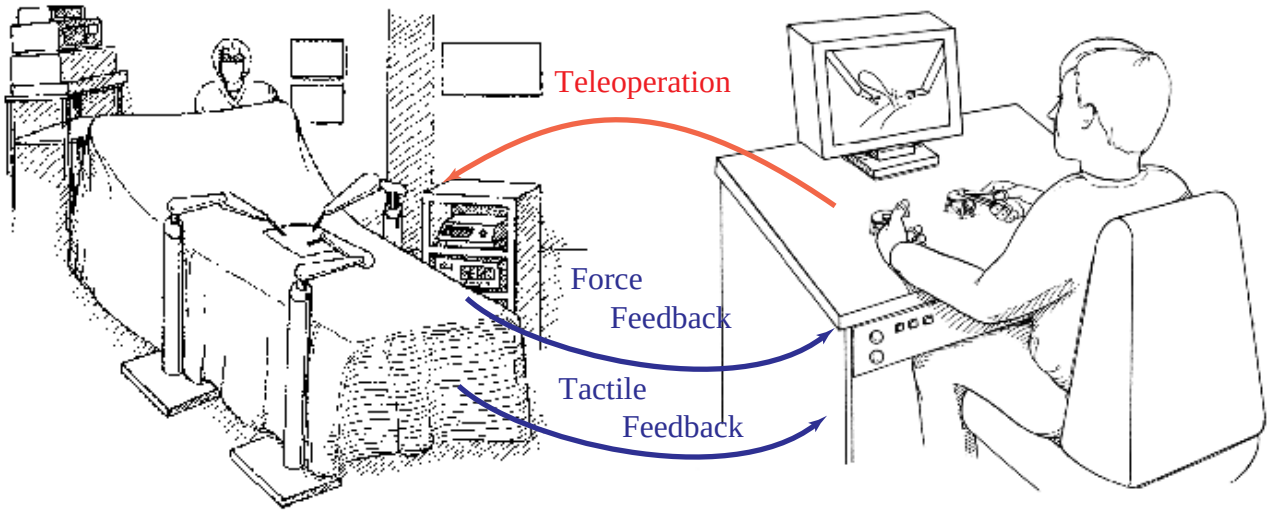

Figure 1.2: Telesurgical system concept

itive Surgical Inc., Palo Alto, CA, which are developing telesurgical systems intended for minimally invasive cardiac surgery as well as laparoscopy. Systems of both companies are currently in the human testing stage.

It is important to mention at this point that there are other successful medical applications of robotics. These include the ROBODOC system for orthopedic surgery [95], which is an autonomous robotic system to perform total hip replacement surgery, the image guided robotic system for micro-surgery and stereotactic neurosurgery developed by Lavallée et.al. [60], the high precision manipulator for micro surgery (eye surgery in particular) developed at NASA Jet Propulsion Laboratory [89], and the image guided planning system for robotic radiotherapy [100]. See [28, 94] for good reviews.

The research problems in the development of a telesurgical system are manipulator design and achieving high fidelity teleoperation. Telesurgical manipulators need to be small, 10 mm or smaller for laparoscopy, and 5 mm or smaller for cardiac and fetal surgery, yet have significant workspace and apply forces in the range of several Newtons to be able to manipulate tissue. At this scale, transmission of sufficient mechanical power is the main challenge. Design of haptic interfaces, 6 DOF, lightweight, high bandwidth manipulators with workspace in the range of several liters[1] and with at least 4 DOF, preferably 6 DOF, force feedback, which will serve as master devices, is another active research area.

[1] 1 liter=1000 cm^3

Telesurgical tasks require high dexterity and fidelity during manipulation since most of the manipulation is delicate. Therefore, the design requirements for the teleoperation controllers are significantly different from classical teleoperation applications. An important component of the teleoperator design is the quantification of the human operator sensitivity and performance. This is necessary in terms of providing the specifications of the controller as well as measures to evaluate designs.

Tactile sensing and display technology is an active research area [21, 39, 34, 72, 58, 77, 104]. Tactile sensors are at a level mature enough for application, however, tactile displays are not currently at the necessary scale.

1.2 Surgical Simulator Concept

Surgeons are trained through apprenticeship. The basic techniques are taught with simple training equipment, but the rest of the training is either with books describing surgical procedures and techniques, or in the operating room by watching and participating in actual operations, and rarely in the animal laboratories. Although actual operating room training is essential and invaluable, it does not provide the optimal environment to try or practice new techniques and procedures due to the risks to the patient. This method of training also limits the diffusion of knowledge since only a limited number of people can be trained by one experienced surgeon.

Virtual environments present an alternative to this training scheme. With virtual environments it is possible to create an interactive 3D simulation environment, where the surgeons, using a haptic interface, can manipulate, cut, or suture dynamically and geometrically correct models of organs and tissues simulated on a computer (Fig. 1.3). The idea is similar to using flight simulators to train pilots. Virtual environments provide an environment where there is no risk to a patient and therefore less stressful. They are interactive and 3D in contrast to books, and they are relatively inexpensive compared to training in the operating room or animal labs. Virtual environments also give a unique advantage, as it is possible to generate arbitrary anatomies and pathologies with which the surgeons can be trained for cases that they will encounter only a few times during their whole career but nonetheless must be trained for. This way, it is also possible to standardize the training and accreditation in surgery.

There are many research groups working on virtual environments for surgical train-

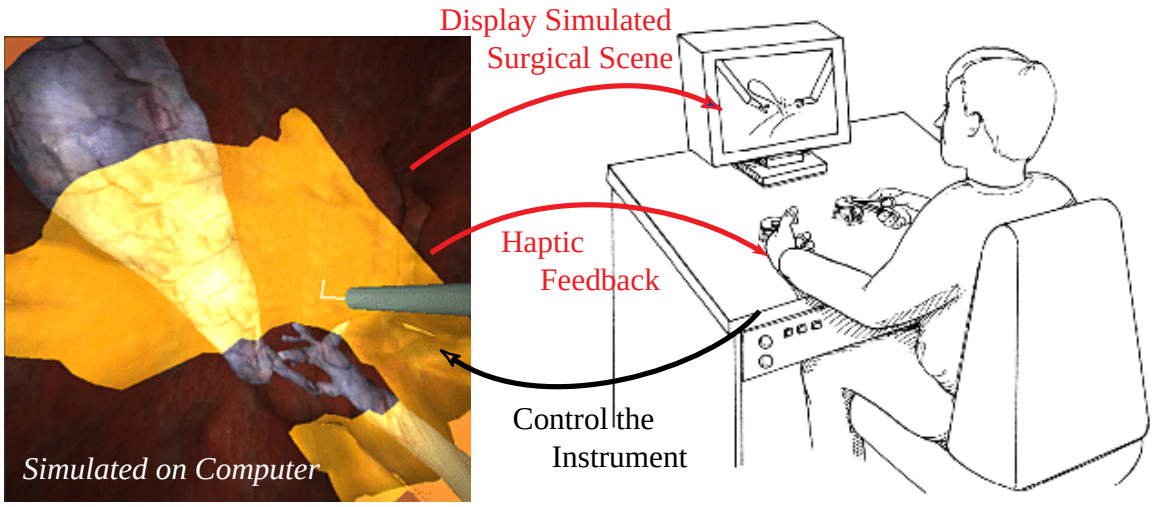

Figure 1.3: Surgical training simulator concept

ing. These studies include surgical training simulators for laparoscopic surgery [59, 92], endoscopy of the colon [7, 47] and sinus [107], arthroscopy [37, 73, 68, 87], bronchoscopy [14], endoscopic retrograde cholangio-pancreatography (ERCP) [76], retinal laser photocoagulation [33], phacoemulsification of cataracts [86], and spinal biopsy and nerve blocks [9, 19].

The existing successful training simulators are for applications where there are not large deformations, and mostly manipulation of hard objects. But, for other applications, deformable models are required, and the state of the art for interactive deformable object simulation is not sufficiently advanced to build realistic real-time simulations. Constructing realistic and efficient deformable models for soft tissue behavior is the main challenge in achieving realism in surgical training simulators. The deformable tissue models have to be interactive, efficient enough to be simulated in real time, visually and haptically realistic, and able to be cut and sutured.

The surgical training simulators in the literature are mostly for MIS applications. This is not a coincidence. In addition to the need for better training tools for MIS, the constraints which make MIS difficult are the same reasons that make building simulators for MIS more manageable with existing technology. It is significantly easier to imitate the user interface for MIS, limited and well constrained haptic interaction and limited amount and quality of feedback (visual and otherwise) available.

It is also necessary to determine what to teach in the simulator. It is possible to train basic motor skills, such as using surgical instruments, suturing, and knot tying. It is also possible to train spatial skills, including navigation, exposure, and camera handling skills. Finally, it is also possible to teach surgical tasks and complete procedures.

Verification of the transfer of skills from virtual surgery, i.e. simulator, to real surgery is an important piece of the puzzle. It is obviously important that the skills learned from the simulator are not skills in a new computer game, but rather skills transferable to actual surgery. However, there are only a few studies in the literature which actually studied the transfer of skills form a surgical simulator to real surgery.

1.3 Telesurgery and Surgical Simulation as Haptic Interfacing to Real and Virtual Surgical Environments

At first, the development of a robotic telesurgical system and a virtual environments based surgical simulator may seem to be unrelated areas. But, in fact, they are two parallel problems as illustrated in Fig. 1.4.

Surgery is inherently a form of haptic interaction. During surgery the surgeon is in physical interaction with the patient either with his hands or through the instruments he uses. In the telesurgical system, the operator interacts with the master manipulator, which controls the slave robot through a teleoperation algorithm, to interact with the real surgical environment on the remote site. In the surgical training simulator, the operator again uses the master haptic interface, this time to interact with a simulated virtual environment. Therefore, telesurgery and surgical simulation are problems of developing haptic interfaces to real and virtual surgical environments.

From a systems engineering point of view, the development of a telesurgical system and a surgical training simulator are parallel problems. They require similar design and analysis methodologies, and there are similar or overlapping problems. Tools and results of one can be applied to the other. We can see these corresponding aspects of the two applications more clearly in Fig. 1.4.

Psychophysics It is important to identify the relevant psychophysical parameters of the human operator. The telesurgical system is augmenting the human operator, therefore it is necessary to know the engineering specification of the underlying system, i.e. the

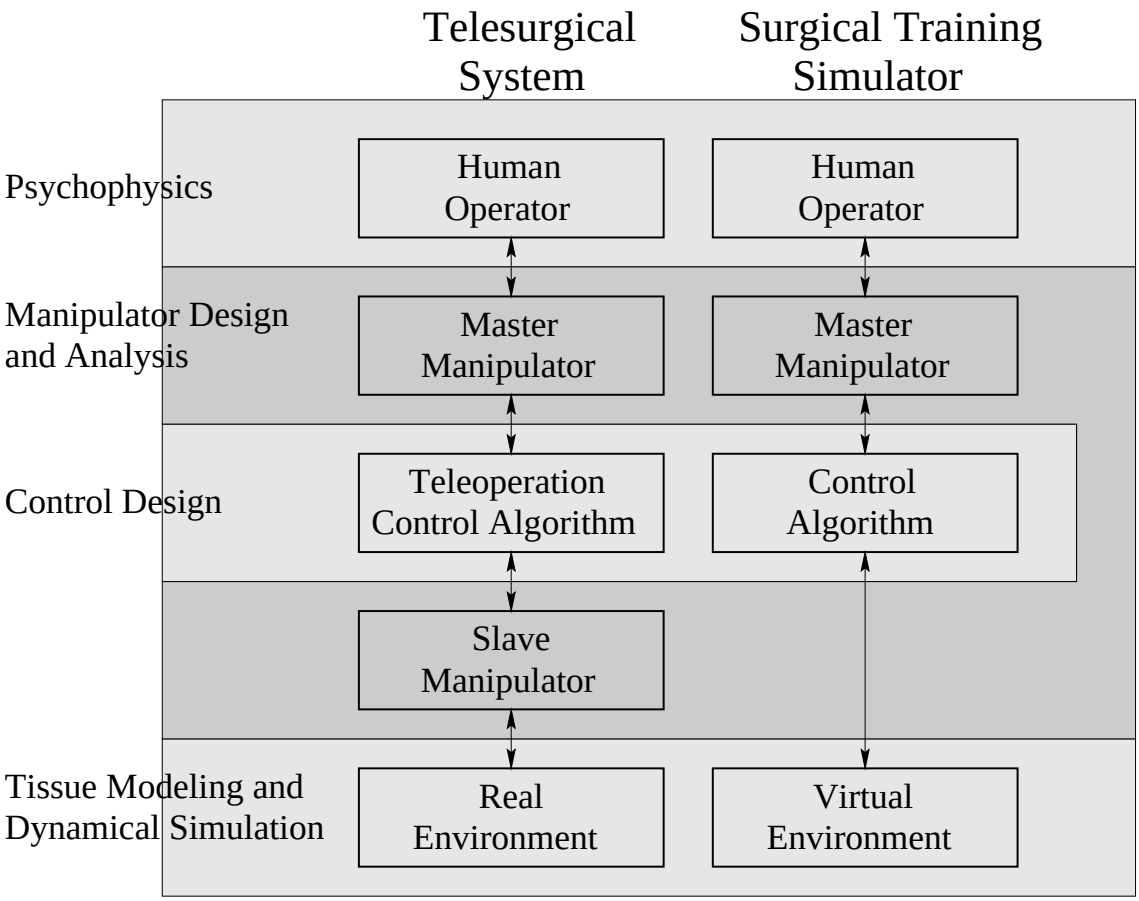

Figure 1.4: Telesurgery and surgical simulation are parallel research problems.

human, such as the frequency dependent force and impedance sensitivities. The same psychophysical quantities are also important for the surgical simulator, since they determine the level of accuracy necessary in the simulation to achieve the desired level of realism.

Manipulator Design and Analysis The same requirements apply for the master manipulator of the telesurgical system and the haptic interface of the surgical simulator. Both need to display interaction forces of the same magnitude and bandwidth, require similar fidelity and similar workspace. Essentially, they will be interfaces for interaction to similar environments, apart from the fact that the former will be used for interacting with a real surgical environment, whereas the latter will be used for interacting with a virtual surgical environment. This parallelism extends to the design of the slave manipulator of the telesurgical system as well.

Control Design Teleoperation controller design for the telesurgical system and

the control of the haptic interface of the surgical simulator are essentially two aspects of the same problem. The only difference is that, in telesurgery, the remote environment is real, resulting in an unstructured system with uncertainties, and in surgical simulation, the remote environment is simulated, resulting in a different set of problems from the discrete nature of the simulation and computational requirements. The same analysis and design tools of control theory are used in addressing these problems.

Tissue Modeling and Dynamical Simulation One of the main problems of the surgical simulator is the development of realistic physical models of the organs and soft tissue. Construction of these models require data from the real tissue to determine the mechanical properties. Also, knowing the physical properties of the tissue to be manipulated is important for the design and control of the telesurgical system.

1.4 Contributions

The main research contribution in this dissertation is the application of the analytical tools of systems and control theory and robotics to several of the research items shown in Fig. 1.4.

Bilateral control design for high fidelity telemanipulation of soft objects is one of the main focus areas. Telemanipulation of soft objects has not been previously studied in the literature. In this study, the teleoperator control design is specifically for manipulation of deformable objects and uses a task-based optimization scheme which explicitly takes into account human perceptual capabilities for the task at hand, telesurgery and stiffness discrimination. This distinguishes our approach from the work in the literature on teleoperation. Integrated with this control design approach, two quantitative methods to analytically compare sensory schemes for teleoperators are proposed, and a new experimental methodology to evaluate teleoperation control algorithms human-in-the-loop is presented for a stiffness discrimination task.

Human interfacing to deformable objects in virtual environments is another focus of this thesis. A novel method to interface with deformable objects addressing the issues resulting from the difference between the haptic and deformable model simulation update rates is motivated, developed, and analyzed using the tools of modern control theory, namely order reduction methodology.

The kinematic analysis and basic experimental evaluation of the UC Berkeley

(UCB)/UC San Francisco(UCSF) Robotic Telesurgical Workstation (RTW) are also presented in this thesis. General issues on the testing of the system are discussed, and a novel approach using open surgical suturing motion data to evaluate the kinematics of a robotic telesurgical manipulator without prototyping a physical system is proposed.

Finally, dynamic simulation of deformable objects for interactive virtual environments is explored with emphasis on formulation of the problem, enabling technologies, and a critical look at the various modeling methods in the literature.

1.5 Dissertation Outline

The topics in this thesis are broadly divided into two parts : telesurgery and surgical simulation. The work on telesurgery is centered around the UCB/UCSF Laparoscopic Telesurgical Workstation. Chapter 2 focuses on the design and analysis of the system, with details of the design specifications, solution of the forward and inverse kinematics, and control issues. This is followed by a discussion on the experimental evaluation of the laparoscopic telesurgical workstation in chapter 3. The last chapter in this part (chapter 4) is on high fidelity teleoperation controller design for the telesurgical system. In this chapter, a theoretical and experimental framework is developed for design and evaluation of teleoperation controllers for telemanipulation of deformable objects.

The second part of the thesis focuses on surgical simulation. Chapter 5 discusses the general problems in dynamical simulation of deformable objects, with a critical look at the existing methodologies in the literature. It is mostly focused on formulating the problem and putting the existing methodologies into a unifying framework. Chapter 6 addresses the problem of high fidelity haptic interaction with deformable objects in virtual environments from a control theory point of view.

Finally, chapter 7 discusses the future research directions in telesurgery and surgical simulation.

Part I

Telesurgery

Chapter 2

The Robotic Telesurgical Workstation

In this joint project between the Robotics and Intelligent Machines Laboratory of the University of California, Berkeley (UCB) and the Department of Surgery of the University of California San Francisco (UCSF), a robotic telesurgical workstation for laparoscopy is being developed. The current design is a bimanual system with two 6 DOF manipulators instrumented with grippers, controlled by a pair of 6 DOF master manipulators.

To justify the cost and overhead of using a non-conventional and complicated tool, a robotic telesurgical workstation (RTW) has to either improve existing procedures or enable the surgeons to perform operations previously not possible. The target tasks chosen in the design of the UCB/UCSF RTW are suturing and knot tying, which are very difficult to perform with existing laparoscopic tools. This is mainly due to the lack of ability to orient the tip of the tools and the difficulties in hand-eye coordination. This makes many advanced abdominal procedures extremely difficult to be performed laparoscopically. Therefore, the design of the system is oriented explicitly towards easy suturing and knot tying.

This chapter will introduce the UCB/UCSF RTW, with emphasis on design specifications, give the detailed kinematic analysis of the slave manipulator, solution of the inverse and forward kinematics, and briefly discuss the control issues.

2.1 Description of the System

The current system is a second generation system, designed for extensive operating room testing in animal experiments as well as testing with *ex vivo* tissue and in training box. Its goal is to verify the concept, i.e., to show that using teleoperated 6 DOF slave manipulators, it is possible to improve dexterity and sensation in laparoscopic surgery, and therefore, improve the surgeons' performance and enable them to perform previously impossible surgical operations.

Previous research on medical robotics at UC Berkeley includes the development of an endoscopic manipulator [106, 105], early designs of millirobotic manipulators for laparoscopy [20], and the first generation laparoscopic telesurgical workstation [17, 16]. The first generation prototype was completed in 1997 and tested in *ex vivo* suturing and knot tying experiments.

2.1.1 Design Requirements

The goal of the design of the slave manipulators is to add a 2 DOF wrist to extend the 4 DOF available through the fulcrum, and therefore give enough dexterity to perform complex skills, especially suturing and knot tying, in the minimally invasive setting. The slave must be small enough to fit through incisions typically 10 mm wide, but also able to apply forces large enough to manipulate tissue and suture. It must have sufficient workspace to span significant regions in the abdominal cavity and suture at almost arbitrary orientations, yet have a wrist short enough in length to work in constrained spaces. System bandwidth should permit natural motions by the surgeon and haptic feedback with sufficient fidelity. Of course, the system must be safe to be used inside a patient.

Performance goals in the design of the millirobot are given in Table 2.1.[1] These values are estimated for a suturing task, force and movement requirements for driving a needle through tissue and tying a knot. The diameter of the instrument is chosen to fit the standard 10 mm and 15 mm diameter trocars. It is preferable not to have larger diameters as it causes greater damage to healthy tissue. For laparoscopic surgery, it is not necessary to go smaller than 10 mm, and use of a 15 mm instrument is acceptable as there are other instruments, for example staplers, that require a 15 mm trocar. Smaller diameters may be necessary or beneficial for other forms of minimally invasive surgery. For example, for min-

[1] Courtesy of Endorobotics Inc.

Table 2.1: Performance goals for the millirobot

Parameter	**Value**
Dimension: overall diameter	10–15 mm max
Dimension: wrist joint to grasper	50 mm max
Force: at the point of needle, for driving the needle through tissue	1.5 N min
Torque: about grasper axis, for driving needle (assumes curved needle, 15 mm from grasper to needle tip)	100 N-mm min
Torque: wrist flexion (yaw)	300 N-mm min
Force: gripping, while driving needle	40 N min
Range of motion: gripper jaw opening	8 mm min
Range of motion: rotation about grasper axis, to drive plus allowance for inclined work surface	270 degrees min
Range of motion: wrist flexion, for driving needle	90 degrees min
Range of motion: wrist pronation	720 degrees min
Speed: Grasper, full close in	0.5 sec max
Speed: Wrist roll	540 degrees/sec min
Speed: Wrist flexion	360 degrees/sec min
Bandwidth	5 Hz min
Lifetime	6 months min

imally invasive cardiac surgery, the instruments need to be able to go through the ribs, also pediatric laparoscopy and fetal surgery require smaller instruments. The wrist-to-gripper length is determined by the clearance between the abdominal wall and the key organs when the abdomen is pressurized. Torque and force requirements are estimated from measurements on instruments performing suturing in an open surgical setting. 270 degrees of roll rotation is required for driving the needle through tissue in a single movement without regrabbing it. 90 degrees of wrist flexion with 360 degrees of gross rotation is necessary for suturing at the desired orientations. 720 degrees of gross rotation is desirable for comfortable operation, reducing the need to readjust the instrument. The speed and bandwidth requirements are set to accommodate the bandwidth of intentional hand movements.

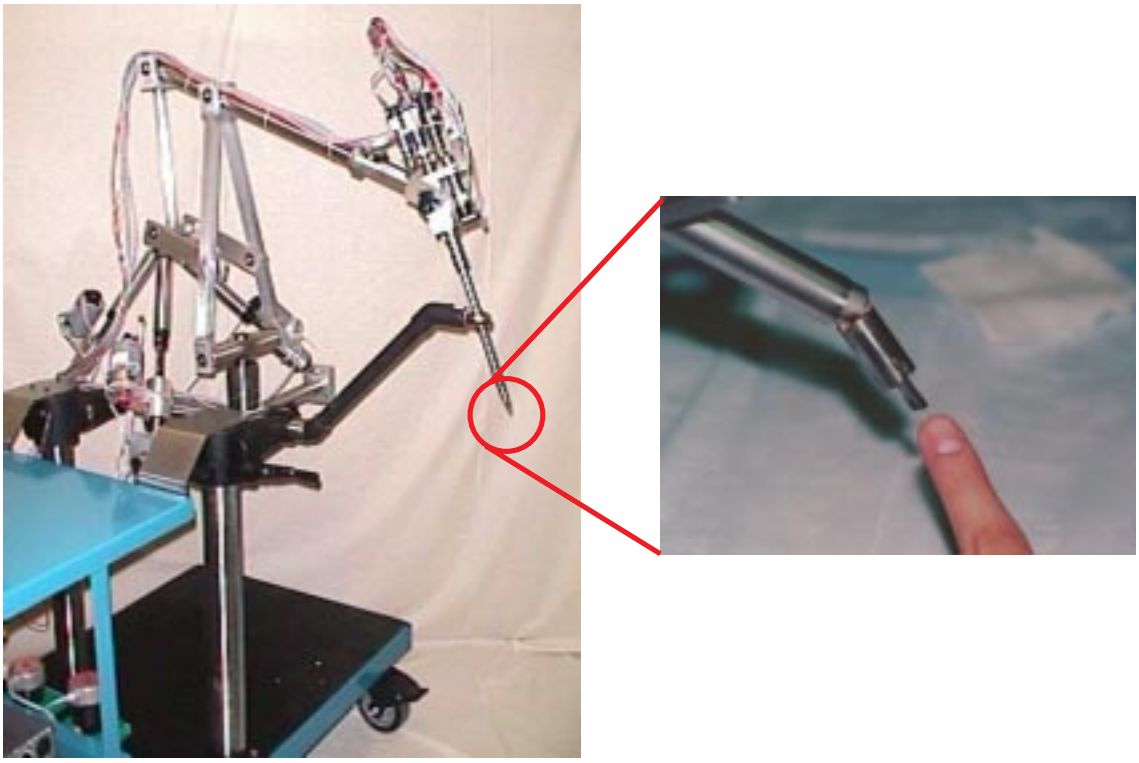

Figure 2.1: Slave manipulator of the UCB/UCSF laparoscopic telesurgical workstation. Close-up view of the millirobotic wrist is shown on the right.

2.1.2 Current Prototype

To meet the design requirements, the slave manipulator is composed of two parts (Fig. 2.1). The first part is the gross positioning stage located outside the body. It is responsible for positioning the millirobot, which is the second part of the slave robot. The gross stage controls the same 4 DOF as those available in conventional laparoscopic instruments. As the gross stage is located outside the body, there is not a tight space limitation. A parallel arrangement is chosen for increased rigidity and a small footprint. Three linear joints, which are connected to the base of the robot with U-joints, control the position of one end of a four-bar linkage. The tool arm and the motors actuating the gross rotation and the millirobot are connected to the opposite end of the four-bar linkage. All four actuators of the gross positioning stage are DC servo motors. In the linear joints, power is transmitted by lead screws connected to the motors. The roll axis through the entry port is tendon driven.

The second part of the slave, the millirobot, is located inside the patient and

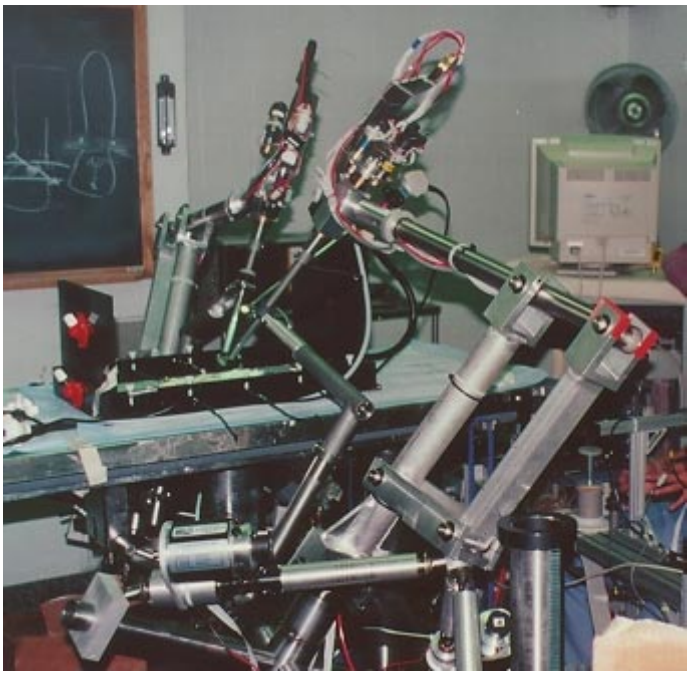

Figure 2.2: Setup of the bimanual system around the operating table.

consequently must be small yet capable of producing a wide range of motion and relatively large forces. To meet these requirements, it has a 2 DOF wrist, with yaw and roll axis rotations, and a gripper (Fig. 2.1). It is 15 mm in diameter. The wrist-to-gripper length is 5 cm. The yaw and roll axes are coupled and actuated with tendons jointly by three DC servo motors located on the end of tool arm outside the body.

Fig. 2.2 illustrates the positioning of the bimanual system in the operating room. The two slave manipulators are located at the opposite sides of the operating table. Fig. 2.3 shows the close-up view of the millirobotic section while tying a knot. Here, it is possible to see the advantage of having the 2 DOF wrist on the slave which makes it possible to have the nice approach angle and the opposing configuration of the two tools.

The master workstation (See Fig. 2.4) is composed of a pair of 6 DOF haptic interfaces, each controlling one of the slave manipulators. Commercial 6 DOF force reflecting haptic interfaces (Phantom v1.5, Sensable Technologies Inc., Cambridge, MA) with 3 actuated DOF are modified to be kinematically similar to the wrist configuration of the slave manipulators. This is to avoid control problems which would arise because of the wrist singularity and relieve the operator from the burden of dealing with unintuitive behavior

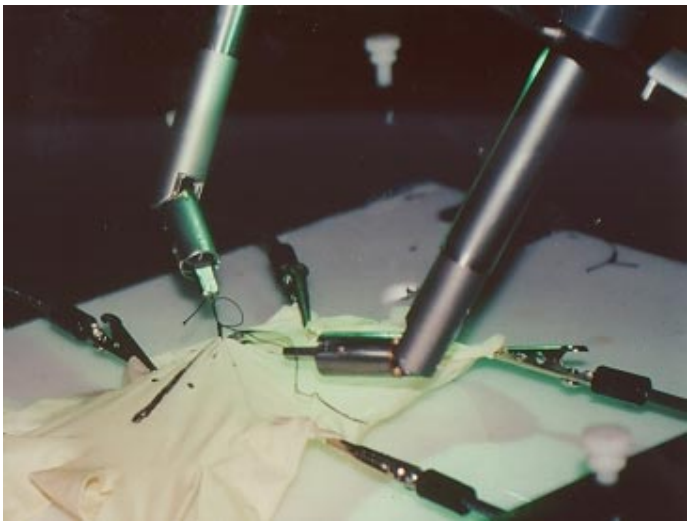

Figure 2.3: Close-up view of the bimanual system tying a knot in the training box.

of the manipulators around the singularity. The master interfaces are also equipped with a stylus handle to give a more dextrous interface for precise manipulation.

The major safety feature present in this prototype of the system is the heartbeat check by the robot. The robot continuously monitors a heartbeat signal sent by the control program, and cuts the power from all of the actuators in case this signal is lost, which means a computer failure.

2.2 Kinematics

For feedforward control of the system, the inverse kinematics of the slave manipulator and the forward kinematics of the master manipulator are needed. Forward kinematics of the slave are also necessary for position error based force feedback. In the following two sections, the details of the solution of the inverse and forward kinematics of the slave manipulator are presented.

In the specifications of the kinematic configuration of the robot, the product of exponentials formulation is used. Appendix A gives a brief summary of the product of exponentials formulation and the notation used. Refer to [74] for a full treatment of this formulation. The subproblems referenced in the text below are the Paden-Kahan subproblems which can also be found in [74].

Figure 2.4: Master workstation of the RTW.

2.3 Solution of the Inverse Kinematics

The inverse kinematics of a robot determine the joint angles of the actuated joints of the manipulator given the desired configuration of the end effector g_{md}. (Here we will assume that the desired configuration is expressed in the fulcrum coordinate frame.)

To simplify the inverse kinematics calculations, slave kinematics can be divided into two parts: the serial part inside the body and parallel part outside the body (Fig. 2.5). The serial part is composed of the fulcrum, which is modeled with a spherical joint and a translational joint, and the 2 DOF wrist. The parallel part of the slave consists of the tool arm passing through the fulcrum, the four-bar linkage configuration carrying the tool arm, and the three legs holding the opposite end of the four-bar linkage. Solution of the inverse kinematics of the millirobot is rather straightforward, since it has a very standard serial structure. However, the gross positioning stage has an unusual parallel structure.

In the inverse kinematics calculations, first the serial part needs to be solved, which gives the angles of the wrist joints and the desired configuration of the parallel part. Then the parallel part is solved to calculate the lengths of the linear joints and the tool

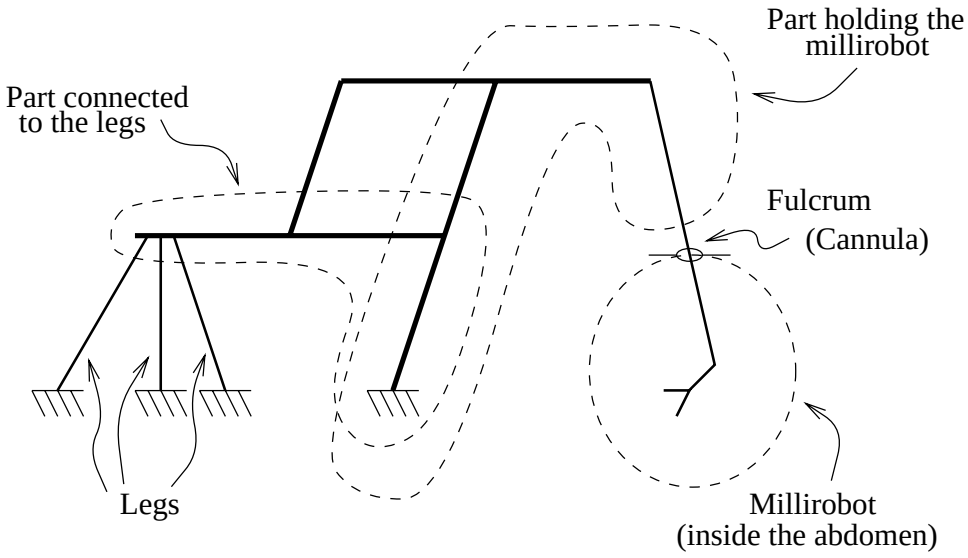

Figure 2.5: Kinematic diagram of the slave manipulator.

arm rotation. The solution of the parallel part is done in three steps. First, the inverse kinematics of the part of the four-bar linkage holding the millirobot is solved to calculate the amount of gross rotation, the angle of the four-bar linkage, and the amount of base rotations, which in turn are used to calculate the location and orientation of the legs by using the forward kinematics of the part of the four-bar linkage connected to the legs. Finally, the extensions of the linear joints at the legs are calculated by solving the inverse kinematics of the legs.

2.3.1 Millirobot

Kinematics of the millirobot can be represented with the following twists and zero configuration (Fig. 2.6):

$$\xi_{m1} = \begin{bmatrix} 0 & 0 & 0 & 1 & 0 & 0 \end{bmatrix}^T \tag{2.1}$$

$$\xi_{m2} = \begin{bmatrix} 0 & 0 & 0 & 0 & 1 & 0 \end{bmatrix}^T \tag{2.2}$$

$$\xi_{m3} = \begin{bmatrix} 0 & 0 & 0 & 0 & 0 & -1 \end{bmatrix}^T \tag{2.3}$$

$$\xi_{m4} = \begin{bmatrix} 0 & 0 & -1 & 0 & 0 & 0 \end{bmatrix}^T \tag{2.4}$$

$$\xi_{m5} = \begin{bmatrix} 0 & 0 & 0 & 1 & 0 & 0 \end{bmatrix}^T \tag{2.5}$$

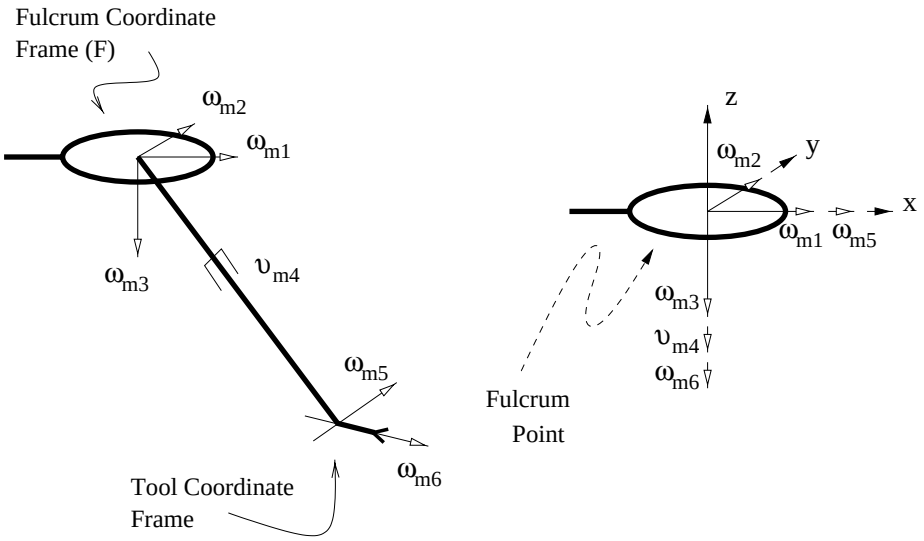

Figure 2.6: Naming convention and the zero configuration of millirobot.

$$\xi_{m6} = \begin{bmatrix} 0 & 0 & 0 & 0 & 0 & -1 \end{bmatrix}^T \tag{2.6}$$

$$g_m(0) = I_{4\times 4} \tag{2.7}$$

The ω_1, ω_2, ω_3 rotations and v_4 translation represent the ball joint at the entry port. This kinematic configuration is the inverse of the Stanford manipulator. We start with defining the point

$$p_{m1} = \begin{bmatrix} 0 & 0 & 0 & 1 \end{bmatrix}^T \tag{2.8}$$

Then, we proceed by inverting the forward kinematics map

$$e^{\hat{\xi}_{m1}\theta_{m1}} e^{\hat{\xi}_{m2}\theta_{m2}} e^{\hat{\xi}_{m3}\theta_{m3}} e^{\hat{\xi}_{m4}\theta_{m4}} e^{\hat{\xi}_{m5}\theta_{m5}} e^{\hat{\xi}_{m6}\theta_{m6}} I_{4\times 4} = g_{md} \tag{2.9}$$

$$e^{-\hat{\xi}_{m6}\theta_{m6}} e^{-\hat{\xi}_{m5}\theta_{m5}} e^{-\hat{\xi}_{m4}\theta_{m4}} e^{-\hat{\xi}_{m3}\theta_{m3}} e^{-\hat{\xi}_{m2}\theta_{m2}} e^{-\hat{\xi}_{m1}\theta_{m1}} = g_{md}^{-1} \tag{2.10}$$

$$e^{-\hat{\xi}_{m6}\theta_{m6}} e^{-\hat{\xi}_{m5}\theta_{m5}} e^{-\hat{\xi}_{m4}\theta_{m4}} e^{-\hat{\xi}_{m3}\theta_{m3}} e^{-\hat{\xi}_{m2}\theta_{m2}} e^{-\hat{\xi}_{m1}\theta_{m1}} p_{m1} = g_{md}^{-1} p_{m1} \tag{2.11}$$

$$e^{-\hat{\xi}_{m6}\theta_{m6}} e^{-\hat{\xi}_{m5}\theta_{m5}} e^{-\hat{\xi}_{m4}\theta_{m4}} p_{m1} = g_{md}^{-1} p_{m1} \tag{2.12}$$

$$e^{-\hat{\xi}_{m6}\theta_{m6}} e^{-\hat{\xi}_{m5}\theta_{m5}} e^{-\hat{\xi}_{m4}\theta_{m4}} p_{m1} - p_{m1} = g_{md}^{-1} p_{m1} - p_{m1} \tag{2.13}$$

$$e^{-\hat{\xi}_{m6}\theta_{m6}} e^{-\hat{\xi}_{m5}\theta_{m5}} (e^{-\hat{\xi}_{m4}\theta_{m4}} p_{m1} - p_{m1}) = g_{md}^{-1} p_{m1} - p_{m1} \tag{2.14}$$

$$\left| e^{-\hat{\xi}_{m6}\theta_{m6}} e^{-\hat{\xi}_{m5}\theta_{m5}} (e^{-\hat{\xi}_{m4}\theta_{m4}} p_{m1} - p_{m1}) \right| = \left| g_{md}^{-1} p_{m1} - p_{m1} \right| \tag{2.15}$$

$$\left| e^{-\hat{\xi}_{m4}\theta_{m4}} p_{m1} - p_{m1} \right| = \left| g_{md}^{-1} p_{m1} - p_{m1} \right| \tag{2.16}$$

which can be solved with Paden-Kahan subproblem 5 to calculate θ_{m4}. Once θ_{m4} is known, we can define

$$p_{m2} = e^{-\hat{\xi}_{m4}\theta_{m4}} p_{m1} \tag{2.17}$$

and continue with (2.12)

$$e^{-\hat{\xi}_{m6}\theta_{m6}} e^{-\hat{\xi}_{m5}\theta_{m5}} e^{-\hat{\xi}_{m4}\theta_{m4}} p_{m1} = g_{md}^{-1} p_{m1} \tag{2.18}$$

$$e^{-\hat{\xi}_{m6}\theta_{m6}} e^{-\hat{\xi}_{m5}\theta_{m5}} p_{m2} = g_{md}^{-1} p_{m1} \tag{2.19}$$

This can be solved using subproblem 2 to find θ_{m5} and θ_{m6}, which are respectively the yaw and roll angles of the millirobot. Subproblem 2 yields two solutions, but only one of them is mechanically possible, since the yaw axis of the millirobot can bend only in one direction, i.e. $0 \leq \theta_{m5} \leq \pi$. We do not need to solve the remaining angles of the millirobot explicitly, since only the term

$$e^{\hat{\xi}_{m1}\theta_{m1}} e^{\hat{\xi}_{m2}\theta_{m2}} e^{\hat{\xi}_{m3}\theta_{m3}} e^{\hat{\xi}_{m4}\theta_{m4}} = g_{md} e^{-\hat{\xi}_{m6}\theta_{m6}} e^{-\hat{\xi}_{m5}\theta_{m5}} \tag{2.20}$$

is required for the parallel part kinematics.

2.3.2 Parallel Part

We will proceed with solving the inverse kinematics of the part of the four-bar linkage which holds the millirobot. The kinematics of this segment are given by the following twists and zero configuration, all expressed with respect to the base coordinate frame (Fig. 2.7).

$$\xi_{t1} = \begin{bmatrix} 0 & 0 & 0 & 0 & 0 & 1 \end{bmatrix}^T \tag{2.21}$$

$$\xi_{t2} = \begin{bmatrix} 0 & 0 & 0 & 0 & 1 & 0 \end{bmatrix}^T \tag{2.22}$$

$$\xi_{t3} = \begin{bmatrix} -d_1 & 0 & 0 & 0 & 1 & 0 \end{bmatrix}^T \tag{2.23}$$

$$\xi_{t4} = \begin{bmatrix} 0 & d_1 & 0 & 1 & 0 & 0 \end{bmatrix}^T \tag{2.24}$$

$$\xi_{t5} = \begin{bmatrix} -d_1 & 0 & d_2 & 0 & 1 & 0 \end{bmatrix}^T \tag{2.25}$$

$$\xi_{t6} = \begin{bmatrix} 0 & -d_2 & 0 & 0 & 0 & 1 \end{bmatrix}^T \tag{2.26}$$

$$g_t(0) = \begin{bmatrix} & & d_2 \\ & I_{3\times 3} & 0 \\ & & d_1 \\ 0 & & 1 \end{bmatrix} \tag{2.27}$$

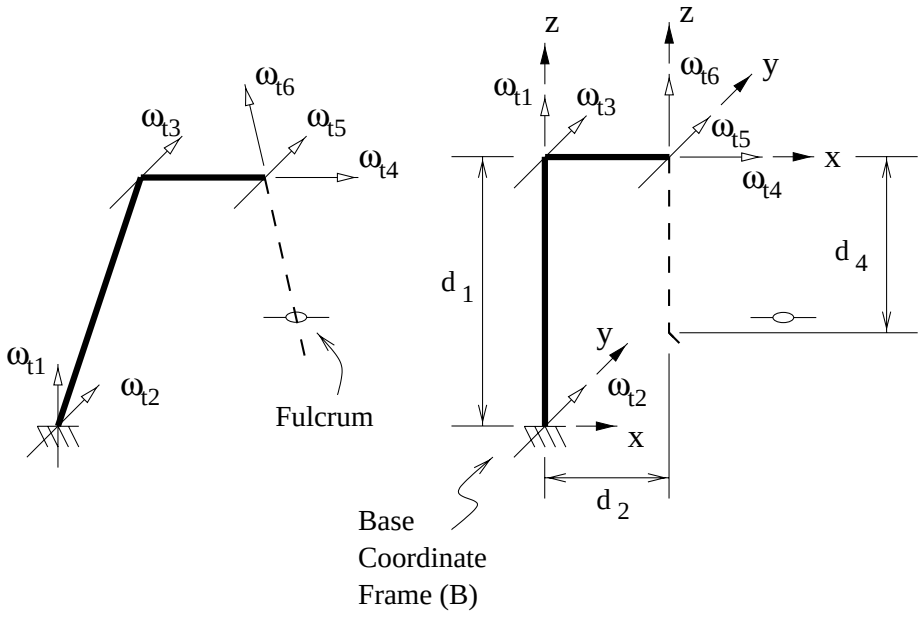

Figure 2.7: Naming convention and the zero configuration for the part of gross positioning stage which holds the millirobot.

The desired configuration of this segment is determined from the millirobot solution as

$$g_{td} = g_{BF} e^{\hat{\xi}_{m1}\theta_{m1}} e^{\hat{\xi}_{m2}\theta_{m2}} e^{\hat{\xi}_{m3}\theta_{m3}} e^{\hat{\xi}_{m4}\theta_{m4}} \begin{bmatrix} & & 0 \\ & I_{3\times 3} & 0 \\ & & d_4 \\ 0 & & 1 \end{bmatrix} \tag{2.28}$$

where g_{BF} is the coordinate transformation from the fulcrum coordinate frame (F) to the base coordinate frame (B). Then, the solution of the inverse kinematics of this segment follows as:

$$p_{t1} = \begin{bmatrix} 0 & 0 & 0 & 1 \end{bmatrix}^T \tag{2.29}$$

$$p_{t2} = \begin{bmatrix} d_2 & 0 & d_1 & 1 \end{bmatrix}^T \tag{2.30}$$

$$e^{\hat{\xi}_{t1}\theta_{t1}} e^{\hat{\xi}_{t2}\theta_{t2}} e^{\hat{\xi}_{t3}\theta_{t3}} e^{\hat{\xi}_{t4}\theta_{t4}} e^{\hat{\xi}_{t5}\theta_{t5}} e^{\hat{\xi}_{t6}\theta_{t6}} g_t(0) = g_{td} \tag{2.31}$$

$$e^{\hat{\xi}_{t1}\theta_{t1}} e^{\hat{\xi}_{t2}\theta_{t2}} e^{\hat{\xi}_{t3}\theta_{t3}} e^{\hat{\xi}_{t4}\theta_{t4}} e^{\hat{\xi}_{t5}\theta_{t5}} e^{\hat{\xi}_{t6}\theta_{t6}} = g_{td} g_t^{-1}(0) \tag{2.32}$$

$$e^{\hat{\xi}_{t1}\theta_{t1}} e^{\hat{\xi}_{t2}\theta_{t2}} e^{\hat{\xi}_{t3}\theta_{t3}} e^{\hat{\xi}_{t4}\theta_{t4}} e^{\hat{\xi}_{t5}\theta_{t5}} e^{\hat{\xi}_{t6}\theta_{t6}} p_{t2} = g_{td} g_t^{-1}(0) p_{t2} \tag{2.33}$$

$$e^{\hat{\xi}_{t1}\theta_{t1}} e^{\hat{\xi}_{t2}\theta_{t2}} e^{\hat{\xi}_{t3}\theta_{t3}} p_{t2} = g_{td} g_t^{-1}(0) p_{t2} \tag{2.34}$$

$$e^{\hat{\xi}_{t1}\theta_{t1}}e^{\hat{\xi}_{t2}\theta_{t2}}e^{\hat{\xi}_{t3}\theta_{t3}}p_{t2} - p_{t1} = g_{td}g_t^{-1}(0)p_{t2} - p_{t1} \quad (2.35)$$

$$e^{\hat{\xi}_{t1}\theta_{t1}}e^{\hat{\xi}_{t2}\theta_{t2}}(e^{\hat{\xi}_{t3}\theta_{t3}}p_{t2} - p_{t1}) = g_{td}g_t^{-1}(0)p_{t2} - p_{t1} \quad (2.36)$$

$$\left|e^{\hat{\xi}_{t1}\theta_{t1}}e^{\hat{\xi}_{t2}\theta_{t2}}(e^{\hat{\xi}_{t3}\theta_{t3}}p_{t2} - p_{t1})\right| = \left|g_{td}g_t^{-1}(0)p_{t2} - p_{t1}\right| \quad (2.37)$$

$$\left|e^{\hat{\xi}_{t3}\theta_{t3}}p_{t2} - p_{t1}\right| = \left|g_{td}g_t^{-1}(0)p_{t2} - p_{t1}\right| \quad (2.38)$$

Subproblem 3 gives two solutions for θ_{t3}, only one of which is mechanically feasible. If we define

$$p_{t3} = e^{\hat{\xi}_{t3}\theta_{t3}}p_{t2} \quad (2.39)$$

(2.34) becomes

$$e^{\hat{\xi}_{t1}\theta_{t1}}e^{\hat{\xi}_{t2}\theta_{t2}}p_{t3} = g_{td}g_t^{-1}(0)p_{t2} \quad (2.40)$$

which can be solved by using subproblem 2, yielding two solutions for $(\theta_{t1}, \theta_{t2})$ pair, again only one of which is mechanically possible. Then we proceed as

$$e^{\hat{\xi}_{t1}\theta_{t1}}e^{\hat{\xi}_{t2}\theta_{t2}}e^{\hat{\xi}_{t3}\theta_{t3}}e^{\hat{\xi}_{t4}\theta_{t4}}e^{\hat{\xi}_{t5}\theta_{t5}}e^{\hat{\xi}_{t6}\theta_{t6}} = g_{td}g_t^{-1}(0) \quad (2.41)$$

$$e^{\hat{\xi}_{t4}\theta_{t4}}e^{\hat{\xi}_{t5}\theta_{t5}}e^{\hat{\xi}_{t6}\theta_{t6}} = e^{-\hat{\xi}_{t3}\theta_{t3}}e^{-\hat{\xi}_{t2}\theta_{t2}}e^{-\hat{\xi}_{t1}\theta_{t1}}g_{td}g_t^{-1}(0) \quad (2.42)$$

$$p_{t4} = \begin{bmatrix} d_2 & 0 & 0 & 1 \end{bmatrix}^T \quad (2.43)$$

$$e^{\hat{\xi}_{t4}\theta_{t4}}e^{\hat{\xi}_{t5}\theta_{t5}}e^{\hat{\xi}_{t6}\theta_{t6}}p_{t4} = e^{-\hat{\xi}_{t3}\theta_{t3}}e^{-\hat{\xi}_{t2}\theta_{t2}}e^{-\hat{\xi}_{t1}\theta_{t1}}g_{td}g_t^{-1}(0)p_{t4} \quad (2.44)$$

$$e^{\hat{\xi}_{t4}\theta_{t4}}e^{\hat{\xi}_{t5}\theta_{t5}}p_{t4} = e^{-\hat{\xi}_{t3}\theta_{t3}}e^{-\hat{\xi}_{t2}\theta_{t2}}e^{-\hat{\xi}_{t1}\theta_{t1}}g_{td}g_t^{-1}(0)p_{t4} \quad (2.45)$$

where subproblem 2 gives two solutions for $(\theta_{t4}, \theta_{t5})$ pair, with one mechanically possible solution.

$$e^{\hat{\xi}_{t6}\theta_{t6}} = e^{-\hat{\xi}_{t5}\theta_{t5}}e^{-\hat{\xi}_{t4}\theta_{t4}}e^{-\hat{\xi}_{t3}\theta_{t3}}e^{-\hat{\xi}_{t2}\theta_{t2}}e^{-\hat{\xi}_{t1}\theta_{t1}}g_{td}g_t^{-1}(0) \quad (2.46)$$

$$e^{\hat{\xi}_{t6}\theta_{t6}}p_{t1} = e^{-\hat{\xi}_{t5}\theta_{t5}}e^{-\hat{\xi}_{t4}\theta_{t4}}e^{-\hat{\xi}_{t3}\theta_{t3}}e^{-\hat{\xi}_{t2}\theta_{t2}}e^{-\hat{\xi}_{t1}\theta_{t1}}g_{td}g_t^{-1}(0)p_{t1} \quad (2.47)$$

Subproblem 1 can be used to solve the only remaining unknown θ_{t6}, which is the gross rotation.

The kinematics of the part of the four-bar linkage connected to the legs is given by the following twists expressed in the base coordinate frame (Fig. 2.8).

$$\xi_{b1} = \begin{bmatrix} 0 & 0 & 0 & 0 & 0 & 1 \end{bmatrix}^T \quad (2.48)$$

$$\xi_{b2} = \begin{bmatrix} 0 & 0 & 0 & 0 & 1 & 0 \end{bmatrix}^T \quad (2.49)$$

$$\xi_{b3} = \begin{bmatrix} -d_3 & 0 & 0 & 0 & 1 & 0 \end{bmatrix}^T \quad (2.50)$$

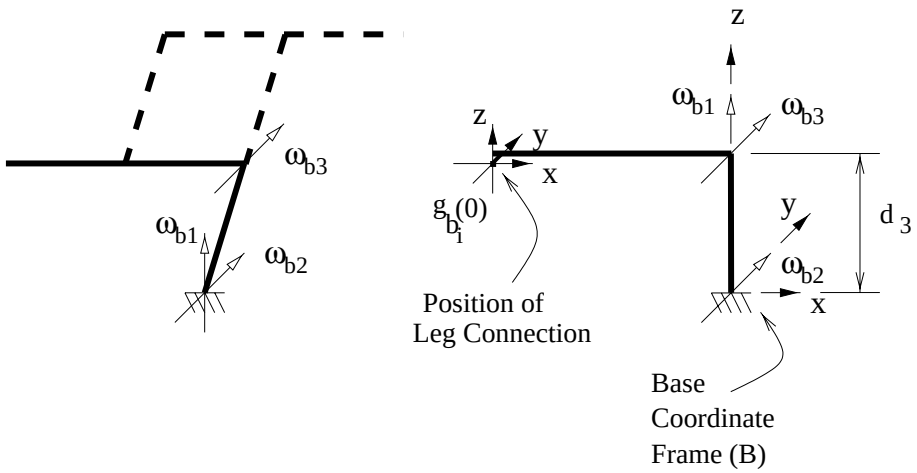

Figure 2.8: Naming convention and the zero configuration for the part of the gross stage connected to the legs.

Before proceeding with the forward kinematics of the part of the four-bar linkage connected to the legs, we note that $\theta_{b3} = \theta_{t3}$ from the four-bar linkage configuration, and $\theta_{b1} = \theta_{t1}$ and $\theta_{b2} = \theta_{t2}$ as these two joints are common between the two segments. For each of the legs, we define a separate zero configuration, $g_{b_i}(0)$. Then the desired configuration of the leg i is given by

$$g_{l_i d} = g_{L_i B} e^{\hat{\xi}_{b1}\theta_{b1}} e^{\hat{\xi}_{b2}\theta_{b2}} e^{\hat{\xi}_{b3}\theta_{b3}} g_{b_i}(0). \tag{2.51}$$

where $g_{L_i B}$ is the coordinate transformation from the base coordinate frame (B) to the coordinate frame of leg i (L_i).

Each of the legs have the kinematic configuration shown in Fig. 2.9. This kinematic configuration can be characterized by the following twists and the zero configuration expressed in the leg coordinate frame.

$$\xi_{l1} = \begin{bmatrix} 0 & 0 & 0 & 1 & 0 & 0 \end{bmatrix}^T \tag{2.52}$$

$$\xi_{l2} = \begin{bmatrix} 0 & 0 & 0 & 0 & 1 & 0 \end{bmatrix}^T \tag{2.53}$$

$$\xi_{l3} = \begin{bmatrix} 0 & 0 & 1 & 0 & 0 & 0 \end{bmatrix}^T \tag{2.54}$$

$$\xi_{l4} = \begin{bmatrix} 0 & 0 & h & 0 & 0 & 1 \end{bmatrix}^T \tag{2.55}$$

$$\xi_{l5} = \begin{bmatrix} 0 & 0 & 0 & 1 & 0 & 0 \end{bmatrix}^T \tag{2.56}$$

$$\xi_{l6} = \begin{bmatrix} 0 & 0 & 0 & 0 & 1 & 0 \end{bmatrix}^T \tag{2.57}$$

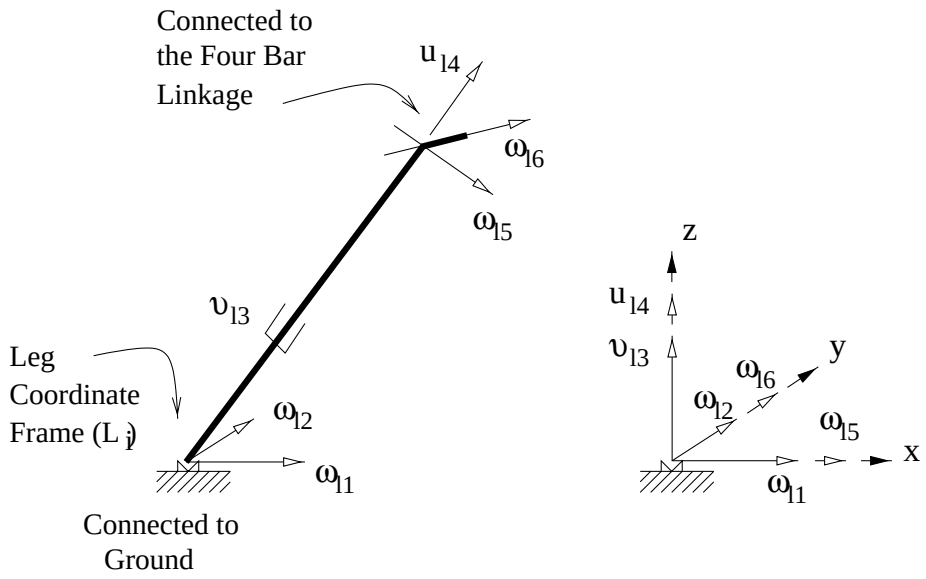

Figure 2.9: Naming convention and the zero configuration of the legs.

$$g_l(0) \quad = \quad I_{4\times 4} \tag{2.58}$$

The axes ω_1 and ω_2 are the rotations of the u-joint connecting the leg to the base, v_3 is the actuated linear axis, u_4 is the screw joint at the end of the shaft of the linear joint, and the axes ω_5 and ω_6 are the rotations of the u-joint connecting to the end of the four-bar linkage. h is the pitch of the screw joint u_4. The zero configuration of the leg is defined as the configuration where it is at zero extension.

Given the desired configuration of a leg, g_{ld}, we have

$$e^{\hat{\xi}_{l1}\theta_{l1}} e^{\hat{\xi}_{l2}\theta_{l2}} e^{\hat{\xi}_{l3}\theta_{l3}} e^{\hat{\xi}_{l4}\theta_{l4}} e^{\hat{\xi}_{l5}\theta_{l5}} e^{\hat{\xi}_{l6}\theta_{l6}} I_{4\times 4} \quad = \quad g_{ld} \tag{2.59}$$

$$e^{\hat{\xi}_{l1}\theta_{l1}} e^{\hat{\xi}_{l2}\theta_{l2}} \overbrace{\begin{bmatrix} I_{3\times 3} & \underline{z}\theta_{l3} \\ 0 & 1 \end{bmatrix}}^{e^{\hat{\xi}_{l3}\theta_{l3}}} \overbrace{\begin{bmatrix} I_{3\times 3} & \underline{z}h\theta_{l4} \\ 0 & 1 \end{bmatrix} \begin{bmatrix} e^{\underline{z}\theta_{l4}} & 0 \\ 0 & 1 \end{bmatrix}}^{e^{\hat{\xi}_{l4}\theta_{l4}}} e^{\hat{\xi}_{l5}\theta_{l5}} e^{\hat{\xi}_{l6}\theta_{l6}} I_{4\times 4} \quad = \quad g_{ld} \tag{2.60}$$

$$e^{\hat{\xi}_{l1}\theta_{l1}} e^{\hat{\xi}_{l2}\theta_{l2}} \begin{bmatrix} I_{3\times 3} & \underline{z}(\theta_{l3} + h\theta_{l4}) \\ 0 & 1 \end{bmatrix} \begin{bmatrix} e^{\underline{z}\theta_{l4}} & 0 \\ 0 & 1 \end{bmatrix} e^{\hat{\xi}_{l5}\theta_{l5}} e^{\hat{\xi}_{l6}\theta_{l6}} I_{4\times 4} \quad = \quad g_{ld} \tag{2.61}$$

where $\underline{z} = \begin{bmatrix} 0 & 0 & 1 \end{bmatrix}^T$. If we define

$$\theta'_{l3} \quad = \quad \theta_{l3} + h\theta_{l4} \tag{2.62}$$

$$\xi'_{l4} = \begin{bmatrix} 0 & 0 & 0 & 0 & 0 & 1 \end{bmatrix}^T \tag{2.63}$$

we get

$$e^{\hat{\xi}_{l1}\theta_{l1}} e^{\hat{\xi}_{l2}\theta_{l2}} e^{\hat{\xi}_{l3}\theta'_{l3}} e^{\hat{\xi}'_{l4}\theta_{l4}} e^{\hat{\xi}_{l5}\theta_{l5}} e^{\hat{\xi}_{l6}\theta_{l6}} I_{4\times 4} = g_{ld} \tag{2.64}$$

which is the same kinematic configuration as the Stanford manipulator. We start by

$$p_{l1} = \begin{bmatrix} 0 & 0 & 0 & 1 \end{bmatrix}^T \tag{2.65}$$

$$e^{\hat{\xi}_{l1}\theta_{l1}} e^{\hat{\xi}_{l2}\theta_{l2}} e^{\hat{\xi}_{l3}\theta'_{l3}} e^{\hat{\xi}'_{l4}\theta_{l4}} e^{\hat{\xi}_{l5}\theta_{l5}} e^{\hat{\xi}_{l6}\theta_{l6}} = g_{ld} \tag{2.66}$$

$$e^{\hat{\xi}_{l1}\theta_{l1}} e^{\hat{\xi}_{l2}\theta_{l2}} e^{\hat{\xi}_{l3}\theta'_{l3}} e^{\hat{\xi}'_{l4}\theta_{l4}} e^{\hat{\xi}_{l5}\theta_{l5}} e^{\hat{\xi}_{l6}\theta_{l6}} p_{l1} = g_{ld} p_{l1} \tag{2.67}$$

$$e^{\hat{\xi}_{l1}\theta_{l1}} e^{\hat{\xi}_{l2}\theta_{l2}} e^{\hat{\xi}_{l3}\theta'_{l3}} p_{l1} = g_{ld} p_{l1} \tag{2.68}$$

$$e^{\hat{\xi}_{l1}\theta_{l1}} e^{\hat{\xi}_{l2}\theta_{l2}} e^{\hat{\xi}_{l3}\theta'_{l3}} p_{l1} - p_{l1} = g_{ld} p_{l1} - p_{l1} \tag{2.69}$$

$$e^{\hat{\xi}_{l1}\theta_{l1}} e^{\hat{\xi}_{l2}\theta_{l2}} (e^{\hat{\xi}_{l3}\theta'_{l3}} p_{l1} - p_{l1}) = g_{ld} p_{l1} - p_{l1} \tag{2.70}$$

$$\left| e^{\hat{\xi}_{l1}\theta_{l1}} e^{\hat{\xi}_{l2}\theta_{l2}} (e^{\hat{\xi}_{l3}\theta'_{l3}} p_{l1} - p_{l1}) \right| = |g_{ld} p_{l1} - p_{l1}| \tag{2.71}$$

$$\left| e^{\hat{\xi}_{l3}\theta'_{l3}} p_{l1} - p_{l1} \right| = |g_{ld} p_{l1} - p_{l1}| \tag{2.72}$$

Then, subproblem 5 gives θ'_{l3}. Since the pitch of the screw joint, h, is small and can be neglected, the leg extension is given as

$$\theta_{l3} \approx \theta'_{l3} \tag{2.73}$$

If an exact solution is desired, it is possible to proceed by defining

$$p_{l2} = e^{\hat{\xi}_{l3}\theta'_{l3}} p_{l1} \tag{2.74}$$

and continuing with (2.68)

$$e^{\hat{\xi}_{l1}\theta_{l1}} e^{\hat{\xi}_{l2}\theta_{l2}} e^{\hat{\xi}_{l3}\theta'_{l3}} p_{l1} = g_{ld} p_{l1} \tag{2.75}$$

$$e^{\hat{\xi}_{l1}\theta_{l1}} e^{\hat{\xi}_{l2}\theta_{l2}} p_{l2} = g_{ld} p_{l1} \tag{2.76}$$

which can be solved by subproblem 2 to yield two solutions for θ_{l1} and θ_{l2}, with only one mechanically possible solution. Then,

$$e^{\hat{\xi}_{l1}\theta_{l1}} e^{\hat{\xi}_{l2}\theta_{l2}} e^{\hat{\xi}_{l3}\theta'_{l3}} e^{\hat{\xi}'_{l4}\theta_{l4}} e^{\hat{\xi}_{l5}\theta_{l5}} e^{\hat{\xi}_{l6}\theta_{l6}} = g_{ld} \tag{2.77}$$

$$e^{\hat{\xi}'_{l4}\theta_{l4}} e^{\hat{\xi}_{l5}\theta_{l5}} e^{\hat{\xi}_{l6}\theta_{l6}} = e^{-\hat{\xi}_{l3}\theta'_{l3}} e^{-\hat{\xi}_{l2}\theta_{l2}} e^{-\hat{\xi}_{l1}\theta_{l1}} g_{ld} \tag{2.78}$$

$$p_{l3} = \begin{bmatrix} 0 & 1 & 0 & 1 \end{bmatrix}^T \tag{2.79}$$

$$e^{\hat{\xi}'_{l4}\theta_{l4}} e^{\hat{\xi}_{l5}\theta_{l5}} e^{\hat{\xi}_{l6}\theta_{l6}} p_{l3} = e^{-\hat{\xi}_{l3}\theta'_{l3}} e^{-\hat{\xi}_{l2}\theta_{l2}} e^{-\hat{\xi}_{l1}\theta_{l1}} g_{ld} p_{l3} \tag{2.80}$$

$$e^{\hat{\xi}'_{l4}\theta_{l4}} e^{\hat{\xi}_{l5}\theta_{l5}} p_{l3} = e^{-\hat{\xi}_{l3}\theta'_{l3}} e^{-\hat{\xi}_{l2}\theta_{l2}} e^{-\hat{\xi}_{l1}\theta_{l1}} g_{ld} p_{l3} \tag{2.81}$$

which can be solved using subproblem 2 to calculate θ_{l4} and θ_{l5}. The calculation gives two solutions, one of which is mechanically possible. Then it is possible to calculate the exact value of θ_{l3}

$$\theta_{l3} = \theta'_{l3} - h\theta_{l4} \tag{2.82}$$

2.4 Forward Kinematics

The forward kinematics of the robot determines the configuration of the end-effector, g_{md}, given the angles of the actuated joints of the robot, lengths of the legs (l_1, l_2, l_3), amount of gross rotation (θ_{t6}), yaw flexion (θ_{m5}), and roll rotation (θ_{m6}).

The end-effector configuration can be calculated with the forward kinematics of the open chain $t1$–$t2$–$t3$–$t4$–$t5$–$t6$–$m5$–$m6$. However, for this, it is necessary to know the joint angles $(\theta_{t1}, \theta_{t2}, \theta_{t3}, \theta_{t4}, \theta_{t5})$. $(\theta_{t1} = \theta_{b1}, \theta_{t2} = \theta_{b2}, \theta_{t3} = \theta_{b3})$ are determined by the extension of the legs at the gross positioning stage, and $(\theta_{t4}, \theta_{t5})$ are determined by the constraint of the fulcrum.

The gross positioning stage of the slave manipulator has a parallel structure, which complicates the solution of the forward kinematics. Usually it is not possible to find closed form solutions for the forward kinematics of parallel manipulators.[2]

Here, we will use the simplified kinematics for the legs, ignoring the pitch of the screw joints (see (2.73)). Then, the linear joints at the legs give the following three nonlinear algebraic equations

$$\left\| g_{L_i B} e^{\hat{\xi}_{b1}\theta_{b1}} e^{\hat{\xi}_{b2}\theta_{b2}} e^{\hat{\xi}_{b3}} g_{b_i}(0)\underline{0} - \underline{0} \right\| = l_i \ , \ \text{for } i = 1, 2, 3 \tag{2.83}$$

in the three unknowns θ_{b1}, θ_{b2}, and θ_{b3}. $\underline{0} = \begin{bmatrix} 0 & 0 & 0 & 1 \end{bmatrix}^T$ is the origin. These equations do not have a closed form solution, but can be solved numerically. There is a unique solution $(\theta_{b1}, \theta_{b2}, \theta_{b3}) \in [-\pi/2, \pi/2]^3$ for a given (l_1, l_2, l_3).

Once $(\theta_{b1}, \theta_{b2}, \theta_{b3})$ are known, we can calculate $(\theta_{t4}, \theta_{t5})$ by using the constraint that the millirobot has to go through the fulcrum, which can be stated as the following two

[2]The most classical and well-studied example of this type of manipulators is the Stewart platform, which has no closed form solution available in literature [65].

vectors being parallel

$$g_t(\theta_t)\begin{bmatrix} 0 \\ 0 \\ -1 \\ 0 \end{bmatrix} \parallel g_{BF}\underline{0} - g_t(\theta_t)\underline{0} \tag{2.84}$$

where the vector on the left hand side is the vector along the shaft of the millirobot, and the vector on the right hand side is the vector between the fulcrum and the tip of the part holding the millirobot (See Fig. 2.10). Here,

$$g_t(\theta_t) = e^{\hat{\xi}_{t1}\theta_{t1}}e^{\hat{\xi}_{t2}\theta_{t2}}e^{\hat{\xi}_{t3}\theta_{t3}}e^{\hat{\xi}_{t4}\theta_{t4}}e^{\hat{\xi}_{t5}\theta_{t5}}e^{\hat{\xi}_{t6}\theta_{t6}}g_t(0) \tag{2.85}$$

If we define

$$p_{t0} = g_t(0)\underline{0} \tag{2.86}$$

then

$$e^{\hat{\xi}_{t4}\theta_{t4}}e^{\hat{\xi}_{t5}\theta_{t5}}e^{\hat{\xi}_{t6}\theta_{t6}}g_t(0)\underline{0} = e^{\hat{\xi}_{t4}\theta_{t4}}e^{\hat{\xi}_{t5}\theta_{t5}}e^{\hat{\xi}_{t6}\theta_{t6}}p_{t0} = p_{t0} \tag{2.87}$$

since p_{t0} is on ω_{t4}, ω_{t5}, and ω_{t6} axes. Also

$$e^{\hat{\xi}_{t6}\theta_{t6}}g_t(0)\begin{bmatrix} 0 \\ 0 \\ -1 \\ 0 \end{bmatrix} = e^{\hat{\xi}_{t6}\theta_{t6}}\begin{bmatrix} 0 \\ 0 \\ -1 \\ 0 \end{bmatrix} = \begin{bmatrix} 0 \\ 0 \\ -1 \\ 0 \end{bmatrix} \tag{2.88}$$

as $\omega_{t6} = \begin{bmatrix} 0 & 0 & 1 \end{bmatrix}$. Then (2.84) becomes

$$e^{\hat{\xi}_{t1}\theta_{t1}}e^{\hat{\xi}_{t2}\theta_{t2}}e^{\hat{\xi}_{t3}\theta_{t3}}e^{\hat{\xi}_{t4}\theta_{t4}}e^{\hat{\xi}_{t5}\theta_{t5}}\begin{bmatrix} 0 \\ 0 \\ -1 \\ 0 \end{bmatrix} \quad \parallel \quad g_{BF}\underline{0} - e^{\hat{\xi}_{t1}\theta_{t1}}e^{\hat{\xi}_{t2}\theta_{t2}}e^{\hat{\xi}_{t3}\theta_{t3}}p_{t0}. \tag{2.89}$$

With some manipulation,

$$e^{\hat{\xi}_{t4}\theta_{t4}}e^{\hat{\xi}_{t5}\theta_{t5}}\begin{bmatrix} 0 \\ 0 \\ -1 \\ 0 \end{bmatrix} \quad \parallel \quad e^{-\hat{\xi}_{t3}\theta_{t3}}e^{-\hat{\xi}_{t2}\theta_{t2}}e^{-\hat{\xi}_{t1}\theta_{t1}}\left(g_{BF}\underline{0} - e^{\hat{\xi}_{t1}\theta_{t1}}e^{\hat{\xi}_{t2}\theta_{t2}}e^{\hat{\xi}_{t3}\theta_{t3}}p_{t0}\right) \tag{2.90}$$

$$e^{\hat{\xi}_{t4}\theta_{t4}}e^{\hat{\xi}_{t5}\theta_{t5}}\begin{bmatrix}0\\0\\-1\\0\end{bmatrix} \quad \| \quad \left(e^{-\hat{\xi}_{t3}\theta_{t3}}e^{-\hat{\xi}_{t2}\theta_{t2}}e^{-\hat{\xi}_{t1}\theta_{t1}}g_{BF}\underline{0}-p_{t0}\right) \tag{2.91}$$

$$\begin{bmatrix}-\sin(\theta_{t5})\\ \cos(\theta_{t5})\sin(\theta_{t4})\\ -\cos(\theta_{t4})\sin(\theta_{t5})\\ 0\end{bmatrix} \quad \| \quad \left(e^{-\hat{\xi}_{t3}\theta_{t3}}e^{-\hat{\xi}_{t2}\theta_{t2}}e^{-\hat{\xi}_{t1}\theta_{t1}}g_{BF}\underline{0}-p_{t0}\right)=\gamma \tag{2.92}$$

where $\gamma = \begin{bmatrix}\gamma_1\\ \gamma_2\\ \gamma_3\\ 0\end{bmatrix}^T$. For physically realisable configurations $\gamma_1 \neq 1$, which yields

$$\theta_{t4} = \text{atan2}(\gamma_2, -\gamma_3) \tag{2.93}$$

$$\theta_{t5} = \text{atan2}(-\gamma_1, \sqrt{\gamma_2^2+\gamma_3^2}). \tag{2.94}$$

Then, the configuration of the end-effector can be calculated as

$$g_{md} = g_{BF}^{-1}e^{\hat{\xi}_{t1}\theta_{t1}}e^{\hat{\xi}_{t2}\theta_{t2}}e^{\hat{\xi}_{t3}\theta_{t3}}e^{\hat{\xi}_{t4}\theta_{t4}}e^{\hat{\xi}_{t5}\theta_{t5}}e^{\hat{\xi}_{t6}\theta_{t6}}e^{\hat{\xi}_{m5}\theta_{m5}}e^{\hat{\xi}_{m6}\theta_{m6}}g_{bm}(0) \tag{2.95}$$

where

$$g_{bm}(0) = \begin{bmatrix} & & d_2\\ I_{3\times3} & & 0\\ & & d_1-d_4\\ 0 & & 1\end{bmatrix}. \tag{2.96}$$

The workspace reachable by the gross stage of the slave manipulator is shown in Fig. 2.11. The boundary of the reachable workspace is determined by six surfaces corresponding to the minimum and maximum lengths of each of the three linear joints. The gross stage does not have a singularity in the workspace, but, the precision of the manipulator is reduced at the outer boundary of the workspace due to the larger moment arm.

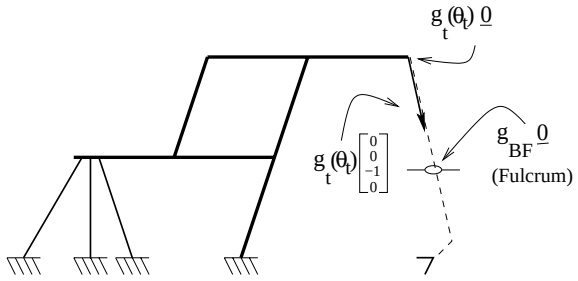

Figure 2.10: Constraints used in forward kinematics.

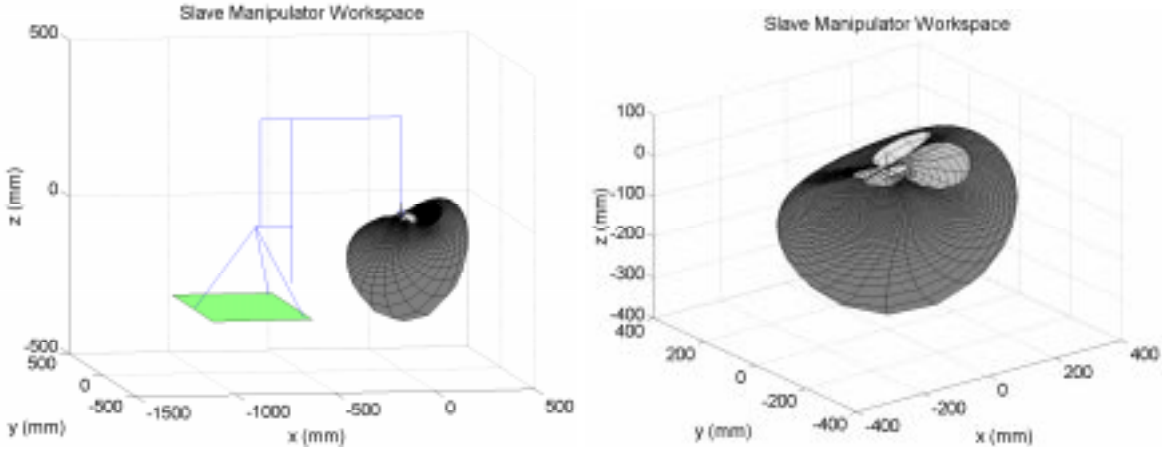

Figure 2.11: Workspace of the slave manipulator.

2.5 Control

The design of the teleoperation controller for the RTW is a critical component of the overall system since it provides the means of interaction of the operator with the remote site, i.e. interaction of the surgeon with the tissue. The overall structure of the proposed controller for the telesurgical workstation is shown in Fig. 2.12. In the current implementation joint level angle control is used. Individual joints of the slave manipulator are servoed with PID controllers to the joint trajectories determined from the solution of the slave inverse kinematics and the master forward kinematics along the trajectory of the master manipulator. There are not any force sensors installed on the manipulators. There is no force feedback available to the master from the slave side. Tactile loop is not present either. The only form of safety monitoring implemented is the heartbeat check performed by the robot. The robot listens to a heartbeat generated by the control software, and shuts

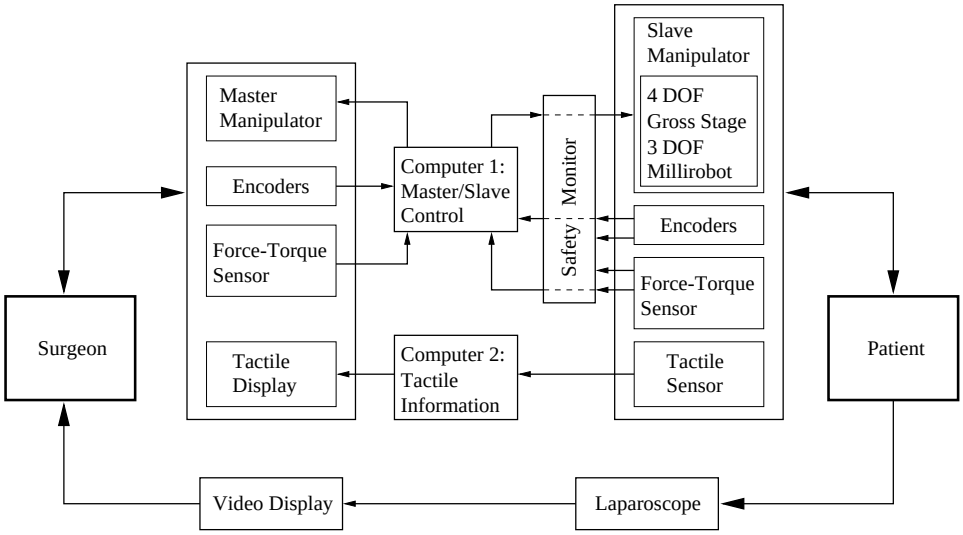

Figure 2.12: Block diagram of the proposed controller.

down all the motors, if the heartbeat is lost, which means a malfunction in the control software.

The issues related with design of high fidelity bilateral teleoperation controllers for the telesurgical system are addressed in detail in chapter 4.

Chapter 3

Experimental Evaluation

The first goal of the experimental evaluation of the robotic telesurgical workstation (RTW) is **verification of concept**. Being more precise, it is important to illustrate that it is possible to improve performance in MIS, and enable the performance of new procedures minimally invasively, which are not possible with existing MIS technology. This is necessary to justify the use of the system clinically, cost of the investment of buying and maintaining a RTW. Testing needs to focus on the two target tasks identified at the beginning, suturing and knot tying (see chapter 2).

There are several recent papers in the literature on evaluation of other robotic tools and assist systems for surgery. Garcia-Ruiz et.al. [36] performed pre-clinical evaluation of the SRI system (Menlo Park, CA) [45] in basic laparoscopic manipulation and suturing tasks compared to manual instruments, and Bowersox et.al. [11] evaluated the same system clinically on remotely performing operative urology, in several open surgical operations. Boehm et.al. [10] performed clinical evaluation of the Zeus system by Computer Motion Inc., (Goleta, CA) in minimally invasive coronary artery surgery and Sung et.al. [91] performed pre-clinical evaluation of this system in laparoscopic peloplasty in animal experiments. Cadiére et.al. reports results of the clinical evaluation of daVinci system by Intuitive Surgical, (Mountain View, CA) in laparoscopic Nissen fundoplication operation in [15]. And, Poulose et. al. [78] performed clinical evaluation of the LARS laparoscopic assistant [93] in laparoscopic Nissen fundoplication operation.

These papers, with the exception of [36] and [93], do not address the basic capabilities of the systems under study, and none of the above studies critically evaluate which elements of the systems were adequate or inadequate, nor they have enough information to

guide designers of future systems.

In this chapter, first, the general issues on the testing of the RTW are discussed, followed by the results of the experimental evaluation of the system. Then, a novel approach using open surgical suturing motion data to evaluate the kinematics of a robotic telesurgical manipulator without prototyping a physical system is proposed. The discussion is concluded by a review of the results and proposed improvements to the current prototype of the RTW. During the evaluation of the system, special emphasis is given to verification of concept and critical evaluation of the design choices for the system.

3.1 Phases of Testing

Experimental evaluation of the RTW can be divided into four phases of testing. Each of these phases are performed on a different platform and have different objectives.

- **Training box** Testing of the RTW in the training box aims the evaluation of the basic capabilities of the system. In this environment, it is possible to see if the RTW has the necessary dexterity and range of motion to perform the basic manipulation and suturing tasks.

- **Ex vivo tissue** Testing with *ex vivo* tissue is an extension of the training box testing. It is possible to test the ability of the system to manipulate soft tissue, and see if the manipulator has sufficient force and dexterity to manipulate tissue.

- **Animal testing** Animal testing evaluates the system with the constraints of working in the operating room and limited workspace of operating inside abdomen. It is possible to perform complete procedures, therefore to evaluate the complete functional capabilities of the RTW in a realistic setting.

- **Human testing** For human testing, it necessary to have a high level of safety and reliability, something which has not been addressed extensively in the current prototype of the system. This is part of the clinical evaluation of the RTW for premarket approval from Food and Drug Administration (FDA), and beyond the scope of this thesis [101].

3.2 Evaluation Criteria

The following aspects of the RTW need to be evaluated during the experimental testing of the system:

- **Precision** Since RTW will be under direct control of the surgeon with visual feedback, absolute accuracy is not critical. However, the system needs to have sufficient precision to be able to manipulate tissue and perform intricate tasks, suturing in particular.

- **Dexterity** One of the main objectives of the RTW is to improve dexterity of laparoscopic instruments to enable suturing and knot tying along arbitrary directions on a wide range of surface orientations in the significant portion of the workspace. Testing of the system need to clearly target evaluating the effectiveness of the RTW in this respect.

- **Functional capability** It is important to evaluate ability of the RTW to perform all the pieces of procedures, such as manipulation, dissection, traction, not just suturing and knot tying. This also has to be done with specific procedures in mind.

- **Ergonomics of the master workstation** There are several important issues with the master workstation. The master workstation needs to give an intuitive interface to the system. Typically, in MIS operations, the camera is almost continuously in motion, therefore, hand-eye coordination is an important factor. It is necessary to evaluate how well the surgeon can use the system under various amounts of misalignment between the haptic and visual coordinates, and how the system handles when the misalignment is large. It is also necessary to consider if the surgeon can effectively control the slave manipulator around the singularity of the wrist without getting confused. The general comfort and ease of use of the master needs to be considered as well.

- **Ergonomics of the slave system** One of the important set of requirements of the RTW come for the ergonomics of the slave system. The setting around the operating table needs to be comfortable enough to give access to the patient, enough room for the assistants and the camera holder, and avoid self collisions.

- **Design parameters of the robot** The following are the main design parameters of the RTW :

  - Tool diameter
  - Size of the workspace
  - Amount of roll rotation at the wrist
  - Amount of gross stage roll rotation
  - Amount of yaw axis flexion
  - Wrist-to-tip length
  - Shape of the tool
  - Location of the kinematic singularity

  It is important to evaluate the individual parameters as a feedback for the future design improvements.

- **Ease of learning to use by the surgeon** An important indicator of the effectiveness of the system is the answer to the question 'How long does it take for a novice / expert to learn to perform a benchmark task ?' It is important to make the distinction between the surgeons who are novice and expert in laparoscopy. It may be more difficult for the experts to learn to use RTW since they are already accustomed to perform tasks, e.g. suturing, in a specific way with the existing 4 DOF instruments, which is not necessarily the optimal way with a unconstrained 6 DOF manipulator.

- **Force feedback** The existing prototype of the RTW does not have any force feedback. It is important to evaluate if it is necessary to add force feedback for effective use of the system.

3.3 Testing the Second Generation UCB/UCSF Laparoscopic Telesurgical Workstation

In this section, we will present an experimental procedure for evaluating the suturing capabilities of the RTW in a training box, and discuss the results of the pilot experiments. The experimental procedure focuses on the ability of the RTW to suture at different direction and surface orientations, compared to the conventional laparoscopic tools (CLT) and open surgical tools (OST).

3.3.1 Method

Experimental Setup

For the experiments, three setups were used: RTW, CLT, and OST. For the RTW and CLT setups, two tools with 20 cm apart entry ports were used to suture at targets located approximately 20 cm away from the point midway between the entry ports. The tools had an 30^o approach angle with respect to the vertical. The target sites were observed with a 30^o angled laparoscope, which was kept stationary during the trials. The targets were positioned at the center of the field of view, and the field of view was wide enough to cover the necessary workspace without requiring to move the scope. For the CLT setup, the display was located directly in front of the surgeon, right behind the training box, about 1 m away. In the OST experiments, subjects used a 7 1/4 inch needle driver with their dominant hand, and a pair of DeBekey forceps with their non-dominant hand.

For all trails, 2-0 silk suture with V-20 taper needles (26 mm long, semicircular curvature, sharp tip) by US Surgical Corp. (manufacturers part number: GS-66-M) were used. The sutures were cut to 6 inches long. Latex gloves padded with 4x4 gauze pads, with approximately 1 cm uncompressed thickness, were used for the suturing surface. The entry and exit points for the needles were circles of approximately 3 mm in diameter with 1 cm separation, and were clearly marked on the suturing surfaces. Incision lines were also marked in between the entry and exit point locations.

Experimental Task

In the experiments, subjects were asked to pick up the needle from the fixed starting location, drive the needle through the marked target pair of entry and exit points on the suturing surface, and finish by tying a knot which is composed of a surgeon's knot followed by two half hitches.

Six targets were used in the experiments. Targets 1 and 2 were on a horizontal surface. Targets 3 and 4 were on a surface tilted 45^o and had no rotation. Targets 5 and 6 were on surfaces with 45^o tilt and had $\pm 45^o$ rotation around the vertical axis. For targets 1 and 3 the incision line was along the optical axis[1], and for targets 2 and 4 it was perpendicular to the optical axis. Targets 5 and 6 were rotated versions of target 3.

[1]Optical axis is the axis normal to the objective of the laparoscope, pointing into the field of view.

In each session, targets were presented in five sets. In the first four sets, targets 1 through 4 were presented in a Latin square fashion, and in the fifth set targets 5 and 6 were presented. The first set was intended as the training set, and no data was collected, and the fifth set was used to obtain qualitative information, since there were not enough trials to get any statistical information.

There were 3 subjects, who were surgical fellows in the Department of Surgery at UCSF. They were experienced laparoscopic surgeons trained in advanced laparoscopic procedures, who can be classified as experts in using conventional laparoscopic tools (with 1-3 years of laparoscopic suturing experience). Their experience with the RTW were limited. Two subjects had about 8 hours of experience, and one subject had less than 1 hour of experience using the robot. For each subject, the experiments were performed in three sessions, first with the RTW, followed by the CLT, and finally with the OST. The sessions took approximately 1 hour 30 minutes, 40 minutes, and 15 minutes respectively. For each setup, the same experimental procedure, i.e. order of targets, was repeated, and the same target orders were used for all the subjects.

3.3.2 Results

The results of the experiments cumulated among all three subjects are summarized in table 3.1. The OST results give a baseline performance for the experimental tasks, which are better than both RTW and CLT for all cases. Qualitatively, we can also observe that the subjects are slower with RTW compared to CLT, but tend to make fewer errors that require regrabbing with the RTW than they do with CLT. These results are parallel to those reported Garcia-Ruiz et.al. in [36].

For the knot tying durations, single-factor repeated-measures analysis of variance (ANOVA) performed separately for each of the instruments show no statistically significant variation due to targets ($p > 0.3$), which is expected. Single-factor repeated-measures ANOVA for the data cumulated for all targets reveal that the variation among instruments and subjects are statistically significant with $p < 0.001$ and $p < 0.002$ respectively (Fig. 3.1). A similar analysis performed for total task times also show statistically significant variation among instruments and among subjects, both with $p < 0.001$ (Fig. 3.2).

For the other time measures (time for positioning and needle driving) the variances are too large to give a statistically significant result. To decrease the variance, it is necessary

Target No	Time for positioning		Time for needle driving		Time for knot tying		# regrab. drg. positioning		# regrab. drg. needle dr.		# attmpts. drg. needle dr.	
	AVE	STD	AVE	STD	AVE	STD	AVE	STD	AVE	STD	AVE	STD
1–4	11.44	9.85	27.00	17.27	120.47	36.27	0.22	0.59	0.19	0.47	1.92	1.59
	10.56	12.07	12.42	9.29	44.36	12.37	0.78	1.31	0.25	0.55	1.61	0.90
	3.11	1.19	3.06	1.04	12.69	1.85	0.08	0.28	0.00	0.00	1.03	0.17
1	7.89	3.37	23.56	17.44	136.33	44.73	0.11	0.33	0.22	0.44	1.33	0.50
	6.22	5.14	13.89	9.88	40.78	6.92	0.00	0.00	0.44	0.73	2.11	0.93
	2.89	1.27	2.89	0.60	11.89	1.17	0.00	0.00	0.00	0.00	1.00	0.00
2	19.11	17.00	26.00	19.62	120.00	27.54	0.44	1.01	0.00	0.00	1.67	1.12
	6.78	4.02	14.67	13.44	46.00	17.76	0.89	1.62	0.33	0.71	1.67	0.87
	2.78	0.67	3.00	1.32	13.33	2.24	0.11	0.33	0.00	0.00	1.11	0.33
3	10.00	3.77	32.44	18.49	106.22	18.76	0.11	0.33	0.44	0.73	2.44	1.88
	18.44	20.09	10.44	5.77	42.89	11.12	1.56	1.51	0.11	0.33	1.33	1.00
	2.89	0.78	3.00	1.22	12.56	2.19	0.00	0.00	0.00	0.00	1.00	0.00
4	8.78	4.35	26.00	14.98	119.33	46.18	0.22	0.44	0.11	0.33	2.22	2.28
	10.78	9.18	10.67	7.05	47.78	12.23	0.67	1.12	0.11	0.33	1.33	0.71
	3.89	1.62	3.33	1.00	13.00	1.58	0.22	0.44	0.00	0.00	1.00	0.00
1,2	13.50	13.21	24.78	18.05	128.17	37.00	0.28	0.75	0.11	0.32	1.50	0.86
	6.50	4.49	14.28	11.45	43.39	13.35	0.44	1.20	0.39	0.70	1.89	0.90
	2.83	0.99	2.94	1.00	12.61	1.88	0.06	0.24	0.00	0.00	1.06	0.24
3,4	9.39	4.00	29.22	16.66	112.78	34.85	0.17	0.38	0.28	0.57	2.33	2.03
	14.61	15.66	10.56	6.25	45.33	11.62	1.11	1.37	0.11	0.32	1.33	0.84
	3.39	1.33	3.17	1.10	12.78	1.86	0.11	0.32	0.00	0.00	1.00	0.00
1,3	8.94	3.64	28.00	18.03	121.28	36.70	0.11	0.32	0.33	0.59	1.89	1.45
	12.33	15.56	12.17	8.05	41.83	9.05	0.78	1.31	0.28	0.57	1.72	1.02
	2.89	1.02	2.94	0.94	12.22	1.73	0.00	0.00	0.00	0.00	1.00	0.00
2,4	13.94	13.16	26.00	16.93	119.67	36.89	0.33	0.77	0.06	0.24	1.94	1.76
	8.78	7.17	12.67	10.62	46.89	14.82	0.78	1.35	0.22	0.55	1.50	0.79
	3.33	1.33	3.17	1.15	13.17	1.89	0.17	0.38	0.00	0.00	1.06	0.24

Table 3.1: Cumulated results for all subjects. For each cell in the table, the first row of numbers are for the RTW, the second row of numbers are for the CLT, and the third row of numbers are for the OST. All times are measured in seconds. Targets 1-4: 3 subjects $\times$ 3 trials for each target and experimental condition.

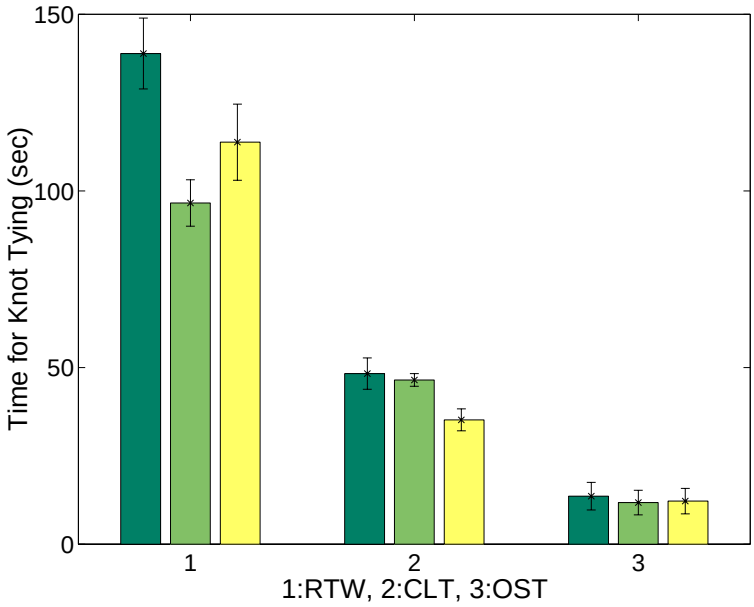

Figure 3.1: Knot tying times for each subject, cumulated over all the targets. 10% truncated mean ± estimated standard error is shown (10% truncated mean is the mean of the middle 80% (symmetric) of the data).

to have subjects with more training on the RTW. It is also desirable to have more trials in order to minimize the dominance of several isolated data points where the subjects had struggled considerably (for both RTW and CLT). The distributions for the error measures are not Gaussian, therefore, ANOVA is not applicable. Some more sophisticated statistical analysis is necessary to get quantitative results.

Experience and proficiency of the subjects with conventional laparoscopic tools gave a bias to the experimental results favoring against the RTW. For future experiments, it will be informative to have a subject pool which includes subjects who are familiar with laparoscopy but not very experienced with suturing and other advanced laparoscopic techniques, and analyze effects of this factor explicitly.

Two important problems with the existing design of the RTW identified during the experiment are the gripper control switches on the master and the master handles. The unsatisfactory design of the gripper switch resulted in a large number of misfirings of the gripper, which slowed down the subjects and forced errors. The subjects were also forced to consciously separate parts of the motion where they move the instruments and where they operate the gripper, rather than manipulating the suture with a smooth and intuitive

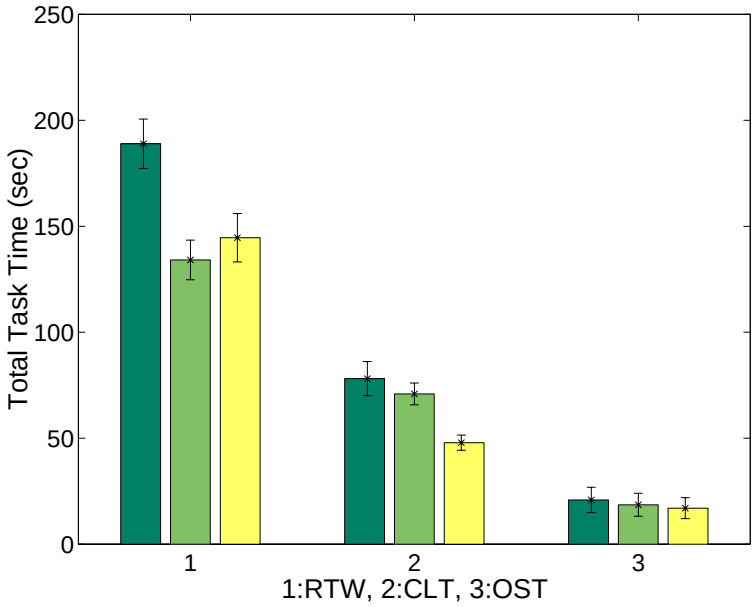

Figure 3.2: Total times for each subject, cumulated over all the targets. 10% truncated mean ± estimated standard error is shown.

motion. Also, the configuration of the master handle was an important source of complaint and is believed to be another factor which lowered the performance with the RTW. Training with the RTW is another important factor which will improve performance, since this will help the surgeons to use the full benefits of having a wrist.

At this point the qualitative observations and quantitative results discussed above will suffice, since the experiment revealed the overall trends and pointed out several important deficiencies of the RTW that caused the somewhat less than satisfactory performance of the system, including the problems with the master handle and the gripper control switch. The changes proposed to improve the performance of the RTW are discussed in detail below in section 3.5.

3.4 Analysis of the Workspace

It is desirable to develop a methodology to evaluate the kinematic ability of the system to perform the critical tasks of suturing and knot tying without actually building a physical prototype. This can be achieved by running typical tool motions during these tasks through the inverse kinematics calculations of the manipulators, to see if the system

can accommodate the desired motions. The system can perform a given motion if the whole trajectory lies continuously within the workspace of the manipulator.

As mentioned in chapter 2, one of the goals of the RTW is to enable the surgeons to use the open surgical techniques for suturing and knot tying in the MIS setting by having robotic tools with sufficient dexterity and a suitable user interface. Therefore, it is more appropriate to use open surgical suturing motions in the analysis. This way, it is possible to evaluate if the system can be used with the natural open surgical techniques, without the need of learning new ways to perform these tasks.

3.4.1 Method

We are using the open surgical suturing motion data obtained by Villanueva in [102]. In that study, experienced surgeons were asked to perform a simple suturing task while the motions of surgical instruments were tracked by 6 DOF trackers. The suturing task involved driving a curved needle into tissue followed by tying several knots in an open surgical setting. The surgeons were using a pair of needle drivers with their right hand, and forceps with their left hand, and the motion of the instruments were tracked by miniBIRD 6 DOF magnetic tracking devices (by Ascencion Technologies, Inc.). The surgeons repeated the task for several trials, resulting in multiple suturing motion trajectories.

Motion tracking of the instruments give the trajectories of the left and right hand instruments as

$$g_l(t) : [0, T] \rightarrow \mathrm{SE}(3) \tag{3.1}$$

$$g_r(t) : [0, T] \rightarrow \mathrm{SE}(3) \tag{3.2}$$

in the sensor coordinate frame[2]. These trajectories are converted to the suturing coordinate frame as

$$g_{ls}(t) = g_{SX} g_l(t) \tag{3.3}$$

$$g_{rs}(t) = g_{SX} g_r(t). \tag{3.4}$$

Here, g_{SX} is the coordinate transformation relating the sensor coordinate frame X to the suturing coordinate frame S. The advantage of using trajectories in the suturing coordinate

[2]For brevity, we have used continuous trajectories although the trajectories obtained experimentally are discrete samples of the actual continuous trajectory.

frame is that it is easier and more intuitive to specify the location and orientation of the entry port of the robot (configuration of the fulcrum coordinate frame of the robot) with respect to the suturing site.

If the left and right hand robots are located (and oriented) respectively at g_{F_lS} and g_{F_rS} with respect to the suturing coordinate frame, we will have the desired trajectories for the robots

$$g_{ld}(t) = g_{F_rS}g_{ls}(t) \tag{3.5}$$

$$g_{rd}(t) = g_{F_lS}g_{rs}(t), \tag{3.6}$$

which can then be mapped through the inverse kinematics to the joint trajectories. If the inverse kinematics have solution at every point during the motion and the resulting joint trajectory is continuous, then the manipulator can perform the desired motion.

3.4.2 Workspace Analysis Applied to the UCB/UCSF Robotic Telesurgical Workstation

If the joint limits of the rotational axes are not considered, the workspace of the RTW is connected. Then, if every point on the desired trajectory has a solution for inverse kinematics, the joint space trajectory is continuous. In the analysis below, we will not consider these joint limits for the inverse kinematics solution, but in turn find the necessary joint ranges to be able to accommodate the desired motions with a continuous motion.

Consider the manipulator configuration shown in Fig. 3.3, the manipulators at an approach angle of 30^o to the suturing surface normal. The inverse kinematics had valid solutions for all the trajectories tested.

The distribution of the joint angles for the whole motion of a typical trial is shown in Fig. 3.4. In the particular trial shown, all the axes of the system except for the yaw axis have sufficient joint range.

It is more informative to look at the distribution of the joint angles aggregated over several trials. Such a distribution is shown in Fig. 3.5, where five trials performed by one expert are aggregated. The resulting ranges of motion are summarized in table 3.2. In this case, the required ranges for the roll and gross rotation axes are quite large. This is because of the kinematic singularity of the wrist, which occurs when the yaw axis is at zero flexion, aligning the roll and gross rotation axes. Motions around the singularity result in

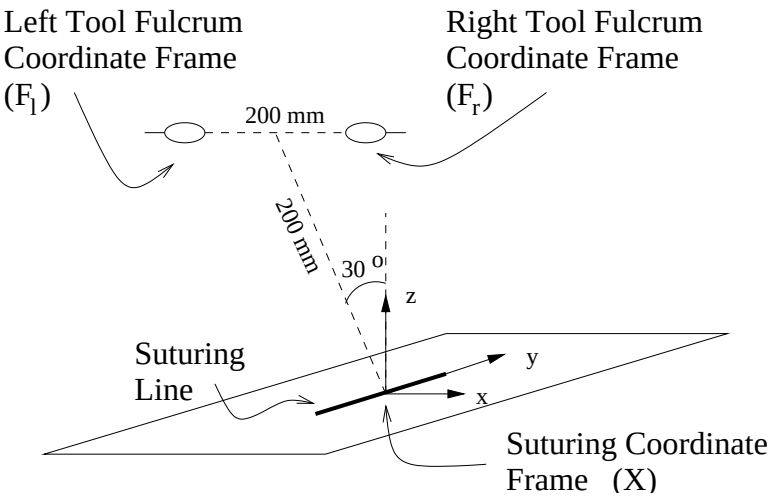

Figure 3.3: Configuration of the slave manipulators with respect to the suturing location used in the workspace analysis.

Joint	Left Min	Left Max	Left Range	Right Min	Right Max	Right Range	Total Range
θ_{m6}	-216^o	81^o	298^o	-233^o	318^o	551^o	551^o
θ_{m5}	5^o	132^o	127^o	31^o	179^o	148^o	175^o
θ_{t6}	-81^o	318^o	399^o	-666^o	-76^o	589^o	984^o
l_3	347mm	393mm	46mm	358mm	404mm	46mm	57mm
l_2	372mm	434mm	62mm	366mm	391mm	26mm	68mm
l_1	353mm	431mm	77mm	364mm	441mm	77mm	87mm

Table 3.2: Range of joint angles for the aggregate distribution.

the large joint motions observed. Actually, in only two of the five trials, the manipulator comes close to the singularity.

3.4.3 Concluding Remarks

It might be desirable to segment the critical and noncritical parts of the recorded open surgical motion, especially to remove the segments corresponding to the parts of the motion when the instrument is not being actively used. This way, it possible to avoid misleading results.

It is important to note that this method cannot evaluate if the system will have the complete dexterity necessary, since it looks at the problem from a purely kinematic point of view, and dexterity includes the dynamical properties of the manipulator as well as kinematics.

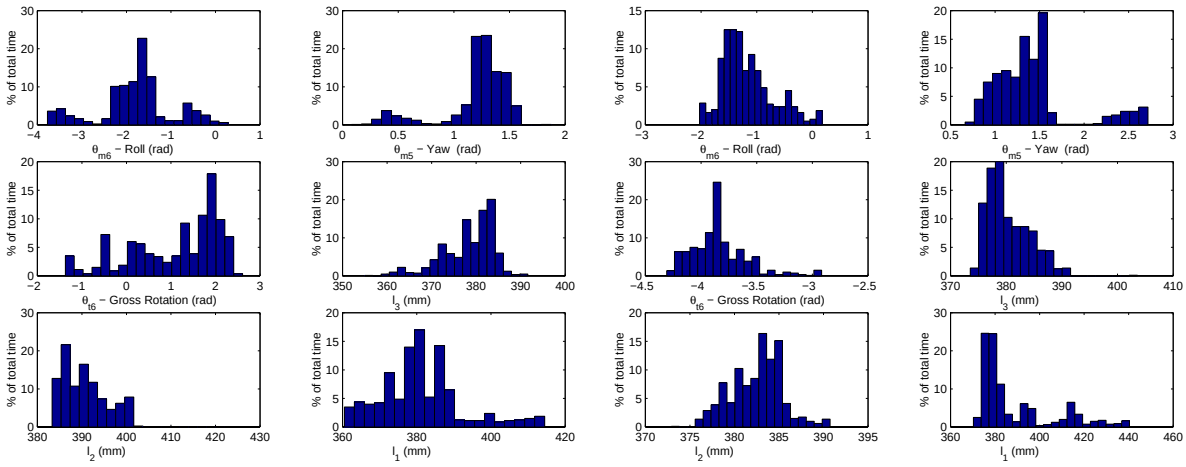

Figure 3.4: Distribution of the joint angles for a single trial of suturing task for the left (a) and right (b) hand instruments.

This method not only provides the means to evaluate a kinematic design, but also helps to determine the requirements on various design parameters, such as joint ranges. In the analysis, it is also possible to move the robot with respect to the suturing site, to see the suturing abilities of the system at different location and orientations in the workspace, and this can be used to find the entry port location and robot configuration for optimal performance in suturing.

3.5 Discussion of the Results

The experimental evaluation and the workspace analysis of the RTW help us to make the following observations about the current design and suggestions for the next generation system.

- Although we do not currently have any quantitative results comparing 4 versus 6 DOF manipulator configurations, the user comments suggest that having the 2 DOF wrist (which gives a 6 DOF slave manipulator) greatly improves the ability to suture and tie knots. This observation is further substantiated by the results of the experiments with suturing at different suturing surface orientations and incision directions.

- Even if it is possible to suture and tie knots with the current system, the available range of motion is quite restrictive. Especially, the limited range of the roll axis tend

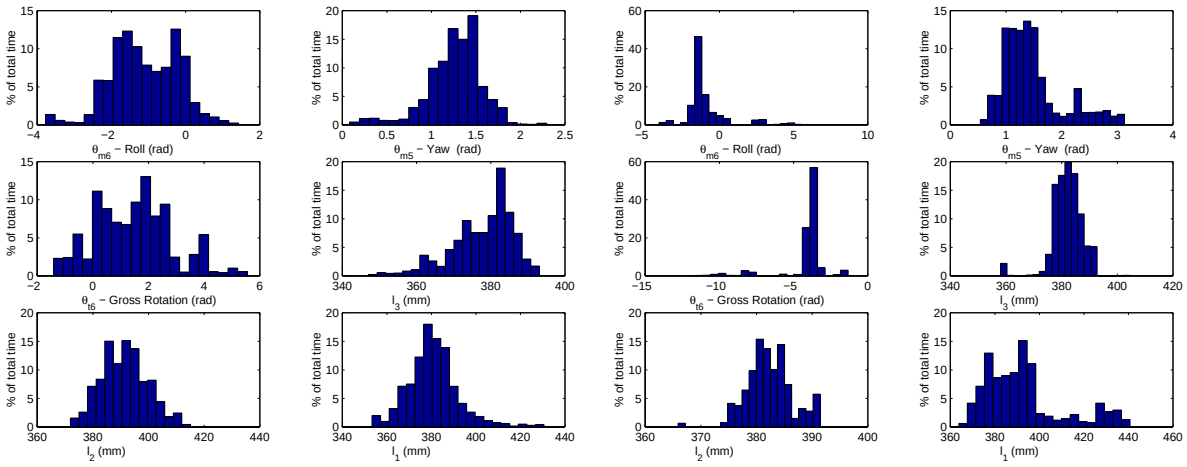

Figure 3.5: Distribution of the joint angles aggregated over five trials. Left (a) and right (b) hand instruments are shown.

to cause difficulties, requiring the user to pay extra attention to the positioning of this joint during initial grabbing of the needle, and forcing seldom regrabbing of the needle. Therefore, it is desirable to increase the range of motion for the roll axis, and to some extent the gross rotation. A range of 720^o, or higher, for the roll axis, and 1000^o or higher for the gross rotation should be considered as the design goals for the next generation wrist design.

- The yaw axis range needs to be extended to at least 135^o for more comfortable suturing at a wider range of suturing surface angles.

- The instrument diameter needs to be reduced below 10 mm for laparoscopic applications, and to 5 mm to accommodate other important minimally invasive applications, such as cardiac surgery.

- The handles on the master interface needs to be redesigned. The existing configuration, with the stylus handle and the gripper button located at the tip of the handle, was described as awkward, unnatural, and uncomfortable by the surgeons. Actually, this user interface configuration, difficulty in operating the grippers, and the frequent misfirings of the gripper, is the main reason behind the lower than expected performance of the RTW, relative to conventional laparoscopic tools.

- Ability to replace the end effectors is important for using the system during the

different phases of an operation to perform tasks other than suturing, such as holding tissue or dissection. These kind of tasks require different end effector designs.

- It is desirable to have an analog gripper for more effective control of the needle, by making it possible to lightly hold the needle and easily reorient it.

- Although the surgeons were able to successfully suture and tie knots without any force feedback, there were more cases when the needle snapped from the suture, or the suture itself was damaged, during the suturing experiments with the RTW compared to the CLT. This was mainly because of the lack of force feedback, since it is very difficult to judge the amount of force applied to the suture, just with visual feedback. Also, in the absence of force feedback, the forces felt by the operator on the handle are purely function of the master characteristics, completely independent of the what is happening on the slave side. This sometimes result in misleading haptic cues in terms of what is a natural motion of the slave, and what is not. Therefore, it is necessary to have some form of force feedback to the master from the slave side. For having an effective force feedback, it may preferable to be able to place a force/torque sensor on the slave manipulator, which should also be considered during the designing of the third generation slave manipulator.

Several items from the list of evaluation criteria given in the section 3.2 has not been discussed here. The precision of the manipulator has been empirically measured as 0.5 mm, and the results of the experimental evaluation suggest sufficient precision. Functional capabilities of the RTW should be evaluated by performing complete procedures in animal experiments. Animal experiments will also help to evaluate the ergonomics of the slave manipulator setup. Learning curve for the RTW needs to be studied as well. The experimental task described here can be used as the bechmark task, however it is necessary to modify the experimental procedure to evaluate learning, and to choose a subject pool which includes surgeons who are experienced with laparoscopy but not with laparoscopic suturing.

Chapter 4

Bilateral Control Design for Telemanipulation of Soft Objects

As it was discussed in section 2.5, the bilateral controller of the RTW is a critical part of the overall system being directly related to the performance and fidelity of interaction.

Previous research on teleoperation has focused on manipulation of hard objects. However, the design constraints are different in an application which involves manipulation of deformable objects. The stability-fidelity trade-off is the main determinant of the control design for teleoperation systems, as it is in many other control design problems. Both fidelity and stability are inherently dependent on the task for which the system is designed. This chapter addresses the issues in bilateral control design for telemanipulation of soft objects.

As noted by Lawrence in [62], teleoperation controller architectures given in the literature can be classified in terms of the stability-fidelity trade-off. Control algorithms for ideal kinesthetic coupling [109] are optimized for fidelity[1] and form one end of the spectrum, whereas passive communication based algorithms [75, 3, 4] are optimized for stability and form the other end. Conventional algorithms such as position error based force feedback and kinesthetic force feedback lie in the middle. There are also more recent controller designs using robust control theory. Kazerooni established an H_∞ based framework to design a teleoperation controller which transmits only force information and no position or velocity

[1] Transparency to be more accurate.

data [56]. Yan and Salcudean used H_∞ optimization to design controllers for motion scaling [108], and Hu et al. formulated the teleoperator control design as a convex H_∞ optimization problem [46]. Leung et al. used μ-synthesis to design controllers for teleoperation under time delay [63].

Operator performance is one of the important components of teleoperator design. Therefore experimental evaluation of control algorithms is crucial. Experimental studies at the NASA Jet Propulsion Laboratory [29, 57, 44] and by Lawn and Hannaford [61] compare various teleoperation algorithms within the context of operator performance. Human perceptual capabilities should also be considered. Jones and Hunter [53] performed experiments on determining human perceptual capabilities within the context of teleoperation. In a recent work, Daniel [27] takes into account considerations for improved stimulation of the tactile and kinesthetic receptors during teleoperator controller design by modifying the filter in the force feedback path. Colgate [22] introduced impedance shaping bilateral control as a means of "constructively altering the impedance of a task".

Jones and Hunter has performed psychophysical studies to determine the stiffness [50] and viscosity [52] detection capabilities and effects of manipulandum stiffness [49] and viscosity [51] on human operator dynamics. Srinivasan [88] studied the active and passive discrimination of softness for deformable and compliant but non-deformable objects. Dhruv studied the frequency dependence of the human force and stiffness perception [96, 32]. Clark and Horch [18] give a detailed overview of the human kinesthetic perception.

In the design of a teleoperation system controller, there are two considerations we believe to be important. First, it is important to have task based performance goals rather than trying to achieve a marginally stable, physically unachievable ideal teleoperator response. Second, design of the teleoperation system must be oriented towards improving performance with respect to human perceptual capabilities. It is necessary to experimentally quantify human perceptual capabilities and to develop control design methodologies which will provide the means to include this in the control design.

Use of task based performance goals for teleoperation control design was proposed by several researchers in different contexts. But, there are no studies in the literature where this is explicitly included in control design methodology.

In this chapter, a theoretical and experimental framework to design and evaluate teleoperation control algorithms for telemanipulation of soft objects is developed. The emphasis is on the requirements of telesurgical applications, and the problem is addressed

from three aspects : on the theoretical side, control design (1) and quantitative comparison of sensory schemes (2), and on the experimental side, experimental comparison of teleoperation controllers (3). First, a new measure for fidelity in teleoperation is introduced which quantifies the teleoperation system's ability to transmit changes in the compliance of the environment. This sensitivity function is highly appropriate for the application of telesurgery, where the ability to distinguish small changes in tissue compliance is essential for tasks such as tumor detection. The bilateral teleoperation controller design problem is then formulated as the optimization of this new metric with constraints on free space tracking requirements and robust stability of the system under environment and human operator uncertainties. This is followed by the section on quantitative comparison of controller architectures and sensory schemes. Two methods are introduced, the first one is the extension of the control design method discussed in the previous section, and the second one is based on Kalman filters. The methodologies for control design and comparison of sensory schemes are illustrated in a case study in the following section, applied to an experimental teleoperation testbed. The experimental comparison of teleoperation control algorithms is then discussed in section 4.6.

4.1 Formulation

A teleoperation system can be represented with the simple block diagram of Fig. 4.1. We will consider the model given in Fig. 4.2 as the underlying physical model throughout the analysis where it is necessary to use an explicit plant model.The following analysis is performed for linear models of the teleoperation system. It is imperative to note that this is only valid locally, but can be extended to the whole workspace by using gain scheduling or a similar technique.

The teleoperator can be modeled as a two-port network element relating force and position of the master manipulator, F_m and X_m, to the slave manipulator, F_s and X_s[2]. We follow Hannaford [42] in using the hybrid parameters to characterize system behavior (Fig.

[2]In the literature, generally a force/velocity representation is used instead of a force/position representation. Although force/velocity representation has an advantage since the power is immediately given by the terminal variables of the two port, it introduces a pole/zero pair at the origin, which causes complications in stability analysis conditions, which is purely an artifact of the representation. Here, the force/position representation is used to avoid these complications.

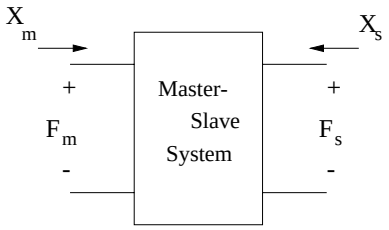

Figure 4.1: Two port input-output model of a teleoperation system.

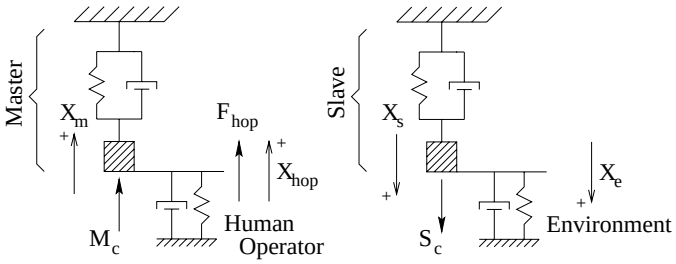

Figure 4.2: Physical model of the teleoperation system.

4.3)

$$\begin{bmatrix} F_m(s) \\ X_s(s) \end{bmatrix} = \begin{bmatrix} h_{11}(s) & h_{12}(s) \\ h_{21}(s) & h_{22}(s) \end{bmatrix} \begin{bmatrix} X_m(s) \\ F_s(s) \end{bmatrix} \tag{4.1}$$

Environment impedance transmitted through the teleoperator (Fig. 4.4) can be calculated as

$$Z_t = \frac{F_m}{X_m} = \frac{h_{11} + (h_{11}h_{22} - h_{12}h_{21})Z_e}{1 + h_{22}Z_e} \tag{4.2}$$

using the hybrid parameters.

4.2 Fidelity

It is important to explicitly distinguish the terms *fidelity* and *transparency* in teleoperation. Fidelity is a task dependent definition of performance, whereas transparency is one specific choice of fidelity measure which quantifies how close the transmitted impedance is to the environmental impedance.

Transparency is the main form of performance measure used in the teleoperation literature. With this, the goal of the control design is to match the position and forces at the master and slave manipulators exactly or through a virtual impedance [109]. One form of

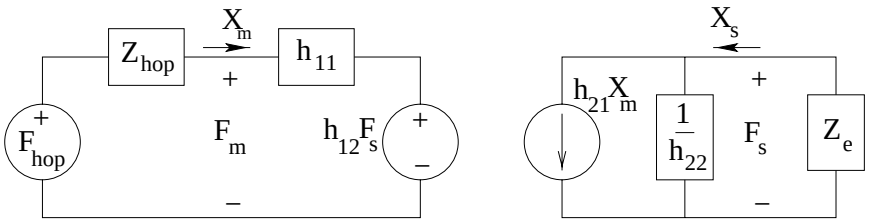

Figure 4.3: Hybrid parameters of a teleoperation system.

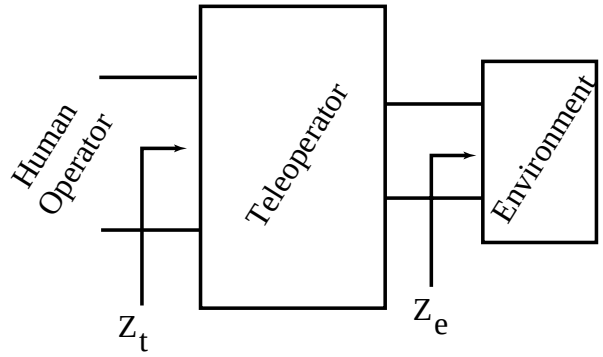

Figure 4.4: Z_t is impedance felt by the operator at the master, which is the environment impedance Z_e transmitted through the teleoperator.

transparency measure is proposed by Lawrence in [62] as the ratio between the transmitted and the environment impedances. Lawrence's design goal was to keep this ratio close to one over a maximal bandwidth.

In robotic telesurgery one would like to improve the ability to detect compliance changes in the environment in addition to the basic requirement of "good" tracking in free space and while in contact with tissue. This compliance detection is critical in a surgical application in two ways. First, the interaction of the needle with tissue during suturing, such as to feel when the needle punctures or leaves tissue, can be detected through the change in the compliance. Second, the structures hidden inside the tissue, such as blood vessels, major nerves, or tumors, can be located by noninvasively probing the tissue. In these cases, it is more desirable to have the ability to detect the changes in the environment impedance than simple position or force tracking between the master and slave manipulators. Therefore, it is necessary to introduce a fidelity measure which quantifies this ability.

The measure of fidelity proposed here is the sensitivity of the transmitted impedance

to changes in the environmental impedance. This can be defined as

$$\left\| W_s \left. \frac{dZ_t}{dZ_e} \right|_{Z_e=\hat{Z}_e} \right\|_2 \tag{4.3}$$

where W_s is a frequency dependent weighting function, and $\hat{Z}_e$ is the nominal environment impedance.

The weighting function W_s represents the frequency dependent sensitivity of the human operator to environment impedance changes. In this study, a low pass filter with cutoff frequency of 40 Hz is used as the weighting function. This frequency was determined from our pilot experiments for determining human compliance discrimination thresholds. A parallel research study is being conducted by our research group to determine this operator sensitivity function through psychophysics experiments [32]. These studies reveal that the sensitivity of the human operator to stiffness stimuli increases with increasing frequency. This implies that the high frequency response of the system is critical for good performance.

4.3 Task Based Optimization of the Teleoperation Controller

The controller to be used for the teleoperation system needs to satisfy some basic requirements such as stability under specified environment and operator variations. Once these are satisfied, the remaining freedom in the controller can be used to optimize a task dependent performance measure, in this case fidelity.

4.3.1 Stability

Any teleoperation system must maintain stability under operator and environment variations. Robust stability of the closed loop system under unstructured uncertainty can be used to check this by properly modeling the operator and environment variations as uncertainty in the system.

For stability analysis, we use a robust stability criterion for unstructured uncertainties as given in Zhou, Doyle, and Glover [110]. For SISO systems, the criterion is as follows.

Theorem 1 (Robust Stability Criterion) *Consider the closed loop system shown in Figure 4.5 with multiplicative unstructured uncertainty. The uncertainty is defined as*

$$P \in M(\hat{P}, W_u) = \{\hat{P}(1 + W_u\Delta) : \Delta \in \mathcal{R}, \sup|\Delta(j\omega)| < 1,$$

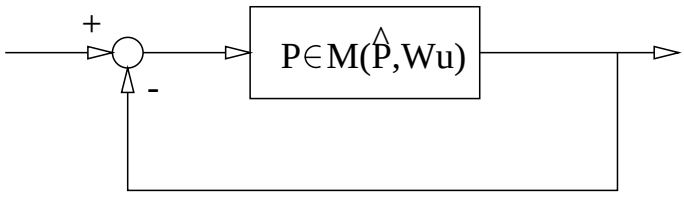

Figure 4.5: Closed loop system with multiplicative uncertainty.

$$\#\ of\ rhp\ poles(\hat{P})\ =\ \#\ of\ rhp\ poles\ (\hat{P}(1+W_u\Delta))\}, \tag{4.4}$$

where P is the loop gain, $\hat{P}$ is the nominal plant loop gain, W_u is the uncertainty weighting function, and $\mathcal{R}$ is the set of proper real rational functions. Then, the closed loop system shown is stable for all $P \in M(\hat{P}, W_u)$, if and only if it is stable for the nominal plant $\hat{P}$, and

$$\|W_u T\|_\infty \leq 1, \tag{4.5}$$

where $T = \frac{\hat{P}}{1+\hat{P}}$.

The uncertainty weighting function $|W_u(j\omega)|$ can be interpreted as the percentage uncertainty in $\hat{P}$ at the frequency w.

For the teleoperation system, the loop gain P is calculated in Hannaford [43] as

$$P = \frac{-h_{12}h_{21}Z_e}{(h_{11}+Z_{hop})(1+h_{22}Z_e)} \tag{4.6}$$

where Z_e and Z_{hop} are respectively the environment and human operator impedances, and h_{ij} are the hybrid parameters of the teleoperator.

In this study we will consider the uncertainties in the human operator and the environment impedances. First, consider the variation in the environment. Since Z_e appears as $\frac{Ze}{1+h_{22}Z_e}$ in the loop gain expression, we proceed to put an upper bound to the variation in this term for the possible set of environments, $Z_e \in \mathcal{Z}_e$.

Start with some manipulation

$$P = \frac{-h_{12}h_{21}Z_e}{(h_{11}+Z_{hop})(h_{22}Z_e+1)} \tag{4.7}$$

$$= \underbrace{\frac{-h_{12}h_{21}}{(h_{11}+Z_{hop})}\frac{\hat{Z}_e}{h_{22}\hat{Z}_e+1}}_{\hat{P}}\underbrace{\frac{h_{22}\hat{Z}_e+1}{\hat{Z}_e}\frac{Z_e}{h_{22}Z_e+1}}_{1+W_{ue}\Delta} \tag{4.8}$$

Since we want to have the nominal environment $\hat{Z}_e$ for $\Delta = 0$, we pick

$$W_{ue}\Delta = \frac{1 + h_{22}\hat{Z}_e}{\hat{Z}_e}\frac{Z_e}{1 + h_{22}Z_e} - 1 \tag{4.9}$$

$$= \frac{1}{h_{22}\hat{Z}_e}\frac{Z_e - \hat{Z}_e}{\frac{1}{h_{22}} + Z_e} \tag{4.10}$$

then we pick an upper bound to

$$\left|\frac{Z_e - \hat{Z}_e}{\frac{1}{h_{22}} + Z_e}(j\omega)\right| < |\Phi(j\omega)| \tag{4.11}$$

for the possible environment values, which gives

$$W_{ue} = \frac{1}{h_{22}\hat{Z}_e}\Phi. \tag{4.12}$$

Φ can be a function of the controller values and other known variables present in h_{22}.

Similarly, for the operator impedance variation, we proceed to put an upper bound to the term $\frac{1}{h_{11}+Z_{hop}}$ for the possible set of operator impedances, $Z_{hop} \in \mathcal{Z}_{hop}$. We pick

$$W_{uh}\Delta = \frac{h_{11} + \hat{Z}_{hop}}{h_{11} + Z_{hop}} - 1 \tag{4.13}$$

$$= \frac{\hat{Z}_{hop} - Z_{hop}}{h_{11} + Z_{hop}} \tag{4.14}$$

to have $\hat{Z}_{hop}$ for $\Delta = 0$. Then, we can pick an upper bound

$$\left|\frac{\hat{Z}_{hop} - Z_{hop}}{h_{11} + Z_{hop}}(j\omega)\right| < |W_{uh}(j\omega)| \tag{4.15}$$

which can be a function of the known variables present in h_{11}.

The two uncertainty terms can be combined to give a single multiplicative uncertainty weighting function as

$$W_u = W_{ue} + W_{uh} + W_{ue}W_{uh}. \tag{4.16}$$

4.3.2 Tracking Requirement

The tracking requirement is necessary to prevent the final controller parameter optimization from yielding trivial solutions. To illustrate this complication, consider the case of optimizing a controller for transparency at a given environment stiffness operating

point. The trivial solution to this optimization is to have a master controller which gives the master manipulator an apparent stiffness equal to the nominal environment stiffness, and have no feedback from slave to master or even not actuate the slave at all. The most natural constraint to prevent this kind of behavior is to require the teleoperation system to have sufficient tracking performance in free space. We will pose this tracking requirement as a condition on the disturbance sensitivity function of the forward position loop during motion in free space. In the hybrid parameter formulation of the teleoperator, this sensitivity function is given by

$$S = 1 - h_{21}. \tag{4.17}$$

Then the tracking requirement can be posed as

$$|S(j\omega)| < |b(j\omega)| \iff \|SW_p\|_\infty \leq 1,\ W_p = 1/b(j\omega) \tag{4.18}$$

which dictates a tracking error less than $|b(j\omega)|$ for a sinusoidal input with angular frequency w and magnitude 1. This effectively puts a condition on the slave position gain when the slave is controlled by the master position (position only loop in the forward direction).

4.3.3 Optimizing for Fidelity

The controller gains are chosen to optimize the fidelity among the set of controller values which satisfy stability and tracking requirements.

$$\arg \sup_{\substack{\|W_u T\|_\infty \leq 1 \\ \text{stable for } \hat{P} \\ \|W_p S\|_\infty \leq 1}} \inf_{\tilde{Z}_e \in \tilde{\mathcal{Z}}_e} \left\| W_s \left. \frac{dZ_t}{dZ_e} \right|_{\tilde{Z}_e} \right\|_2 \tag{4.19}$$

The fidelity term is slightly modified from (4.3) to be more general, optimizing the worst case fidelity for a given set of environment values, $\tilde{\mathcal{Z}}_e$. $\tilde{\mathcal{Z}}_e$ is the range of environments in which sensitivity of the transmitted impedance to environment impedance variations is desired. It is important to note that this is not a convex optimization since $\left\| W_s \frac{dZ_t}{dZ_e} \right\|_2$ is not convex in the controller parameters.

4.4 Comparing Controller Architectures and Sensors

For more effective control of the teleoperation system and hence for better performance, it is desirable to put additional sensors on the manipulators. However, any additional sensors cause design complications. This is especially true for sensors to be located on the slave manipulator. In addition to the problems related to the size, as these sensors need to be located on the part of the instrument which will be inside the body, it is a source of complications in the manipulator design, sterilization requirements, and adds to the cost of the final product. Therefore it is important to have theoretical analysis tools to compare different sensory schemes in terms of performance. This way, it is possible to make informed decisions in choosing sensors for the system. One of the main goals for this analysis is to determine if the use of a force sensor is necessary on the slave manipulator of the telesurgical workstation for sufficient fidelity.

4.4.1 Method 1 : Extending the Control Design Methodology

Within this context, we will compare three different control architectures commonly used in practice: position error (PERR), kinesthetic force feedback (KFF), and position error plus kinesthetic force feedback (P+FF) (Fig. 4.6). In the PERR architecture, the force sent to the master is proportional to the position error between the master and slave manipulators. The KFF architecture uses a force sensor on the slave end to measure and transmit forces back to the master. The P+FF architecture is a hybrid of KFF and PERR. In this architecture, the force fed back to the master is a linear combination of the position error and the interaction force between the slave and the environment. In all three controllers the master position is used to command the slave.

Essentially, the PERR and KFF architectures are the limit cases of the more general control architecture P+FF. Therefore it is possible to quantify the improvement due to using a force sensor for a given task by looking at how the fidelity of the P+FF architecture changes as the force gain is changed.

The *alpha*-curve is defined as the highest fidelity achievable with the P+FF controller subject to stability and tracking constraints as a function of the force gain α (see

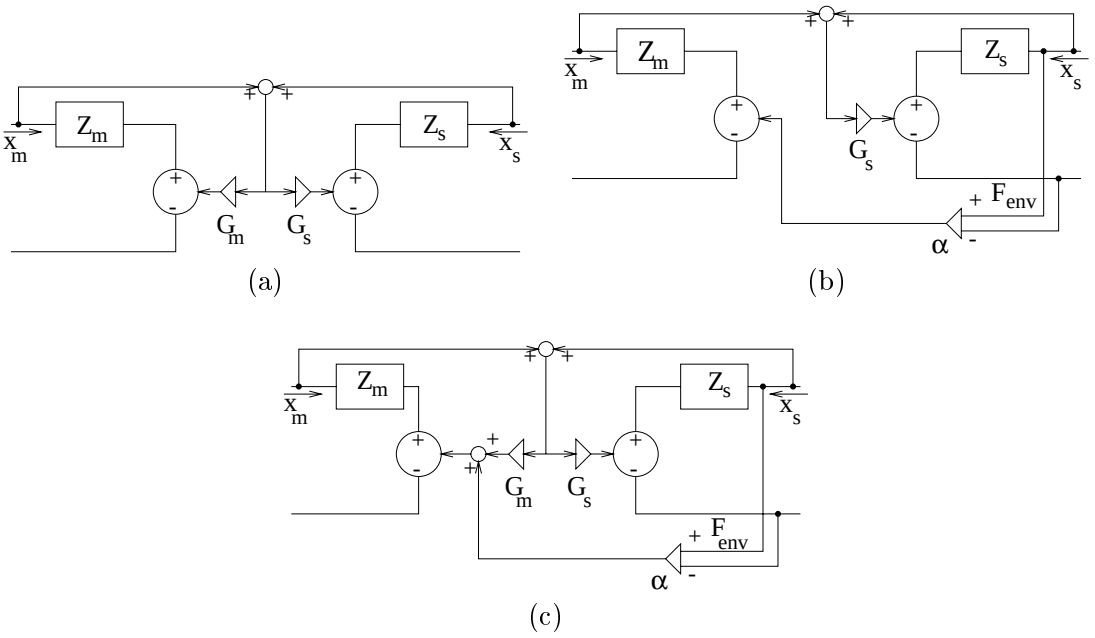

Figure 4.6: PERR, KFF and P+FF architectures

Fig. 4.6c).

$$f(\alpha) = \sup_{\substack{\|W_u T\|_\infty \le 1 \\ \text{stable for } \hat{P} \\ \|W_p S\|_\infty \le 1 \\ G_m, G_s}} \inf_{\tilde{Z}_e \in \tilde{\mathcal{Z}}_e} \left\| W_s \left. \frac{dZ_t}{dZ_e} \right|_{\tilde{Z}_e} \right\|_2 \tag{4.20}$$

The shape of this curve depends on the stability constraint as well as the fidelity measure being used. There are three different cases based on location of the maximum point of the curve (Fig. 4.7). If the PERR end is the maximum, use of a force sensor does not improve performance. If the KFF end is the maximum, then it is better to use purely the force sensor output as the source of force feedback. Finally, if the maximum is located at an intermediate point, it is possible to have better performance by using a combination of position error and the force measurements to generate force feedback. The relative value of the peak value of the curve to the PERR value can be used to judge if the amount of performance improvement justifies cost of using the force sensor.

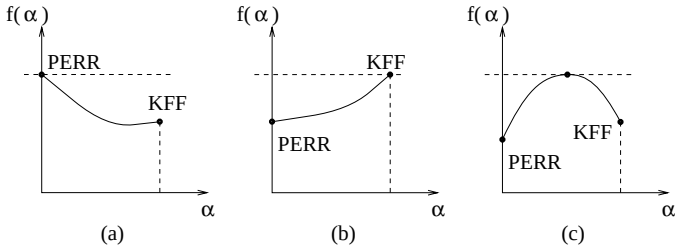

Figure 4.7: Possible cases for the shape of *alpha*-curve

4.4.2 Method 2 : Kalman Filter Analysis

Kalman filter [64, 2] gives the optimal linear state estimator for a linear system given the process and measurement noise characteristics. The error statistics of the state estimates is a limiting factor on the performance achievable with a state feedback controller, as the controller needs to be slower than the observer (state estimator) poles which are in turn dictated by the error in the estimates.

We propose to quantitatively compare the different sensory schemes for the tele-operation system by comparing the norm of the *a posteriori* error covariance matrices of the Kalman filters for each configuration.

Kalman Filter Overview

The discussion in this section follows the notation and formulation of Lewis [64]. Given the following continuous time stochastic linear system in state space representation which will be controlled with a discrete time controller:

$$\dot{z} = A^c z + B^c u + G^c w \tag{4.21}$$

$$y = Cz + v \tag{4.22}$$

where, $z(t) \in \mathbf{R}^n$ is the state vector, $u(t) \in \mathbf{R}^p$ is the control input, $w(t) \in \mathbf{R}^q$ is the process noise, $y(t) \in \mathbf{R}^m$ is the measurement vector, and $v(t) \in \mathbf{R}^m$ is the measurement noise. Suppose the $w(t)$ and $v(t)$ are zero mean white noise processes, with covariances Q^c and R^c respectively. The discrete time equivalent of this system is given by

$$z_{k+1} = Az_k + Bu_k + Gw_k \tag{4.23}$$

$$y_k = Cz_k + v_k \tag{4.24}$$

with

$$A = e^{A^c T} \tag{4.25}$$

$$B = \int_0^T e^{A^c \tau} B^c d\tau \tag{4.26}$$

$$G = I \tag{4.27}$$

$$w_k \sim (0, Q)\ ,\ \ Q = \int_0^T e^{A^c \tau} G^c Q (G^c)^T e^{(A^c)^T \tau} d\tau \approx G^c Q^c (G^c)^T \tag{4.28}$$

$$v_k \sim (0, R)\ ,\ \ R = R^c/T \tag{4.29}$$

and T is the sampling time. $z_k = z(kT)$ is the sampled state vector. Other sampled signals are defined similarly. Here it is assumed that $u(t)$ is constant between the samples, i.e. digital controller output has a zero order hold at the output. If (A, C) is detectable, $(A, G\sqrt{Q})$ is stabilizable, and $R > 0$, then the steady state Kalman filter for the discrete time system of (4.23),(4.24) is given as

$$\hat{z}_{k+1} = A\hat{z}_k + Bu_k + AK(y_k - C\hat{z}_k) \tag{4.30}$$

where $\hat{z}_k$ are the state estimates, and the Kalman filter gain K is given by

$$K = PC^T(CPC^T + R)^{-1} \tag{4.31}$$

which is a constant $n \times m$ matrix. P is the steady state *a priori* error covariance matrix, which is the solution of the following algebraic Ricatti equation:

$$P = A\left(P - PC^T(CPC^T + R)^{-1}CP\right)A^T + GQG^T. \tag{4.32}$$

Then, the steady state *a posteriori* error covariance matrix for the state estimates is

$$P^+ = P - PC^T(CPC^T + R)^{-1}CP. \tag{4.33}$$

Modeling the Teleoperation System and Sensors

A state space representation of the teleoperator model of Fig. 4.2 is as follows

$$\frac{d}{dt}\begin{bmatrix} x_s \\ \dot{x}_s \\ x_m \\ \dot{x}_m \end{bmatrix} = \begin{bmatrix} 0 & 1 & & \\ -\frac{K_s}{M_s} & -\frac{B_s}{M_s} & & 0 \\ & & 0 & 1 \\ 0 & & -\frac{K_m}{M_m} & -\frac{B_m}{M_m} \end{bmatrix}\begin{bmatrix} x_s \\ \dot{x}_s \\ x_m \\ \dot{x}_m \end{bmatrix} +$$

$$\begin{bmatrix} 0 & 0 & & \\ \frac{1}{M_s} & \frac{1}{M_s} & 0 & \\ & & 0 & 0 \\ 0 & & \frac{1}{M_m} & \frac{1}{M_m} \end{bmatrix} \begin{bmatrix} S_c \\ F_{env} \\ M_c \\ F_{hop} \end{bmatrix} \tag{4.34}$$

Here, we consider the environment and human operator forces as process noise. We also assume that they are uncorrelated first order Markov processes, which are modeled as low pass filtered white noise sources. Incorporating these into the model, we get the following state space representation

$$\underbrace{\frac{d}{dt}\begin{bmatrix} x_s \\ \dot{x}_s \\ F_{env} \\ x_m \\ \dot{x}_m \\ F_{hop} \end{bmatrix}}_{\dot{z}} = \underbrace{\begin{bmatrix} 0 & 1 & 0 & & & \\ -\frac{K_s}{M_s} & -\frac{B_s}{M_s} & \frac{1}{M_s} & & 0 & \\ 0 & 0 & -\beta_{env} & & & \\ & & & 0 & 1 & 0 \\ & 0 & & -\frac{K_m}{M_m} & -\frac{B_m}{M_m} & \frac{1}{M_m} \\ & & & 0 & 0 & -\beta_{hop} \end{bmatrix}}_{A^c} \underbrace{\begin{bmatrix} x_s \\ \dot{x}_s \\ F_{env} \\ x_m \\ \dot{x}_m \\ F_{hop} \end{bmatrix}}_{z} +$$

$$\underbrace{\begin{bmatrix} 0 & 0 \\ \frac{1}{M_s} & 0 \\ 0 & 0 \\ 0 & 0 \\ 0 & \frac{1}{M_m} \\ 0 & 0 \end{bmatrix}}_{B^c} \underbrace{\begin{bmatrix} \tilde{S}_c \\ \tilde{M}_c \end{bmatrix}}_{u} + \underbrace{\begin{bmatrix} 0 & 0 \\ 0 & 0 \\ \beta_{env} & 0 \\ 0 & 0 \\ 0 & 0 \\ 0 & \beta_{hop} \end{bmatrix}}_{G^c} \underbrace{\begin{bmatrix} \hat{F}_{env} \\ \hat{F}_{hop} \end{bmatrix}}_{w} \tag{4.35}$$

and

$$Q^c = \begin{bmatrix} \sigma^2_{F_{env}} & 0 \\ 0 & \sigma^2_{F_{hop}} \end{bmatrix} \tag{4.36}$$

where $\sigma^2_{F_{env}}$ and $\sigma^2_{F_{hop}}$ are the covariances and β_{env} and β_{hop} are the bandwidths of F_{env} and F_{hop} respectively. As for the notation, the variables with $\hat{}$ and $\tilde{}$ are used to denote continuous process noise and discrete control input terms and the variables with * will be used to denote discrete measurement noise terms.

Actually, the human operator and environment forces are related when the system is in closed loop control. However, this relation is rather arbitrary, since it is a function of the existence of the contact and the properties of the object in contact. It is also a function

of the controller implemented, however at this point there is no bilateral controller in the system. Therefore, considering them as uncorrelated processes is a reasonable assumption.

Roughly speaking, each sensory configuration corresponds to a different output matrix C for the system. We will consider position, velocity, acceleration, and force measurements on the master and slave manipulators.

Position and velocity sensors give measurements of the states of (4.35):

$$\begin{bmatrix} x_{s,meas} \\ \dot{x}_{s,meas} \\ x_{m,meas} \\ \dot{x}_{m,meas} \end{bmatrix} = \begin{bmatrix} 1 & 0 & 0 & 0 & 0 & 0 \\ 0 & 1 & 0 & 0 & 0 & 0 \\ 0 & 0 & 0 & 1 & 0 & 0 \\ 0 & 0 & 0 & 0 & 1 & 0 \end{bmatrix} z + \begin{bmatrix} \delta^*_{x_s} \\ \delta^*_{\dot{x}_s} \\ \delta^*_{x_m} \\ \delta^*_{\dot{x}_m} \end{bmatrix} \tag{4.37}$$

where $\delta^*_{\cdot}$ are the measurement noise. If the quantization of the sensor is the only form of measurement noise, which is usually the case for position sensing with encoders, the covariance of the random process is $\sigma^2 = \Delta^2/12$, Δ being the quantization step size. Assuming these random processes are uncorrelated

$$R = \text{diag}\left\{ \begin{bmatrix} \sigma_{x_s}, \sigma_{\dot{x}_s}, \sigma x_m, \sigma \dot{x}_m \end{bmatrix} \right\} \tag{4.38}$$

Note that here we have directly calculated R, not by $R = R^c/T$. This is because the quantization noise itself is in discrete time, it is not the result of sampling of a continuous time random process.

Accelerometers also give measurements of the states of the system. Here, we are also including the signal conditioning filters for the accelerometers, since accelerometers are analog sensors and the signal conditioning filters are an integral part of these sensors. Then, (4.35) augmented with the low pass filter becomes

$$\underbrace{\frac{d}{dt}\begin{bmatrix} x_s \\ \dot{x}_s \\ F_{env} \\ z_4 \\ x_m \\ \dot{x}_m \\ F_{hop} \\ z_8 \end{bmatrix}}_{\dot{z}} = \underbrace{\begin{bmatrix} 0 & 1 & 0 & 0 & & & & \\ -\frac{K_s}{M_s} & -\frac{B_s}{M_s} & \frac{1}{M_s} & 0 & & & 0 & \\ 0 & 0 & -\beta_{env} & 0 & & & & \\ -\frac{\beta_{acc}K_s}{M_s} & -\frac{\beta_{acc}B_s}{M_s} & \frac{\beta_{acc}}{M_s} & -\beta_{acc} & & & & \\ & & & & 0 & 1 & 0 & 0 \\ & 0 & & & -\frac{K_m}{M_m} & -\frac{B_m}{M_m} & \frac{1}{M_m} & 0 \\ & & & & 0 & 0 & -\beta_{hop} & 0 \\ & & & & -\frac{\beta_{acc}K_m}{M_m} & -\frac{\beta_{acc}B_m}{M_m} & \frac{\beta_{acc}}{M_m} & -\beta_{acc} \end{bmatrix}}_{A^c} \underbrace{\begin{bmatrix} x_s \\ \dot{x}_s \\ F_{env} \\ a_s \\ x_m \\ \dot{x}_m \\ F_{hop} \\ a_m \end{bmatrix}}_{z} +$$

$$\underbrace{\begin{bmatrix} 0 & 0 \\ \frac{1}{M_s} & 0 \\ 0 & 0 \\ \frac{\beta_{acc}}{M_s} & 0 \\ 0 & 0 \\ 0 & \frac{1}{M_m} \\ 0 & 0 \\ 0 & \frac{\beta_{acc}}{M_m} \end{bmatrix}}_{B^c} \underbrace{\begin{bmatrix} \tilde{S}_c \\ \tilde{M}_c \end{bmatrix}}_{u} + \underbrace{\begin{bmatrix} 0 & 0 \\ 0 & 0 \\ \beta_{env} & 0 \\ 0 & 0 \\ 0 & 0 \\ 0 & 0 \\ 0 & \beta_{hop} \\ 0 & 0 \end{bmatrix}}_{G^c} \underbrace{\begin{bmatrix} \hat{F}_{env} \\ \hat{F}_{hop} \end{bmatrix}}_{w} \tag{4.39}$$

and the output equations with accelerometer measurements are

$$\begin{bmatrix} x_{s,meas} \\ \dot{x}_{s,meas} \\ \ddot{x}_{s,meas} \\ x_{m,meas} \\ \dot{x}_{m,meas} \\ \ddot{x}_{m,meas} \end{bmatrix} = \begin{bmatrix} 1 & 0 & 0 & 0 & 0 & 0 & 0 & 0 \\ 0 & 1 & 0 & 0 & 0 & 0 & 0 & 0 \\ 0 & 0 & 0 & 1 & 0 & 0 & 0 & 0 \\ 0 & 0 & 0 & 0 & 1 & 0 & 0 & 0 \\ 0 & 0 & 0 & 0 & 0 & 1 & 0 & 0 \\ 0 & 0 & 0 & 0 & 0 & 0 & 0 & 1 \end{bmatrix} z + \begin{bmatrix} \delta^*_{x_s} \\ \delta^*_{\dot{x}_s} \\ \delta^*_{\ddot{x}_s} \\ \delta^*_{x_m} \\ \delta^*_{\dot{x}_m} \\ \delta^*_{\ddot{x}_m} \end{bmatrix} \tag{4.40}$$

with

$$R = \text{diag}\left\{ \begin{bmatrix} \sigma_{x_s}, \sigma_{\dot{x}_s}, \sigma_{\ddot{x}_s}, \sigma x_m, \sigma \dot{x}_m, \sigma_{\ddot{x}_m} \end{bmatrix} \right\}. \tag{4.41}$$

Since accelerometer is an analog sensor, it has both continuous time noise and quantization noise terms. If the spectral density of the sensor noise has magnitude ρ (assuming white noise), and the quantization step size is Δ_{acc}, then the covariance of the accelerometer measurement noise is $\sigma_{\ddot{x}} = \rho^2/T + \Delta^2_{acc}/12$. Note that the sensor noise and the quantization noise are uncorrelated.

Force sensor gives a measurement of the process noise rather than the states, therefore it changes the error statistics of the process noise. For example, when we put a force sensor on the slave manipulator, the slave dynamics can be written as

$$M_s \ddot{x}_s + B_s \dot{x}_s + K_s x_s = \tilde{S}_c + \underbrace{\tilde{F}_{env} + \hat{\delta}_{F_{env}}}_{F_{env}} \tag{4.42}$$

where F_{env} is not a completely unknown variable but rather the sum of the measured force $\tilde{F}_{env}$ and the quantization of the force sensor $\hat{\delta}_{F_{env}}$. Low pass filter for the force input is no

longer needed. The state space model for the system with force sensors is

$$\underbrace{\frac{d}{dt}\begin{bmatrix} x_s \\ \dot{x}_s \\ z_3 \\ x_m \\ \dot{x}_m \\ z_6 \end{bmatrix}}_{\dot{z}} = \underbrace{\begin{bmatrix} 0 & 1 & 0 & & & \\ -\frac{K_s}{M_s} & -\frac{B_s}{M_s} & 0 & & 0 & \\ -\frac{\beta_{acc}K_s}{M_s} & -\frac{\beta_{acc}B_s}{M_s} & -\beta_{acc} & & & \\ & & & 0 & 1 & 0 \\ & 0 & & -\frac{K_m}{M_m} & -\frac{B_m}{M_m} & 0 \\ & & & -\frac{\beta_{acc}K_m}{M_m} & -\frac{\beta_{acc}B_m}{M_m} & -\beta_{acc} \end{bmatrix}}_{A^c} \underbrace{\begin{bmatrix} x_s \\ \dot{x}_s \\ a_s \\ x_m \\ \dot{x}_m \\ a_m \end{bmatrix}}_{z} +$$

$$\underbrace{\begin{bmatrix} 0 & 0 & 0 & 0 \\ \frac{1}{M_s} & 0 & \frac{1}{M_s} & 0 \\ \frac{\beta_{acc}}{M_s} & 0 & \frac{\beta_{acc}}{M_s} & 0 \\ 0 & 0 & 0 & 0 \\ 0 & \frac{1}{M_m} & 0 & \frac{1}{M_m} \\ 0 & \frac{\beta_{acc}}{M_m} & 0 & \frac{\beta_{acc}}{M_m} \end{bmatrix}}_{B^c} \underbrace{\begin{bmatrix} \tilde{S}_c \\ \tilde{M}_c \\ \tilde{F}_e nv \\ \tilde{F}_{hop} \end{bmatrix}}_{u} + \underbrace{\begin{bmatrix} 0 & 0 \\ \frac{1}{M_s} & 0 \\ \frac{1}{M_s} & 0 \\ 0 & 0 \\ 0 & \frac{1}{M_m} \\ 0 & \frac{1}{M_m} \end{bmatrix}}_{G^c} \underbrace{\begin{bmatrix} \hat{\delta}_{F_{env}} \\ \hat{\delta}_{F_{hop}} \end{bmatrix}}_{w} \tag{4.43}$$

$$\begin{bmatrix} x_{s,meas} \\ \dot{x}_{s,meas} \\ \ddot{x}_{s,meas} \\ x_{m,meas} \\ \dot{x}_{m,meas} \\ \ddot{x}_{m,meas} \end{bmatrix} = I_{6\times 6} z + \begin{bmatrix} \delta^*_{x_s} \\ \delta^*_{\dot{x}_s} \\ \delta^* \ddot{x}_s \\ \delta^*_{x_m} \\ \delta^*_{\dot{x}_m} \\ \delta^*_{\ddot{x}_m} \end{bmatrix} \tag{4.44}$$

with

$$Q^c = \begin{bmatrix} \sigma^2_{\hat{\delta}_{F_{env}}} & 0 \\ 0 & \sigma^2_{\hat{\delta}_{F_{hop}}} \end{bmatrix} \tag{4.45}$$

and

$$R = \text{diag}\left\{ \begin{bmatrix} \sigma_{x_s}, \sigma_{\dot{x}_s}, \sigma_{\ddot{x}_s}, \sigma x_m, \sigma \dot{x}_m, \sigma_{\ddot{x}_m} \end{bmatrix} \right\} \tag{4.46}$$

where $\sigma^2_{\hat{\delta}_{F_{env}}} = \Delta_F^2/12$ and $\sigma^2_{\hat{\delta}_{F_{hop}}} = \Delta_F^2/12$.

Analysis Method

The algorithm to compare the sensory configurations is as follows.

1. For each of the sensory configurations :

(a) Construct the continuous time state space model (A^c, B^c, G^c, C)

(b) Calculate the discrete time equivalent of the system (A, B, G, C)

(c) Construct the noise covariance matrices Q, R

(d) Calculate the *a priori* error covariance matrix P using (4.32)

(e) Calculate the *a posteriori* error covariance matrix P^+ using (4.33)

(f) Calculate the norm of the submatrix of P^+ corresponding to the states $(x_s, \dot{x}_s, F_{env}, x_m, \dot{x}_m, F_{hop})$

2. The relative values of the calculated norms give a quantitative estimate for the achievable performance with the sensory configurations.

At step (f) we are calculating the norm of the submatrix of P^+ corresponding the states inherent to the system in order to have a fair comparison.

The advantages of this method over the one introduced in section 4.4.1 are: 1) there is no assumed control architecture; 2) sensor noise, which is an important factor in teleoperator performance, is explicitly included in the analysis. However, this method is indirect, i.e. it doesn't directly give the relative achievable performances but rather look at an indirect indicator of performance, namely the best possible *a posteriori* error covariance achievable.

4.5 Case Study

In this section, the analysis and design methodology developed in sections 4.3 and 4.4 is applied to a teleoperation testbed. The testbed used is a teleoperation system with two identical three degree of freedom (DOF) robotic manipulators, Phantom v1.5 haptic interfaces (Sensable Technologies, Cambridge, MA) with custom motor drive electronics (See Fig. 4.15). The analysis here is carried out with a one DOF model, along the vertical direction, which is the axis orthogonal to the surface of the deformable body being manipulated. The local linear model of the manipulator in the vertical direction around the operating region is estimated as[3]

$$\frac{X}{F} = \frac{1}{9.641e^{-5}s^2 + (0.002665 + D_x)s + 0.0322} \tag{4.47}$$

[3]All the units are in Newtons for force and mm for distance.

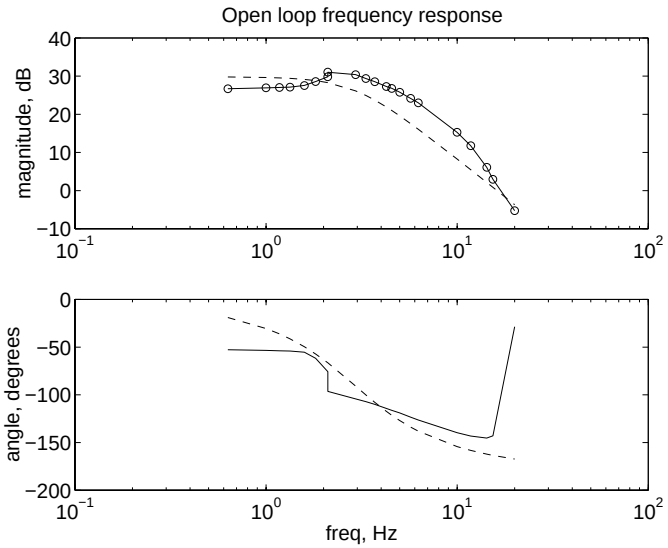

Figure 4.8: Experimentally measured frequency response of the robotic manipulator (solid line) and response of the model (dashed line)

where D_x is the active damping used. This model is constructed by black box system identification. The experimentally measured frequency response used in system identification and response of the model are shown in Fig. 4.8. In this study, active damping of $D_x = 5 \times 10^{-4}$ has been used on the slave side to improve the stability of the manipulator, unless otherwise noted.

Control Design with Task Based Optimization

The following environment and operator impedance variations are considered

$$Z_e \in \{(B_e s + 1)K_e : B_e \geq 0.05, 0 \leq K_e < \infty\}, \tag{4.48}$$

$$Z_{hop} \in \{(0.0219s + 1)K_{hop} : 0.2 \leq K_{hop} \leq 2\} \tag{4.49}$$

with nominal impedances

$$\hat{Z}_e = 0.35(0.05s + 1) \tag{4.50}$$

$$\hat{Z}_{hop} = 1.51(0.0219s + 1). \tag{4.51}$$

The following empirically determined upper bounds for the uncertainty terms are used in the stability analysis (Fig.4.9)

$$\Phi(s) = 10^{3.8/20} \left(\frac{\frac{s}{19} + 1}{\frac{s}{80} + 1} \right)^2 \left(\frac{\frac{s}{125} + 1}{\frac{s}{75} + 1} \right)^3 \tag{4.52}$$

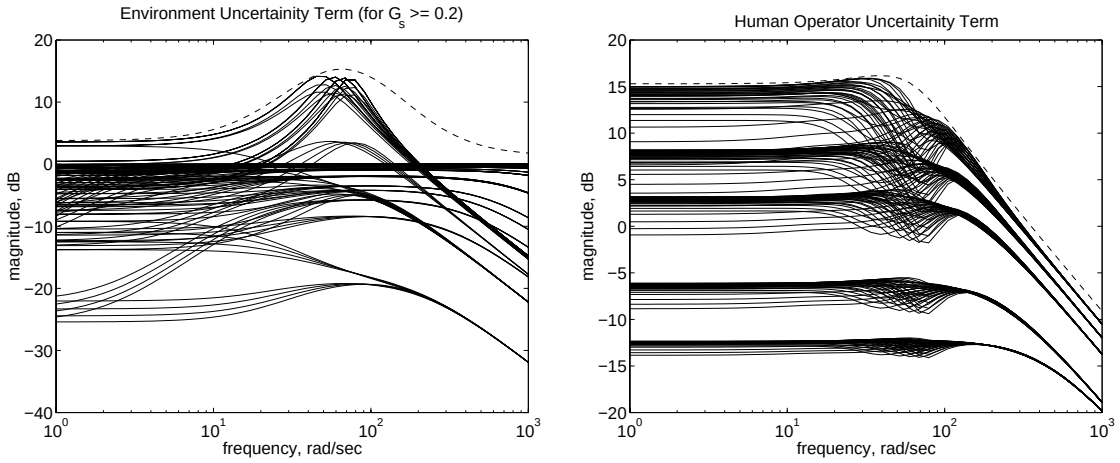

(a) (b)

Figure 4.9: Uncertainty weighting functions: (a) Environment uncertainty term (b) Human operator uncertainty term. Dashed line is the upper bound for the uncertainty. Solid lines are the variations in the environment / human operator terms.

$$W_{uh}(s) = 10^{15.3/20}\left(\frac{\frac{s}{60}+1}{(s^2+20.760s+60^2)/60^2}\right). \tag{4.53}$$

And the upper bound used for tracking sensitivity function is given by

$$b(s) = \left(\frac{9.64\times10^{-5}+3.66\times10^{-3}s+0.032}{9.64\times10^{-5}+3.66\times10^{-3}s+0.232}\right)\left(\frac{\frac{s}{70}+1}{\frac{s}{100}+1}\right)^8\left(\frac{\frac{s}{138}+1}{\frac{s}{100}+1}\right)^8 \tag{4.54}$$

This upper bound requires good position tracking at low frequencies where the voluntary hand movements occur. (Fig. 4.10).

It is important to note that the stability analysis performed with these upper bounds is conservative in the sense that it doesn't completely capture the dependence of the uncertainty weighting function to the known variables, such as controller gains. For example, the bound in (4.52) is chosen to be a constant transfer function, whereas it is actually possible to pick an upper bound which is a function of the controller gains . This dependence is a nontrivial function of controller gains, so a constant upper bound is used here.

It is also possible to find a single upper bound for the combined environment and operator uncertainties. However, the combined bound would have been completely independent of controller gains, whereas the bound constructed from pieces have some

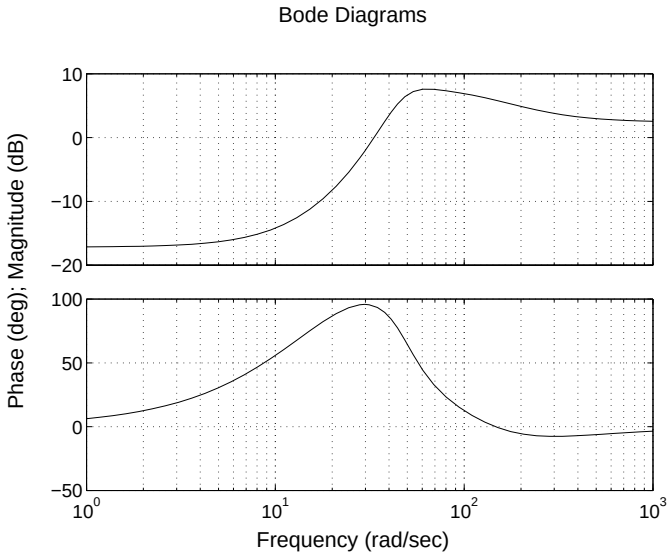

Figure 4.10: Upper bound for forward position loop tracking sensitivity

(even though not complete) dependence from

$$\left| \frac{1}{h_{22}\hat{Z}_e} \frac{Z_e - \hat{Z}_e}{\frac{1}{h_{22}} + Z_e}(j\omega) \right| < \left| \frac{1}{h_{22}\hat{Z}_e} \Phi(j\omega) \right| \tag{4.55}$$

since h_{22} is a function of controllers.

The fidelity plots for the KFF and PERR controllers superimposed with isostability curves are shown in Fig. 4.11. The fidelity-stability trade-off can easily be observed on these plots, as the stability degrades as fidelity improves.

Comparison of Sensors

For this system, the resulting *alpha*-curve is shown in Fig. 4.12. This curve predicts that using a force sensor will improve the performance and the KFF algorithm will perform best for the choice of the fidelity measure, tracking requirements, and the uncertainty bounds considered.

For the Kalman filter analysis, we consider the following parameters :

$$K_s = K_m = 0.0322 \tag{4.56}$$

$$B_s = B_m = 0.002665 \tag{4.57}$$

$$M_s = M_m = 9.641 \times 10^{-5} \tag{4.58}$$

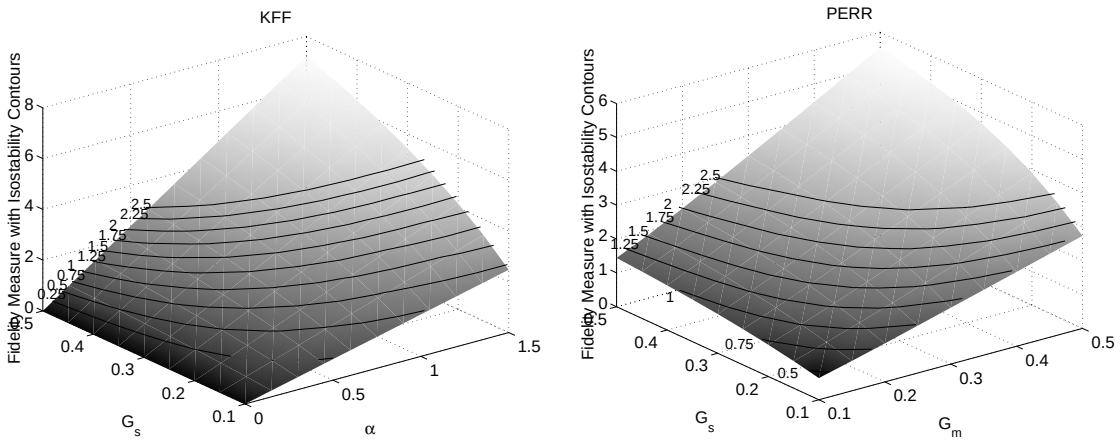

(a) (b)

Figure 4.11: Fidelity of the PERR and KFF architectures as a function of controller parameters. Contours of constant stability are shown overlaid on the fidelity surface for comparison. Note that stability decreases as fidelity increases.

which are from the manipulator model of (4.47). We assume

$$\beta_{hop} = 5\text{Hz} \tag{4.59}$$

$$\beta_{env} = 100\text{Hz} \tag{4.60}$$

$$\sigma^2_{F_{hop}} = 1 \tag{4.61}$$

$$\sigma^2_{F_{env}} = 1. \tag{4.62}$$

The following noise values are for the sensors present on the experimental testbed

$$\Delta_{pos} = 0.03 \tag{4.63}$$

$$\Delta_{acc} = 11.98 \tag{4.64}$$

$$\beta_{acc} = 200\text{Hz} \tag{4.65}$$

$$\rho = 24.06 \tag{4.66}$$

$$\Delta_F = 0.025. \tag{4.67}$$

There is no velocity sensor available on our testbed.

The result of the Kalman filter analysis for this system are shown in Fig. 4.13 comparing the following sensor configurations:

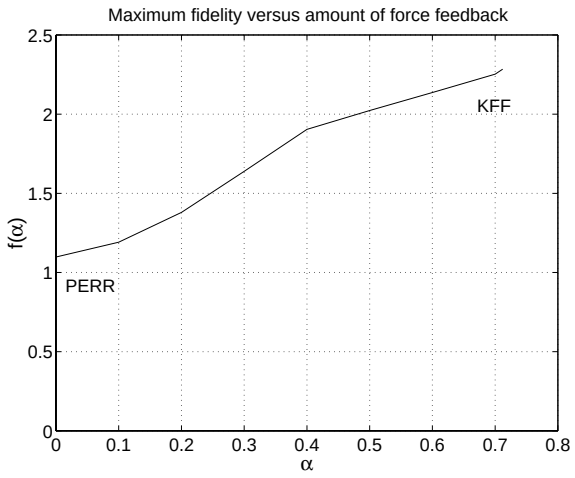

Figure 4.12: *Alpha*-curve for the teleoperation system studied

Controller	Master	Slave
	position	position
	position + force	position
	position	position + force
	position + force	position + force
	position + acceleration	position + acceleration
	position + acceleration + force	position + acceleration
	position + acceleration	position + acceleration + force
	position + acceleration + force	position + acceleration + force

Results predict that addition of force sensors and accelerometers will improve the performance, and relative improvement by adding accelerometers is less than a force sensor on the slave manipulator but it is more than using a force sensor on the master manipulator. Results also suggest that if there will be a single force sensor, it is more desirable to put it on the slave side rather than the master. This is because the assumed bandwidth of environment force is wider than the bandwidth of the human hand motion. It is important to note that the analog noise of the force sensor is not included in the analysis since there was no data available on its statistics, whereas the analog noise of the experiments accelerometers is included.

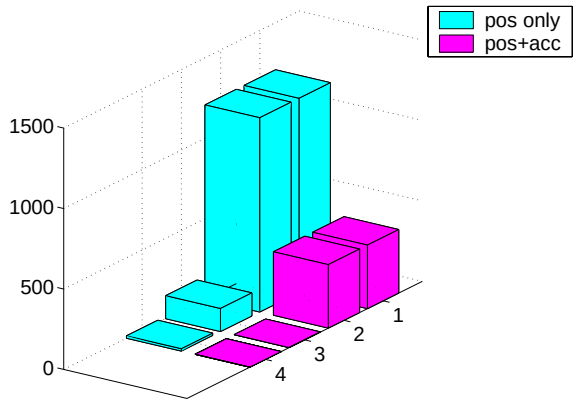

Figure 4.13: Result of the Kalman filter analysis for the teleoperation system studied. Vertical axis is the induced 2-norm of the *a posteriori* error covariance matrix. Sensor configuration 1 through 4 correspond to no force sensor, force sensor on master only, force sensor on slave only, and force sensor on master and slave cases respectively.

4.6 Experimental Evaluation of Teleoperation Controllers

Experimental evaluation of the controllers is a necessary step in design of teleoperation systems, as it is always important to test a human-in-the-loop system with actually running it with the human in the loop.

In our , we have used an inclusion detection task to simulate the palpation of soft tissue during surgery. The subjects are asked to identify the location of a metal inclusion embedded inside a silicon gel by probing it with the teleoperation system. As the control data, the subjects are also asked to locate the same inclusions with a rigid probe, which is the ideal teleoperator model. [85]

Three different bilateral controllers were tested in the experiment, all designed using the design method described in section 4.3. The first one is KFF, where the force measured with the force sensor is used as the force feedback. In PERR, the force displayed on the master side is a force estimate based on the position error between the master and slave manipulators rather than an actual measured force. The P+FF algorithm is a superset of the two, where the force feedback is a linear combination of the force measurement and the position error. (Fig. 4.6). The fidelity values of the controllers are given in table 4.1.

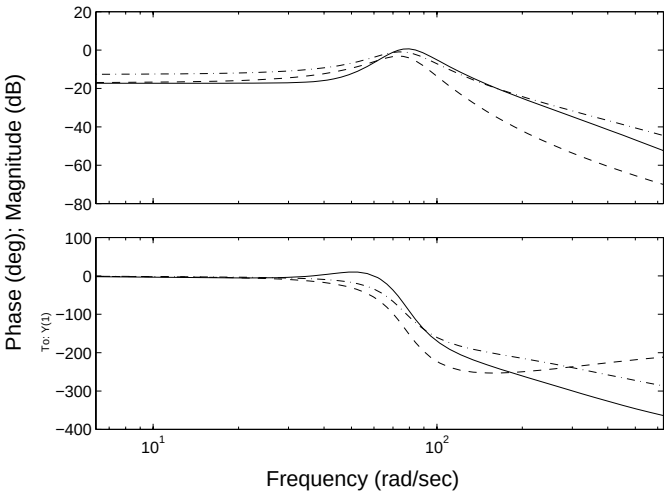

Figure 4.14: Frequency dependence of (unweighted) transmitted impedance sensitivity dZ_t/dZ_{env} at $Z_{env} = \hat{Z}_{env}$. Solid line: KFF, dashed line: PERR, dash-dot line: P+FF.

Control Architecture	Fidelity Measure
P+FF	3.12
KFF	2.78
PERR	1.91

Table 4.1: Fidelity values for the controllers used in the experiment.

4.6.1 Method

Experimental Setup

The experimental setup is shown in Fig. 4.15. The master and slave manipulators were two identical Phantom v1.5 3 DOF robotics manipulators (Sensable Technologies, Cambridge, MA). These devices were controlled by a dual processor SGI Octane workstation running IRIX and Sensable Technologies OS Extender as the real time kernel. The digital controller was running at 1 kHz. The slave manipulator was equipped with a 6 DOF force/torque sensor (Assurance Technologies, Inc., Gamer, NC), which was installed between the tip of the slave manipulator and the end effector. The force sensor had a 540 Hz sampling time with time delay of approximately 6 msec. The slave manipulator had a rigid plastic hemisphere of 2 cm diameter as the end effector. The master manipulator had a plastic stylus handle as its end effector. The subjects were using a pen grip to hold this stylus

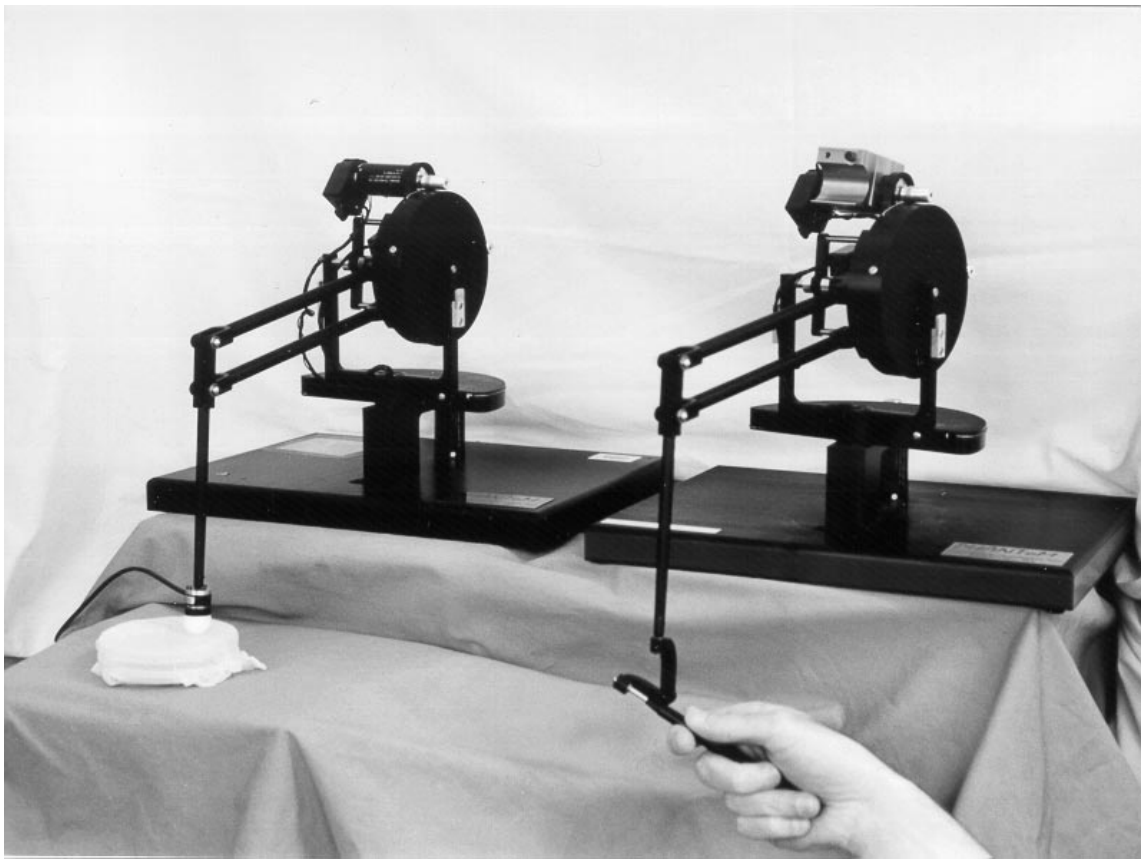

Figure 4.15: Setup for teleoperation experiments

handle.

Soft gel molds with embedded metal rods were used to simulate soft tissue with an inclusion (Fig. 4.16). Each sample was a wax block with a well containing silicone gel (GE RTV 6166). The dimensions of the well were 1.8 cm deep, 12 cm long and 4.5 cm wide. Each sample contained a 1/4 inch diameter metal rod inclusion along the width of the well. The rod was placed 3 cm from the wall of the well. The inclusion depths of 0.8 cm, 1.0 cm, 1.2 cm, and 1.4 cm were used for the four samples in this experiment. A latex glove covered the top surface of the gels to protect the surface of the gel from tearing.

Experimental Task

Subjects were asked to determine which half of the gel sample contained the inclusion by scanning the surface of the gel along the long axis (Fig. 4.16), a alternative forced

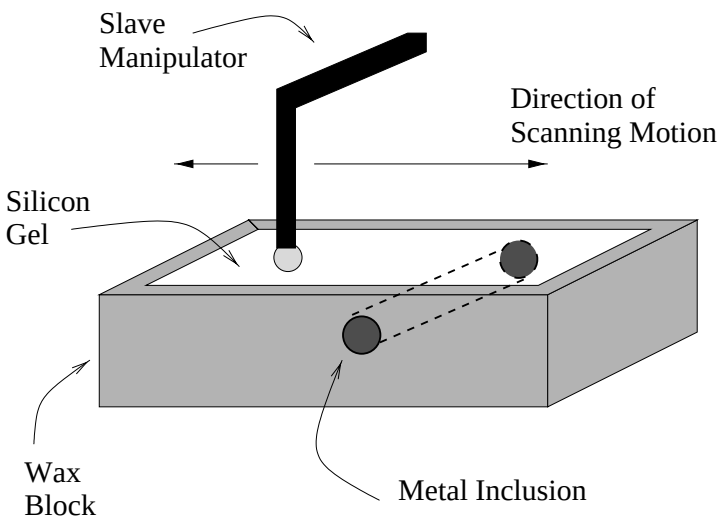

Figure 4.16: Experimental task

choice task. The slave manipulator was not visible to the subject to prevent the use of visual cues. The range of movement of the operator was limited to the boundaries of the gel sample by putting a cardboard restraint on the master side (not shown in Fig. 4.15). The center of the gel sample was marked on the cardboard restraint, so that the subjects would be aware o which part of sample they are probing. In each trial subjects had 10 seconds, marked by auditory cues at the beginning and the end, to scan the surface of the gel sample. The subjects were then asked to tell which half of the sample contained the inclusion.

Three subjects participated in this experiment. Each of the subjects had 10 or more hours of experience using the teleoperation system in similar inclusion detection tasks. All subjects participated in a training period before beginning the experimental trials to minimize learning effects during the experiment. During training, subjects were able to practice the task using all three controllers and all gel samples for several trials. The slave was not hidden from the view of the subject during training so that the subjects could understand how the apparatus functioned.

Each subject completed $3 \times 4 \times 20 = 240$ trials (twenty trials with each of the three control architectures and four gel samples). In order to avoid problems with fatigue, each subject participated in two sets of the 120 trials, separated by at least one day, and they were given three ten minute breaks during each set. Each of the 120 trial sets took approximately

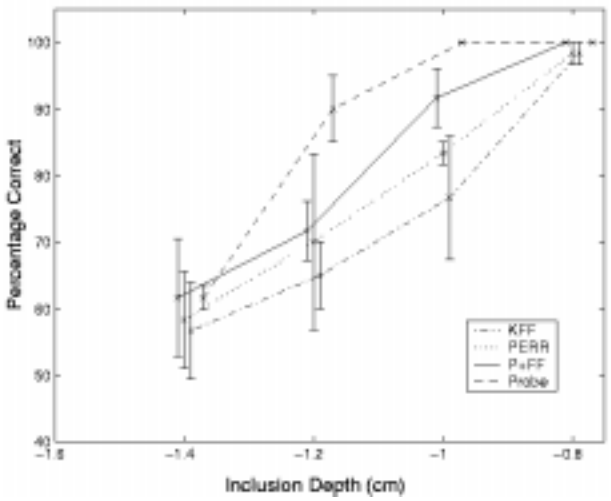

Figure 4.17: Percentage correct (mean ± standard error) versus inclusion depth

two hours to complete. The gels were presented in a pseudo random order. The subjects' responses were collected for each trial. From this data the controllers' performance were analyzed and compared.

The subjects also performed the detection task using a hand-held probe, in addition to the teleoperative system. The probe consisted of a pen-length shaft with a spherical plastic tip of the same diameter as the end effector of the slave manipulator. Subjects held the probe with a pen grip and scanned the surface of the gel. A cloth drape was used to prevent the subjects from seeing their hand or the sample. Each subject performed 80 trials (20 repetitions on each of 4 samples) with the hand-held probe. This data was used as the base line against which the fidelity of the controller architectures was compared.

4.6.2 Results

First of all, the experiments validated the control design methodology described in section 4.3. The resulting controllers were all stable and within the specifications.

Fig. 4.17 summarizes the results of the experiments. It shows the four psychometric curves, for the three controllers and the rigid probe, which show the averaged data among the subjects, the percentage of trails the subjects correctly located the inclusion with respect to the inclusion depth. As expected, the probe, which is the ideal teleoperator, performed best. Among the teleoperated systems, qualitatively it appears that subjects

were able to locate the inclusion best with the P+FF controller, followed by the PERR and KFF controllers respectively. This shows that, for the setup we have, using a force sensor improved the performance. One discrepancy from the theoretical expectations is that PERR performed better than KFF. This was due to the dynamic properties and the noise of the force sensor which were not included in the analysis.

Statistical analysis performed on the data reveal that inclusion depth, as expected, is a significant factor in the outcome (getting a correct response). Controller and subject, although to a lesser extent, also contribute to the deviance in the model. Pairwise comparison between controllers reveal that the performance of PERR is not statistically different from KFF or P+FF, and although the difference between P+FF and KFF is statistically significant, it is not as large as desired. (Details of the statistical analysis of the data can be found in [85, 84].)

Familiarity with the task and haptic devices in general, and personal strategy were the important factors affecting the results of this experiment. Pilot experiments revealed a larger variability between subjects than expected and that learning during the experiment was a significant factor. Ten subjects participated in the pilot experiments, where they performed a more complex detection task involving scanning in two dimensions. In the pilot experiments, the subjects tended to change strategies, and they would converge on one strategy only after extensive training. Therefore, in order to reduce variations among subjects, and training effects, only highly trained subjects with more than ten hours of experience in using haptic devices to interact with compliant objects were used in the final experiments, which significantly limited the available pool of subjects. The experimental task was also simplified to scanning only in one dimension to reduce the effects of personal strategy. However, the small number of subjects used yielded results which are not as statistically significant as desired.

4.7 Discussion and Conclusion

In this chapter, we have developed a theoretical and experimental framework to design and compare bilateral teleoperation controllers for high fidelity telemanipulation of deformable objects with special emphasis on the requirements of telesurgery. The analysis and design methods are general, in the sense that they are not limited to the existing RTW hardware, but can be applied to future teleoperator designs with novel sensors and

actuators.

It is important to note that the stability measure developed here is on the conservative side, mainly due to modeling errors in the weighting functions. It was possible to manually increase the gains of the physical setup and still maintain stability. It would be more appropriate to use a structured uncertainty model to best capture this kind of uncertainty. Linear fractional transformations may be used to develop a less restrictive uncertainty model.

The particular results given in section 4.5 may not be generally applicable to all systems, since the analysis results depend on the particular manipulators used. Every teleoperation system needs to be analyzed individually since the results highly depend on the dynamic properties of the manipulators as well as the sensors.

The results of the experimental comparison of the teleoperation controllers can be further improved by using an experimental task where high frequency force information is more important. As it can be seen from the Fig. 4.14, the difference between the controllers are more significant in the high frequency range. Also the psychophysical studies in [32] suggest that the human operator is more sensitive o changes in stimuli at high frequencies. Such a task would be detection or distinguishing of inclusions with different sizes, which effectively changes the spatial frequency of the stiffness stimuli presented to the subjects. Smaller inclusions result in higher spatial frequency which in turn give higher spatial temporal frequency during scanning of the gel.

Modeling of the dynamical characteristics and the noise of the force sensor is necessary for a better comparison of the sensory schemes and more general results.

As the final words, we would like to reemphasize two important points: 1) It is important to have task based performance goals rather than trying to achieve a marginally stable, physically unachievable ideal teleoperator response. 2) Design of the teleoperation system must be based on human perceptual capabilities. For this, it is necessary to quantify human perceptual capabilities, and to have means to incorporate them into the control design (design methodology, tools, and proper formulation). This study addresses these two points by proposing a new fidelity measure for the compliance discrimination task, and developing a design methodology using robust control theory for task-based optimization of the teleoperation controller, focusing on telemanipulation of deformable objects.

Part II

Surgical Simulation

Chapter 5

Dynamic Simulation of Deformable Objects in Virtual Environments

In this chapter we will have a broad look at the dynamic simulation of deformable objects in virtual environments, focusing on the physical formulation of the problem, establishing a unifying framework where the various modeling methodologies can be compared, and briefly going over the basic problems.

There are essentially three different approaches in the literature to deformable tissue modeling.

- Lumped element models
- Linear finite element models
- Nonlinear continuum models

Lumped element models (LEM) are meshes of mass, spring and damper elements [35, 98, 69]. They are the most popular models for real time surgical simulators, because they are natural extensions of other deformable models used in computer animation, they are conceptually simple, and it is possible to construct models which can be simulated at interactive speeds with these type of models. A common problem with the lumped parameter models used in literature is the selection of component parameters, spring and damper constants, and nodal mass values. There is no physically based or systematic method in the literature to determine the element types or parameters from physical data or known constitutive behavior. The typical practice in the literature is somewhat *ad hoc*,

the element types and connectivities are empirically assumed, usually based on the structure of the geometric model at hand, and the element parameters are either hand tuned to get a reasonable looking behavior or estimated by a parameter optimization method to fit the model response to an experimentally measured response. For example, Joukhadar et. al. [54, 55] use a predefined mesh topology and then determine the element parameters with a search using genetic algorithms.

Linear finite element models (FEM) are used as a step to get closer using models with physically based parameters [13, 48, 26]. Linear finite element models are computationally attractive as superposition can be used and it is possible to perform extensive off-line calculations to significantly reduce the real-time computational burden. However, linear models are based on the assumption of small deformation, typically less than 1%, which is not valid for much of the soft tissue manipulation during surgery. These models cannot handle rigid motions either. Linear models loose their computational advantage under topology changes, e.g. as a result of cutting, as the off-line calculations cannot be used. To address this last problem, Delingette [31] proposed to use lumped element models locally where there is topological change (such as cutting) and use a linear finite element model for the rest.

Nonlinear continuum models are highly accurate models, which take into account nonlinear constitutive behaviors of the materials as well as large deformation effects. These models are computationally very intensive and therefore not suitable for real-time simulation in their current form. [24, 25, 111].

5.1 Continuum Equations for Elastic Bodies

In order to be able to systematically study the methods mentioned above, we will first formulate the underlying physical problem.

Consider the deformable body $\mathcal{B}$, which is a regular region in $\mathbf{R}^3$. $\mathcal{B}$ is also called the reference configuration. $\mathbf{p} \in \mathcal{B}$ are the body coordinates of the material points. A deformation $\mathbf{f} : \mathcal{B} \to \mathbf{R}^3$ of a body is a one-to-one smooth mapping that maps each material point $\mathbf{p}$ to a point $\mathbf{x} = \mathbf{f}(\mathbf{p})$ in spatial frame. A motion $\mathsf{x} : \mathcal{B} \times \mathbf{R} \to \mathbf{R}^3$ of a body is a $\mathcal{C}^3$ function where for each t, $\mathsf{x}(\mathbf{p}, t)$ is a deformation. (See Fig. 5.1)

The total Lagrangian form of the field equations that govern the dynamic behavior

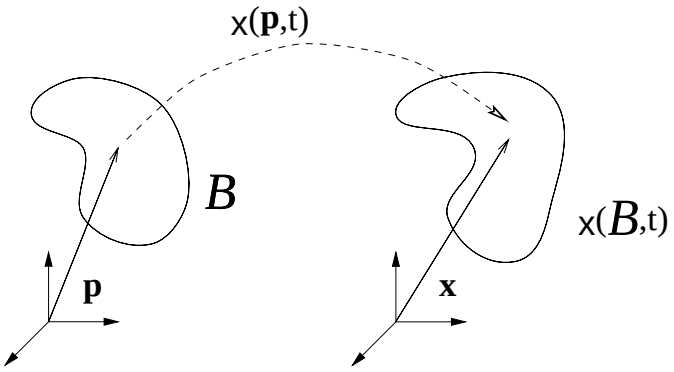

Figure 5.1: Motion of a body

of elastic bodies are given by [40, 41, 67]

$$\begin{aligned} S &= F\bar{S}(C) \\ C = F^T F\,,\ F &= \nabla \mathsf{x} \\ \mathrm{Div}\, S + \mathbf{b}_0 &= \rho_0 \ddot{\mathsf{x}} \ \text{ in } \ \mathcal{B} \end{aligned} \tag{5.1}$$

where F is the deformation gradient, S is the Piola-Kirchhoff stress tensor, C is the right Cauchy-Green strain tensor, $\mathbf{b}_0$ is the body force, ρ_0 is the mass density at the reference configuration, and ∇ and Div are respectively the gradient and divergence operators in body coordinates. These field equations are derived from the empirical physical laws, such as conservation of mass and momentum, and the independence of the response from observer. The first equation is where the material properties are included.

The boundary value problems in finite elasticity are obtained by combining the basic system of field equations given by equation (5.1) with suitable initial and boundary conditions. Initial conditions are usually specified by the initial motion and velocity. The type of boundary value problem typically encountered in our application is specified with:

$$\mathsf{x}(\mathbf{p}, 0) = \mathsf{x}_0(\mathbf{p})\,,\ \dot{\mathsf{x}}(\mathbf{p}, 0) = \mathbf{v}_0(\mathbf{p}) \tag{5.2}$$

where x_0 and $\mathbf{v}_0$ are prescribed functions on $\mathcal{B}$. For boundary conditions, two complimentary regular subsets $\mathcal{S}_1$ and $\mathcal{S}_2$ of $\partial\mathcal{B}$, with $\partial\mathcal{B} = \mathcal{S}_1 \cup \mathcal{S}_2$, $\mathcal{S}_1^o \cap \mathcal{S}_2^o = \emptyset$ are given, where the motion is prescribed on $\mathcal{S}_1$ and the surface traction is prescribed on $\mathcal{S}_2$:

$$\mathsf{x} = \bar{\mathsf{x}} \ \text{ on } \mathcal{S}_1 \times [0, \infty)\,, \quad S\mathbf{n} = \bar{\mathbf{s}} \ \text{ on } \mathcal{S}_2 \times [0, \infty). \tag{5.3}$$

The boundary value problem that needs to be solved or simulated in real time in order to model the deformation of elastic tissue is given by the system of equations (5.1, 5.2 , 5.3).

5.2 Models for the Elastic Bodies - Discretization of the Field Equations

For the solution of the boundary value problem specified by (5.1, 5.2 , 5.3) in the previous section, the partial differential equation (PDE) needs to be spatially and temporally discretized. Typically, the PDE is first discretized in space to construct a large system of ordinary differential equations, in the form of an initial value problem, which is later approximately solved in time by numerical integration methods. Please refer to [80] and [8] for detailed treatments of the finite elements method, [90] for a detailed treatment of the finite differences method, and [79] and [8] for details of time discretization.

5.2.1 Finite Differences Model

Finite difference models are not used very much for solid mechanics problems since they require uniform meshes. This method is briefly introduced here for our problem to make some observations later on in the discussion.

We will assume that there is a uniform mesh covering the reference configuration of the deformable body.[1] We will denote the value of a variable at the I, J, K'th node of the mesh as $\mathbf{x}^{IJK} = \mathsf{x}(\mathbf{p}^{IJK})$. The differential operator to be discretized using finite difference approximation is

$$(\mathrm{Div}\, S)_i = \sum_j \frac{\partial S_{ij}}{\partial \mathsf{p}_j}. \tag{5.4}$$

At I, J, K'th node

$$\begin{aligned}
(\mathrm{Div}\, S)_i &\approx (\frac{\partial S_{i1}}{\partial \mathbf{p}_1})^{IJK} + (\frac{\partial S_{i2}}{\partial \mathbf{p}_2})^{IJK} + (\frac{\partial S_{i3}}{\partial \mathbf{p}_3})^{IJK} && (5.5)\\
&= \frac{S_{i1}^{I+1JK} - S_{i1}^{I-1JK}}{\mathbf{p}_1^{I+1JK} - \mathbf{p}_1^{I-1JK}} + \frac{S_{i2}^{IJ+1K} - S_{i2}^{IJ-1K}}{\mathbf{p}_2^{IJ+1K} - \mathbf{p}_2^{IJ-1K}} + \frac{S_{i3}^{IJK+1} - S_{i3}^{IJK-1}}{\mathbf{p}_3^{IJK+1} - \mathbf{p}_3^{IJK-1}} && (5.6)\\
&= \frac{S_{i1}^{I+1JK} - S_{i1}^{I-1JK}}{2\Delta\mathbf{p}_1} + \frac{S_{i2}^{IJ+1K} - S_{i2}^{IJ-1K}}{2\Delta\mathbf{p}_2} + \frac{S_{i3}^{IJK+1} - S_{i3}^{IJK-1}}{2\Delta\mathbf{p}_3} && (5.7)
\end{aligned}$$

[1] Note that extension of the finite difference method to non-uniform meshes is not trivial.

as $S = \bar{S}(C) = \bar{S}(\nabla \mathrm{x}^T \nabla \mathrm{x}) = \tilde{S}(\nabla \mathrm{x})$ we can write

$$= \frac{\tilde{S}_{i1}(\nabla \mathbf{x}^{I+1JK}) - \tilde{S}_{i1}(\nabla \mathbf{x}^{I-1JK})}{2\Delta \mathbf{p}_1} + \frac{\tilde{S}_{i2}(\nabla \mathbf{x}^{IJ+1K}) - \tilde{S}_{i2}(\nabla \mathbf{x}^{IJ-1K})}{2\Delta \mathbf{p}_2} \tag{5.8}$$

$$+ \frac{\tilde{S}_{i3}(\nabla \mathbf{x}^{IJK+1}) - \tilde{S}_{i3}(\nabla \mathbf{x}^{IJK-1})}{2\Delta \mathbf{p}_3} \tag{5.9}$$

where

$$(\nabla \mathbf{x})_{ij}^{IJK} = \frac{\mathbf{x}_i^{I+\delta_{Ij}J+\delta_{Jj}K+\delta_{Kj}} - \mathbf{x}_i^{I-\delta_{Ij}J-\delta_{Jj}K-\delta_{Kj}}}{2\Delta \mathbf{p}_j}. \tag{5.10}$$

$\delta_{Ii} = \begin{cases} 1, \text{ if } I = i \\ 0, \text{ if } I \neq i \end{cases}$ is the Kronecker delta.

For the individual nodes, the equation of motion is in the form

$$\rho_0 \ddot{\mathbf{x}}^{IJK} = h(\mathbf{x}) \tag{5.11}$$

$\mathbf{x}$ is the vector of nodal variables. When all the equations of motion are assembled, it results in a sparse system of ordinary differential equations (ODE).

Topology of Equations

Connectivity of the equations of the motion of the nodal variables depends on the approximation used for the differential operator (divergence). For the particular approximation of the divergence operator used above, the "force" on the node IJK depends on the nodal variable shown in Fig. 5.2.

5.2.2 Finite Elements Model

Variational form of the PDE is

$$\int_{\mathcal{B}} \xi \cdot (\rho_0 \ddot{\mathrm{x}} - \mathbf{b}_0 - \mathrm{Div}\, S) dV + \int_{\mathcal{S}_2} \xi \cdot (S\mathbf{n} - \bar{\mathbf{s}}) dA = 0. \tag{5.12}$$

Divergence theorem gives

$$\int_{\mathcal{B}} \xi \cdot (\mathrm{Div}\, S) dV = \int_{\mathcal{S}} \xi \cdot S\mathbf{n} dA - \int_{\mathcal{B}} S \cdot \nabla \xi dV \tag{5.13}$$

$$= \int_{\mathcal{S}_2} \xi \cdot S\mathbf{n} dA - \int_{\mathcal{B}} S \cdot \nabla \xi dV. \tag{5.14}$$

Substituting this in the variational form, we get

$$\int_{\mathcal{B}} \xi \cdot \rho_0 \ddot{\mathrm{x}} dV + \int_{\mathcal{B}} S \cdot \nabla \xi dV = \int_{\mathcal{B}} \xi \cdot \mathbf{b}_0 dV + \int_{\mathcal{S}_2} \xi \cdot \bar{\mathbf{s}} dA \tag{5.15}$$

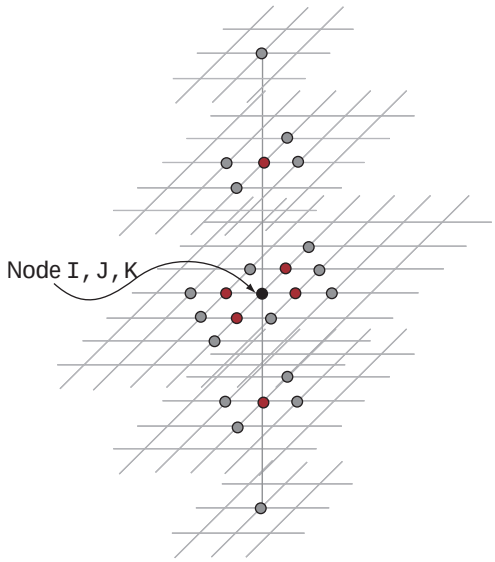

Figure 5.2: The "force" on the node IJK depends on the nodal variables shown here.

for the weak form of the PDE over the whole body.

Now consider the following finite element approximation on each element

$$\mathsf{x}(\mathbf{p},t) = \sum_{I=1}^{\mathrm{NEN}} N_I^e \mathbf{x}_I^e(t) \tag{5.16}$$

$$\xi(\mathbf{p},t) = \sum_{I=1}^{\mathrm{NEN}} N_I^e \xi_I^e(t) \tag{5.17}$$

where N_I^e, $I = 1..\mathrm{NEN}$, is the isoparametric set of approximation functions. We can write these in the matrix form as

$$\mathsf{x}^e = \left[\begin{array}{cccc} N_1^e I & N_2^e I & \cdots & N_{\mathrm{NEN}}^e I \end{array} \right] \left[\begin{array}{c} \mathbf{x}_1^e \\ \mathbf{x}_2^e \\ \vdots \\ \mathbf{x}_{\mathrm{NEN}}^e \end{array} \right] = N^e \hat{\mathbf{x}}^e \tag{5.18}$$

$$\xi^e = N^e \hat{\xi}^e \tag{5.19}$$

$$\nabla\xi \rightarrow \left[\begin{array}{ccccccccc} \xi_{1,1}^e & \xi_{2,2}^e & \xi_{3,3}^e & \xi_{1,2}^e & \xi_{2,3}^e & \xi_{3,1}^e & \xi_{1,3}^e & \xi_{2,1}^e & \xi_{3,2}^e \end{array} \right]^T = B^e \hat{\xi}^e \tag{5.20}$$

$$B^e = \left[\begin{array}{cccc} B_1^e & B_2^e & \cdots & B_{\mathrm{NEN}}^e \end{array} \right] \tag{5.21}$$

$$B_I^e = \begin{bmatrix} N_{I,1}^e & 0 & 0 \\ 0 & N_{I,2}^e & 0 \\ 0 & 0 & N_{I,3}^e \\ N_{I,2}^e & 0 & 0 \\ 0 & N_{I,3}^e & 0 \\ 0 & 0 & N_{I,1}^e \\ N_{I,3}^e & 0 & 0 \\ 0 & N_{I,1}^e & 0 \\ 0 & 0 & N_{I,2}^e \end{bmatrix}. \tag{5.22}$$

Here we have used the subscript notation, for example $\xi_{3,1}^e$ is the partial derivative of the third component of ξ^e with respect to its first variable. Substituting all of the above in the weak form,

$$\hat{\xi}^{eT}\left[\int_{\Omega_0^e} N^{eT}\rho_0 N^e dV\right]\ddot{\hat{\mathbf{x}}}^e + \hat{\xi}^{eT}\left[\int_{\Omega_0^e} B^{eT} S(N^e\hat{\mathbf{x}}^e)dV\right] = \tag{5.23}$$

$$\hat{\xi}^{eT}\left[\int_{\Omega_0^e} N^{eT}\mathbf{b}_0 dV\right] + \hat{\xi}^{eT}\left[\int_{\partial\Omega_0^e} N^{eT}\bar{\mathbf{s}}dA\right] \tag{5.24}$$

which can be written compactly as

$$\hat{\xi}^{eT}\left[M^e\ddot{\hat{\mathbf{x}}}^e + R^e(\hat{\mathbf{x}}^e) - F^e\right] = \hat{\xi}^{eT}\int_{\partial\Omega_0^e - \mathcal{S}_{20}} N^{eT}\bar{\mathbf{s}}dA \tag{5.25}$$

where

$$\begin{array}{ll} M^e = \int_{\Omega_0^e} N^{eT}\rho_0 N^e dV & \text{is the element mass matrix,} \\ R^e = \int_{\Omega_0^e} B^{eT} S(N^e\hat{\mathbf{x}}^e)dV & \text{is the stress divergence term,} \\ F^e = \int_{\Omega_0^e} N^{eT}\mathbf{b}_0 dV + \int_{\partial\Omega_0^e\cap\mathcal{S}_{20}} N^{eT}\bar{\mathbf{s}}dA & \text{is the external force vector.} \end{array} \tag{5.26}$$

As $\hat{\xi}^e$ is arbitrary, at the element level we have

$$M^e\ddot{\hat{\mathbf{x}}}^e + R^e(\hat{\mathbf{x}}^e) = F^e + \int_{\partial\Omega_0^e - \mathcal{S}_{20}} N^{eT}\bar{\mathbf{s}}dA. \tag{5.27}$$

After the element level equations are assembled, the resulting system is in the form

$$M\ddot{\hat{\mathbf{x}}} + R(\hat{\mathbf{x}}) = F \tag{5.28}$$

which is a system of ordinary differential equations.

Topology of Equations

The matrix M^e is dense since the element shape functions N_I^e are not typically mutually orthogonal[2]. The same is true for the function R^e, i.e. the "force" on any node depends on the nodal variables of all the other nodes within the element, as given above in (5.26) and (5.27). Therefore, in FEM formulation, the degrees of freedom are fully connected within an element.

For the assembled set of equations, the variables for the elements are connected only by the degrees of freedom shared between elements. This results in a typical banded structure for the matrix M and a similar dependence in the function R.

5.2.3 Lumped Element Model

Lumped element models are meshes of mass, spring and damper elements. Lumped masses at the nodes of the mesh are interconnected by spring and damper elements. Equations of motion are the collection of the Newton's equations written for the individual nodal masses.

For each nodal mass, the equation of motion is in the form

$$m_i \ddot{\mathbf{x}}_i \quad = \quad K_i(\mathbf{x}) + F_i \tag{5.29}$$

with F_i being the external force on the node, such as gravity, and

$$K_i(\mathbf{x}) = \sum_{\{i,j \text{ connected}\}} \mathbf{f}(\mathbf{x}_i, \mathbf{x}_j) + \sum_{\{i,j,k \text{ connected}\}} \mathbf{g}(\mathbf{x}_i, \mathbf{x}_j, \mathbf{x}_k) \tag{5.30}$$

where $f(\cdot,\cdot)$ is the force from a linear spring and the $g(\cdot,\cdot,\cdot)$ is the force from an angular spring. A typical expression used for linear springs is

$$\mathbf{f}(\mathbf{x}_1, \mathbf{x}_2) = k(\|\mathbf{x}_1 - \mathbf{x}_2\| - L_0)(\mathbf{x}_2 - \mathbf{x}_1)/(\|\mathbf{x}_1 - \mathbf{x}_2\|). \tag{5.31}$$

For the angular springs, the force expression is in the form

$$\mathbf{g}(\mathbf{x}_1, \mathbf{x}_2, \mathbf{x}_3) = k(\theta - \theta_0) \left(\frac{\mathbf{x}_1 - \mathbf{x}_2}{\|\mathbf{x}_1 - \mathbf{x}_2\|} \times \frac{\mathbf{x}_3 - \mathbf{x}_2}{\|\mathbf{x}_3 - \mathbf{x}_2\|} \right) \times \frac{\mathbf{x}_1 - \mathbf{x}_2}{\|\mathbf{x}_1 - \mathbf{x}_2\|}. \tag{5.32}$$

[2]The matrix M^e is sometimes approximated with a diagonal matrix by using nodal quadrature to decrease computational cost, but this is by no means inherent to the FE method. See the section 5.6 on computational issues for more details.

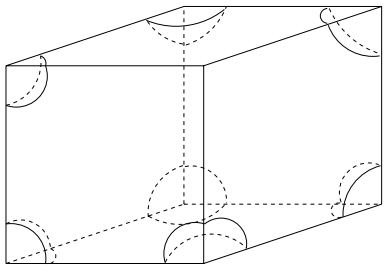

Figure 5.3: Lumped model without cross springs

These expressions are for force acting on node $\mathbf{x}_1$, due to the a spring between $\mathbf{x}_1, \mathbf{x}_2$ and an angular spring between $\mathbf{x}_1, \mathbf{x}_2, \mathbf{x}_3$. L_0 is the rest length of the linear spring and θ_0 is the rest angle of the angular spring.

The angular springs are typically used to enforce $\mathcal{C}^1$ continuity in the mesh.

Topology of Equations

Connectivity in LEM depends on the types of the springs used. The force on any node depends on the nodes it is connected to through springs. This results in a sparse system of equations, similar to the FE and FD models.

Observations

In LEM, the basis of approximation is the values of deformation at the nodes, not weights of some approximation functions. Also, the global mass matrix is inherently diagonal as it is in the FD model. Therefore it is more suitable to classify LEM as a form of finite difference approximation rather than a simplified FE model. The force term coming from the springs connecting the nodal masses can be interpreted as the discretization of the divergence operator.

The type of springs used determines the type of behavior the model exhibits. For example, if the model in Fig. 5.3, a regular grid with linear springs between neighboring nodes and angular springs between neighboring edges, is used, and the body is subjected to a uniform surface force on the top and bottom faces, the body will not expand laterally. To exhibit this behavior, it is necessary to have cross springs (on the faces and in the interior of the building block connections).

The minimum number of spring connections for the structure to be well posed is

imposed by the total degrees of freedom available within the body. The idea is that, when all the springs are replaced with rigid connectors (angular springs to maintain fixed angle) the body should be able to have only rigid modes of motion (3 DOF on the plane and 6 DOF in the space). For example: In 2D, each mass adds an extra 2 DOF. For a 4 mass model, we want $2 \times 4 - n = 3$ DOF, which gives $n = 5$ as the minimum number of constraints (connections). Therefore, a grid connection pattern does not give a well defined structure, as it cannot resist shear. As each additional node gives an extra 2 DOF, it is necessary to add at least 2 springs per mass added. For the spatial (3D) case each mass gives an additional 3 DOF to the structure, therefore it is necessary add 3 springs per added mass. Having more constraints will not cause problem as long as they are consistent.

5.3 Boundary Conditions and Contact

Consider a single deformable body placed on a rigid surface, being manipulated by a position controlled instrument, as seen in Fig. 5.4. The typical boundary conditions for this case are as follows: At the interface between the deformable body and a position controlled object (such as ground, which has fixed location, or the instrument, whose position is specified through the haptic interface), normal displacement of the nodes are specified as boundary conditions. In the tangent directions, the traction is specified as zero for no friction case or proportional to normal force when there is friction. For the parts of the body that are glued to a location or grabbed by the instrument, the displacement is specified in all directions. All other boundary conditions are given as $\bar{\mathbf{s}} = 0$ (zero traction).

Position boundary conditions can easily be prescribed in all of the modeling methods previously presented, through the nodal variables in FD and LE models, and through the positional degrees of freedom of the elements in FE models.

Enforcement of traction boundary conditions is trickier. In the FE method, the traction boundary conditions enter through the $\int_{\partial\Omega_0^e \cap \mathcal{S}_{2\,0}} N^{eT} \bar{\mathbf{s}} dA$ term of F^e. In the LEM method, the traction boundary conditions need to be somehow converted in to nodal forces. However, there is no systematic way to do this. As there is no counterpart of the approximation functions of FEM in LEM, the way F^e term is systematically calculated in (5.26) cannot be transferred to LEM. Luckily, in the application we have, the type of traction boundary conditions are simple, i.e. zero if there is no friction. So, it is possible to get away with this important deficiency of the LEM.

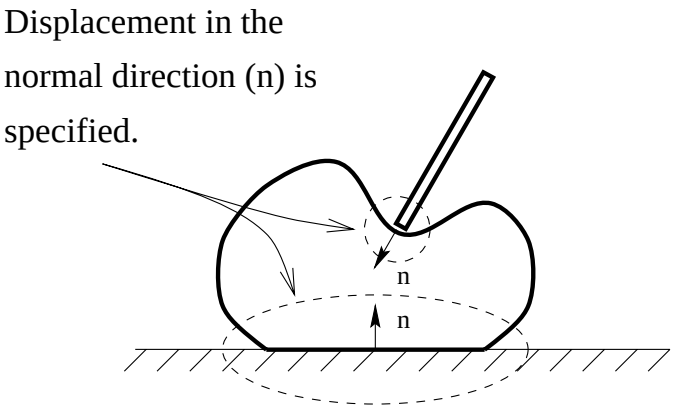

Figure 5.4: Typical boundary conditions of a deformable body being manipulated.

There are three ways to enforce the constraints for contact impenetrability when two deformable objects collide. In the penalty based method, first the interpenetration between the deformable objects are calculated. Then, a fictitious force is applied to the nodes of the two objects that have penetrated into the other one. This force is calculated based on the volume or distance of penetration, multiplied by a stiffness constant, therefore penalizing the interpenetration. This method causes numerical conditioning problems. It results in a stiff system of differential equations, which requires very small step sizes in time integration, and tends to exhibit unstable behavior rather easily. Second method is using Lagrange multipliers to enforce the impenetrability constraint. The disadvantage of this method is that it requires solution of equations, hence increasing the complexity of the system. Third method is based on motion constraining and time step dividing. In this method, after the penetrating nodes are determined, the instant of collision is interpolated by making an approximation of motion (such as linear) between the time steps. The direction of motion of the nodes in contact are constrained to be tangent to the surface to prevent penetration, and the motion is recalculated from the contact instant to the end of the time step. For surfaces already in contact, the method proceeds in the same way as it does for rigid-deformable contact. Impulse based methods of Mirtich [71] for simulation of contacting objects cannot be used here as impulse based simulation is only applicable to rigid objects.

5.4 Cutting, Tearing and Suturing

Cutting and tearing are forms of interaction with the deformable model, which result in topological change in the mesh structure. They are very closely related problems. In cutting, an instrument, such as a knife, which gives a well-defined surface of incision, divides through the mesh. Since these instruments are usually quite sharp, the incision itself is very well defined, and the fracture resulting from the incision follows the instrument. The only condition that needs to be checked is if the shear force or the pressure at the contact is larger than the strength of the tissue. Once the incision surface is known, the elements on the incision surface are divided, resulting in the topological change in the mesh. It may also be necessary to remesh around the incision surface to avoid numerical conditioning problems.

Tearing is an interesting problem by itself, e.g. in cornea simulation. In tearing, contrary to cutting, there is not a well defined incision surface generated by an instrument. Rather, the incision is the result of the formation and advance of fracture in the tissue. For the applications where tearing is important, one needs to accurately model fracture formation and advance, which is a complicated and highly nonlinear problem.

Suturing can easily be modeled by adding nodes to the mesh along the trajectory of the needle. This results in topological changes in the mesh structure, as well as some additional boundary conditions. The interaction between the thread and the tissue can be modeled through these new boundary conditions on the added nodes. These nodes can only move along the direction of the thread, and the deformation of the thread is specified by the forces on these nodes, which are the interaction force between the thread and the tissue. It is also necessary to model the dynamics of the thread.

5.5 Determination of Parameters

In FE models, the parameters of the elements are determined from the constitutive properties of the material of the object being simulated. For the LE models, there is no intrinsic method to determine the element parameters since the models are not actually motivated from approximating the physical behavior of the object.

As mentioned in the discussion above, one of the main problems of LEM is the lack of a systematic way to determine element parameters. In the literature, the parameters

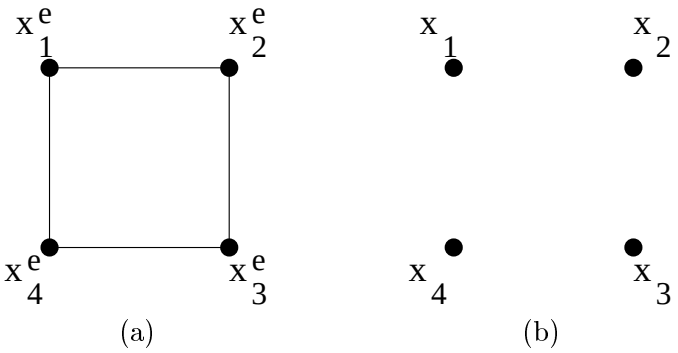

Figure 5.5: 4 node FEM (a) and LEM (b) elements.

of the LEM models are determined through parameter estimation, to fit the response of the model to an experimentally measured response. If the structure allows, it may be possible to isolate effects of some parameters or do some approximations to isolate these parameters and therefore simplify parameter estimation [30]. Otherwise, this can be a very complex optimization problem depending on the number of parameters used.

Here, we will establish a parallelism between the elements in FEM and LEM, and explore methods for setting up of the LEM mesh and selection of its parameters as a way to approximate FEM.

In the discussion below, without loss of generality, we will look at the 2 dimensional case (plane strain[3]) in the absence of external forces, in order to simplify the notation and equations.

Consider a planar 4 node $\mathcal{C}^0$ continuous isoparametric element for the FEM, and a 4 mass configuration for the LEM (Fig. 5.5). The masses of the LEM mesh are located at the same spatial locations as the nodes of the FEM element. This configuration of the LEM masses, with the interconnection springs and dampers, will be used as the building block elements of the LEM mesh. At this point, we are not yet specifying the spring connections between the nodes.

The equations of motion for the FEM and LEM elements are respectively

$$M^e \ddot{\hat{\mathbf{x}}}^e + R^e(\hat{\mathbf{x}}^e) = 0, \qquad \begin{bmatrix} m_1 & & 0 \\ & \ddots & \\ 0 & & m_4 \end{bmatrix} \ddot{\hat{\mathbf{x}}} = K(\hat{\mathbf{x}}) \ . \tag{5.33}$$

[3]Plane strain analysis is used to solve deformation in infinitely long structures which are uniform in the third dimension.

The matrix M^e is dense, but if we use nodal quadrature, it is possible to get a diagonal approximation for the M^e in FEM. For the LEM, we can choose $m_i = m^e_{ii}$, therefore getting a physically based value for the nodal mass. Then, if we can approximate $R^e(\hat{\mathbf{x}}^e)$ with $-K(\hat{\mathbf{x}})$, we can use the LEM for approximating FEM, avoiding the parameter determination problem. If we look at the structure of the function $R^e(\mathbf{x}^e)$

$$R^e(\hat{\mathbf{x}}^e) = \begin{bmatrix} R^e_1(\mathbf{x}^e_1, \mathbf{x}^e_2, \mathbf{x}^e_3, \mathbf{x}^e_4) \\ R^e_2(\mathbf{x}^e_1, \mathbf{x}^e_2, \mathbf{x}^e_3, \mathbf{x}^e_4) \\ R^e_3(\mathbf{x}^e_1, \mathbf{x}^e_2, \mathbf{x}^e_3, \mathbf{x}^e_4) \\ R^e_4(\mathbf{x}^e_1, \mathbf{x}^e_2, \mathbf{x}^e_3, \mathbf{x}^e_4) \end{bmatrix}. \tag{5.34}$$

Comparing with the LEM equations

$$R^e_i(\hat{\mathbf{x}}^e) = \int_{\Omega^e_0} B^{eT}_i S(\hat{\mathbf{x}}^e) dV, \qquad -K_i(\hat{\mathbf{x}}) = -\sum_{i,j \text{ connected}} \mathbf{f}(\mathbf{x}_i, \mathbf{x}_j) \tag{5.35}$$

we observe that the nonlinear functions $R^e_i(\hat{\mathbf{x}}^e)$ needs to be approximated by the function $-K_i(\hat{\mathbf{x}})$, which is the sum of the spring forces on node i. Nonlinear case is too complicated to make basic observations, so we are going to proceed with the simpler case, linear FEM and linearized form of LEM.

For the LEM element, we need to linearize expression for the spring forces

$$\mathbf{f}_i = \begin{bmatrix} \frac{\partial \mathbf{f}(\mathbf{x}_i, \mathbf{x}_j)}{\partial \mathbf{x}_i} & \frac{\partial \mathbf{f}(\mathbf{x}_i, \mathbf{x}_j)}{\partial \mathbf{x}_j} \end{bmatrix} \begin{bmatrix} \mathbf{u}_i \\ \mathbf{u}_j \end{bmatrix} \tag{5.36}$$

$\hat{\mathbf{u}}^e = \hat{\mathbf{x}}^e - \hat{\mathbf{x}}^e(0)$ is the displacement.

$$\frac{\partial \mathbf{f}(\mathbf{x}_i, \mathbf{x}_j)}{\partial \mathbf{x}_i} = -\frac{\partial \mathbf{f}(\mathbf{x}_i, \mathbf{x}_j)}{\partial \mathbf{x}_j} = -\begin{bmatrix} A^{\mathbf{u}_1, \mathbf{u}_2}_1 & B^{\mathbf{u}_1, \mathbf{u}_2}_{1,2} \\ B^{\mathbf{u}_1, \mathbf{u}_2}_{2,1} & A^{\mathbf{u}_1, \mathbf{u}_2}_2 \end{bmatrix} \tag{5.37}$$

$$A^{\mathbf{u}_1, \mathbf{u}_2}_i = k^{1,2} \left(1 - \frac{L_0}{\|\mathbf{x}_2 - \mathbf{x}_1\|} \frac{\|\mathbf{x}_2 - \mathbf{x}_1\|^2 - (\mathbf{x}_{2i} - \mathbf{x}_{1i})^2}{\|\mathbf{x}_2 - \mathbf{x}_1\|^2} \right) \tag{5.38}$$

$$B^{\mathbf{u}_1, \mathbf{u}_2}_{i,j} = k^{1,2} \left(\frac{L_0}{\|\mathbf{x}_2 - \mathbf{x}_1\|} \frac{(\mathbf{x}_{2i} - \mathbf{x}_{1i})(\mathbf{x}_{2j} - \mathbf{x}_{1j})}{\|\mathbf{x}_2 - \mathbf{x}_1\|^2} \right) \tag{5.39}$$

We will define

$$K^{i,j} = \begin{bmatrix} A^{\mathbf{u}_i, \mathbf{u}_j}_1 & B^{\mathbf{u}_i, \mathbf{u}_j}_{1,2} \\ B^{\mathbf{u}_i, \mathbf{u}_j}_{2,1} & A^{\mathbf{u}_i, \mathbf{u}_j}_2 \end{bmatrix} \tag{5.40}$$

to simplify the notation. Note that $K^{i,j} = K^{j,i}$. Then, the linearized equations for LEM is

$$K(\hat{\mathbf{x}}) \approx K\hat{\mathbf{u}} \tag{5.41}$$

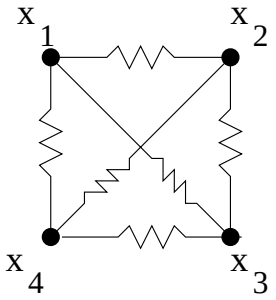

Figure 5.6: A fully connected 4 node LEM element.

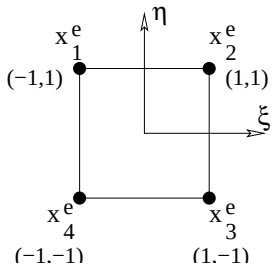

Figure 5.7: 4 node master FEM element.

and the K matrix has entries for each of the springs. For example, if we consider the LEM element of Fig. 5.6 we get

$$K\hat{\mathbf{u}} = \begin{bmatrix} -K^{1,2} - K^{1,3} - K^{1,4} & K^{1,2} & K^{1,3} & K^{1,4} \\ K^{2,1} & -K^{2,1} - K^{2,3} - K^{2,4} & K^{2,3} & K^{2,4} \\ K^{3,1} & K^{3,2} & -K^{3,1} - K^{3,2} - K^{3,4} & K^{3,4} \\ K^{4,1} & K^{4,2} & K^{4,3} & -K^{4,1} - K^{4,2} - K^{4,3} \end{bmatrix}. \tag{5.42}$$

For the FEM element

$$R^e(\hat{\mathbf{x}}^e) \approx R^e\hat{\mathbf{u}}, \tag{5.43}$$

$$R^e = \int_{\Omega_0^e} B^{eT} D B^e dV. \tag{5.44}$$

D is the matrix which transforms strain vector to stress vector ($\sigma = D\epsilon$). For brevity, we are using the same symbol for the nonlinear function and matrix for the linear case, since they are distinguishable from the context.

At this point, to simplify the calculations, we will further assume that the element

in the reference configuration is the same as the master element $\hat{\Omega}$ (Fig. 5.7) and the deformable object is a homogeneous linear isotropic material. Then,

$$R^e = \int_{\Omega_0^e} B^{eT} D B^e dx dy \tag{5.45}$$

$$= \int_{\hat{\Omega}} B^{eT} D B^e J d\xi d\eta \tag{5.46}$$

$$= \int_{-1}^{1}\int_{-1}^{1} B^{eT} D B^e d\xi d\eta \tag{5.47}$$

$$R^e_{ij} = \int_{-1}^{1}\int_{-1}^{1} B_i^{eT} D B_j^e d\xi d\eta. \tag{5.48}$$

For the isoparametric element

$$N_1 = \frac{(1-\xi)(1+\eta)}{4} \tag{5.49}$$

$$N_2 = \frac{(1+\xi)(1+\eta)}{4} \tag{5.50}$$

$$N_3 = \frac{(1+\xi)(1-\eta)}{4} \tag{5.51}$$

$$N_4 = \frac{(1-\xi)(1-\eta)}{4} \tag{5.52}$$

$$\tag{5.53}$$

and for isotropic plane strain

$$D = \begin{bmatrix} \lambda+2\mu & \lambda & 0 \\ \lambda & \lambda+2\mu & 0 \\ 0 & 0 & \mu \end{bmatrix}. \tag{5.54}$$

λ and μ are the Lame constants of the material. If we evaluate the integral, we get

$$R^e = \begin{bmatrix} \frac{\lambda}{3}+\mu & \frac{-\lambda-\mu}{4} & \frac{-\lambda}{3}-\frac{\mu}{2} & \frac{-\lambda}{4}+\frac{\mu}{4} & \frac{-\lambda}{6}-\frac{\mu}{2} & \frac{\lambda}{4}+\frac{\mu}{4} & \frac{\lambda}{6} & \frac{\lambda-\mu}{4} \\ \frac{-\lambda-\mu}{4} & \frac{\lambda}{3}+\mu & \frac{\lambda}{4}-\frac{\mu}{4} & \frac{\lambda}{6} & \frac{\lambda}{4}+\frac{\mu}{4} & \frac{-\lambda}{6}-\frac{\mu}{2} & \frac{-\lambda+\mu}{4} & \frac{-\lambda}{3}-\frac{\mu}{2} \\ \frac{-\lambda}{3}-\frac{\mu}{2} & \frac{\lambda}{4}-\frac{\mu}{4} & \frac{\lambda}{3}+\mu & \frac{\lambda}{4}+\frac{\mu}{4} & \frac{\lambda}{6} & \frac{-\lambda}{4}+\frac{\mu}{4} & \frac{-\lambda}{6}-\frac{\mu}{2} & \frac{-\lambda}{4}-\frac{\mu}{4} \\ \frac{-\lambda}{4}+\frac{\mu}{4} & \frac{\lambda}{6} & \frac{\lambda}{4}+\frac{\mu}{4} & \frac{\lambda}{3}+\mu & \frac{\lambda}{4}-\frac{\mu}{4} & \frac{-\lambda}{3}-\frac{\mu}{2} & \frac{-\lambda}{4}-\frac{\mu}{4} & \frac{-\lambda}{6}-\frac{\mu}{2} \\ \frac{-\lambda}{6}-\frac{\mu}{2} & \frac{\lambda}{4}+\frac{\mu}{4} & \frac{\lambda}{6} & \frac{\lambda}{4}-\frac{\mu}{4} & \frac{\lambda}{3}+\mu & \frac{-\lambda}{4}-\frac{\mu}{4} & \frac{-\lambda}{3}-\frac{\mu}{2} & \frac{-\lambda}{4}+\frac{\mu}{4} \\ \frac{\lambda}{4}+\frac{\mu}{4} & \frac{-\lambda}{6}-\frac{\mu}{2} & \frac{-\lambda}{4}+\frac{\mu}{4} & \frac{-\lambda}{3}-\frac{\mu}{2} & \frac{-\lambda}{4}-\frac{\mu}{4} & \frac{\lambda}{3}+\mu & \frac{\lambda}{4}-\frac{\mu}{4} & \frac{\lambda}{6} \\ \frac{\lambda}{6} & \frac{-\lambda+\mu}{4} & \frac{-\lambda}{6}-\frac{\mu}{2} & \frac{-\lambda}{4}-\frac{\mu}{4} & \frac{-\lambda}{3}-\frac{\mu}{2} & \frac{\lambda}{4}-\frac{\mu}{4} & \frac{\lambda}{3}+\mu & \frac{\lambda+\mu}{4} \\ \frac{\lambda-\mu}{4} & \frac{-\lambda}{3}-\frac{\mu}{2} & \frac{-\lambda}{4}-\frac{\mu}{4} & \frac{-\lambda}{6}-\frac{\mu}{2} & \frac{-\lambda}{4}+\frac{\mu}{4} & \frac{\lambda}{6} & \frac{\lambda+\mu}{4} & \frac{\lambda}{3}+\mu \end{bmatrix} \tag{5.55}$$

We can make one observation here, on how to determine the required connectivity of the LEM elements. The matrix R^e does not have a zero block. This is because the DOF

in this FEM element are all coupled. Therefore, for the LEM element to be able to have the same behavior as the FEM element, it needs to be fully connected, as shown in Fig. 5.6.

Since the material is assumed to be isotropic, the LEM element has to be symmetric

$$k^{\text{edge}} = k^{1,2} = k^{2,3} = k^{3,4} = k^{4,1} \tag{5.56}$$

$$k^{\text{diag}} = k^{1,3} = k^{2,4} \tag{5.57}$$

K has two independent parameters, $k^{\text{edge}}, k^{\text{diag}}$. So does R^e, λ, μ. Then, at first we may think that it should be possible to construct a LEM element which has the same input-output behavior as the FEM element. However, it is not too difficult to see that this is not true, if we look at the individual terms of the matrices K and R^e. Each subblock R^e_{ij} depends on both of the parameters (λ, μ), but this is not the case for K_{ij}, which depends only on single parameter $(k^{i,j})$. Therefore, in block by block sense, LEM element cannot represent the Poisson ratio and bulk modulus simultaneously. It is also informative to note that there are some structural differences between these blocks as well, which can be observed from (5.55). K_{ij} is always symmetric (see (5.40)), but same is not true for R^e_{ij}, whose corresponding off-diagonal terms may or may not have the same sign. Also, the diagonal terms of K_{ij} are always positive, but the the diagonal terms of R^e_{ij} may be positive or negative.

The difference between the behavior of the FEM and LEM elements comes from the fact that the interaction between the nodes are restricted to be some form of spring-like behavior in LEM, whereas there is freedom in FEM. This restricts the physical material behaviors that LEM models can represent.

It is also possible to consider adding angular springs within the LEM element. This would enrich the behavior of the LEM element. However, addition of angular springs would decrease the computational attractiveness of the LEM because of the increased computational complexity. We will leave this for future work.

To approximate FEM element behavior with an LEM element, at least for the linear case, we need to perform the following optimization

$$(k^{\text{edge}}, k^{\text{diag}}) = \arg \inf_{k^{\text{edge}}, k^{\text{diag}}} \left\| R^e(\lambda, \mu) + K(k^{\text{edge}}, k^{\text{diag}}) \right\| \tag{5.58}$$

in some norm. The most natural choice would be the induced 2-norm, which looks at the input-output behavior of the two matrices.

If we use the Frobenius norm, the blocks will be decoupled, and we can get a simple closed form solution

$$R^e_{1,2} = \begin{bmatrix} -\frac{\lambda}{3} - \frac{\mu}{2} & -\frac{\lambda}{4} + \frac{\mu}{4} \\ \frac{\lambda}{4} - \frac{\mu}{4} & \frac{\lambda}{6} \end{bmatrix} \quad -K_{1,2} = \begin{bmatrix} -k^{\text{edge}} & 0 \\ 0 & 0 \end{bmatrix} \tag{5.59}$$

gives

$$k^{\text{edge}} = \frac{\lambda}{3} + \frac{\mu}{2} \tag{5.60}$$

and

$$R^e_{1,3} = \begin{bmatrix} -\frac{\lambda}{6} - \frac{\mu}{2} & \frac{\lambda}{4} + \frac{\mu}{4} \\ \frac{\lambda}{4} + \frac{\mu}{4} & -\frac{\lambda}{6} - \frac{\mu}{2} \end{bmatrix} \quad -K_{1,3} = \begin{bmatrix} -k^{\text{diag}} & k^{\text{diag}} \\ k^{\text{diag}} & -k^{\text{diag}} \end{bmatrix} \tag{5.61}$$

gives

$$k^{\text{diag}} = \frac{\left(\frac{\lambda}{6} + \frac{\mu}{2}\right) + \left(\frac{\lambda}{4} + \frac{\mu}{4}\right)}{2} = \frac{5\lambda}{12} + \frac{3\mu}{4} \tag{5.62}$$

for the element configurations we assumed.

This optimization to determine LEM parameters need to be performed for every different element configuration, since the linearization depend on the geometry of the elements.

5.6 Comparison of Computational Complexity

Explicit integration is typically the choice for dynamical simulation in real time applications as it is not necessary to solve any nonlinear equations. The amount of computation required to advance one time step is the main concern for real-time applications as this is what limits the possible update rate. Therefore, it is preferred to perform as much off-line calculation as possible, as long as they have realistic storage requirements. It is also important to consider the how the minimum time step required to maintain stability changes.

Actually, up to this point, we have not really mentioned viscoelastic behavior. Viscoelasticity is modeled by the addition of dampers in the mesh for LEM, and in FEM viscoelastic terms in the constitutive relation result in R matrix being a function of $\mathbf{v}$ as well as $\mathbf{x}$.

5.6.1 Computational Requirements for Nonlinear FE Model

In FEM, the calculations are performed at the element level. The integrals over the elements are numerically calculated with Gaussian quadrature.

If we look at the individual terms:

- Mass matrix

$$M^e = \int_{\Omega_0^e} N^{eT} \rho_0 N^e dV \tag{5.63}$$

is constant, i.e. independent of deformation. It is a (3 NEN) $\times$ (3 NEN) matrix for each element. The mass matrix is typically approximated with a diagonal matrix, calculated using nodal quadrature. This is to avoid inverting the mass matrix, and storing the inverted mass matrix, which is dense.

- External force vector

$$F^e = \underbrace{\int_{\Omega_0^e} N^{eT} \overbrace{\mathbf{b}_0}^{\text{gravity}} dV}_{\text{const.}} + \underbrace{\int_{\partial\Omega_0^e \cap \mathcal{S}_{2\,0}} N^{eT} \underbrace{\bar{\mathbf{s}}}_{\text{varies}} dA}_{\text{varies}} \tag{5.64}$$

Constant part of the force vector is a (3 NEN) $\times$ 1 vector for each element. The varying part of the force vector is evaluated only at the surface elements/faces, where there is a nonzero traction boundary condition.

- The stress divergence term

$$R^e(\hat{\mathbf{x}}) = \int_{\Omega_0^e} B^{eT} S(N^e \hat{\mathbf{x}}^e) dV \tag{5.65}$$

$$\begin{matrix}\text{(Mapped to the} \\ \text{master element)}\end{matrix} = \int\int\int_{-1}^{1} B^{eT} S(N^e \hat{\mathbf{x}}^e) J_o d\xi d\eta d\zeta \tag{5.66}$$

$$\text{(Gaussian quadrature)} = \sum_i \sum_j \sum_k w_{ijk} \left[B^{eT} S(N^e(\xi,\eta,\zeta)\hat{\mathbf{x}}^e) J_o \right]_{ijk} \tag{5.67}$$

which is calculated at the quadrature points is the only major term that needs to be calculated for each element.

The matrix functions N^e, B^e and J_o are same for same type of elements and can be pre-constructed. For the individual elements, they are evaluated at the Gaussian quadrature points. Values of N^e evaluated are fixed for the same type of elements, independent of

the reference and current configurations, and can be precalculated for existing types of elements. Values of B^e and J_o depend on the reference configuration but not the current configuration (independent of deformation) therefore can be precalculated and stored for individual elements.

5.6.2 Computational Requirements for LE Model

The governing equation for the LE model is in the form

$$\ddot{\mathbf{x}} = \frac{1}{m_i}(\sum \mathbf{f} + \sum \mathbf{g}). \tag{5.68}$$

The main computation is from the calculation of the $\mathbf{f}(\cdot,\cdot)$ and $\mathbf{g}(\cdot,\cdot,\cdot)$ terms for each nodal mass.

5.6.3 Computational Requirements for Linear FE Model

The form of the equation is in the form

$$M\ddot{\mathbf{x}} + K\mathbf{x} = F \tag{5.69}$$

The main motivation behind using linear FE models is the ability to perform off-line computations. The following are the potential off-line computations that can be performed:

- M^{-1} can be precalculated and stored. This part is not is very critical, as it is possible to use nodal quadrature to have a diagonal approximation for M.
- Quasi-static approximation, ignoring the inertial behavior: $\mathbf{x} = K^{-1}F$. K^{-1} can be calculated off-line and stored. This has a large storage requirement as K^{-1} is dense, but it is possible to store how to calculate the LU decomposition rather than the factorized form, therefore reducing the storage requirement while lowering the online computational requirements. Bro-Neilsen [12, 13] proposed to use bordering method to further simplify the computation: Since there is external force only on the surface elements (assuming no gravity), we can write the quasi static linear elasticity equations as $\begin{bmatrix} K_{11} & K_{12} \\ K_{21} & K_{22} \end{bmatrix} \begin{bmatrix} \mathbf{x}_{ext} \\ \mathbf{x}_{int} \end{bmatrix} = \begin{bmatrix} F_{ext} \\ 0 \end{bmatrix}$. Then it is possible to eliminate $\mathbf{x}_{int}$ and get $\mathbf{x}_{ext} = (K_{11} - K_{12}K_{22}^{-1}K_{21})^{-1}F$ with significantly smaller storage requirements.

5.7 Conclusion and Discussion

In this chapter, we looked at the dynamical simulation of deformable objects for real time simulation in VEs. Emphasis was on the formulation of the physical problem, basic enabling technologies, and comparison of modeling techniques used in the literature. Our observations about the FE, FD, and LE models are summarized in the table 5.1.

Approximation Type	Lumped Element Models	Finite Element Models	Finite Difference Models
Mass Distribution	Lumped	Distributed	Lumped
Discretization	Nodal variables (position and velocity)	Weights of the approximation functions	Nodal variables
Parameters	Parameters of the lumped elements	Constitutive relation	Constitutive relation
Connectivity	Based on the types of components used. Neighbors and 3-4 node torsional elements.	Based on the number of nodes of the elements. Fully connected within each element.	Based on the discretization used for the differential operator.
Determination of Parameters	Fit response to experimental data through a search in parameter space, OR, approximate FEM	Can use material characteristics given in terms of the constitutive model.	Can use material characteristics given in terms of the constitutive model.
Boundary Conditions	Need to convert boundary conditions into conditions on the nodal variables.	Inherent in the formulation.	Inherent in the formulation
Non-Uniform Mesh	Yes	Yes	No

Table 5.1: Comparison of the lumped element, finite element and finite difference models of deformable objects.

Chapter 6

Haptic Interfacing to Virtual Environments

Haptic interaction is an increasingly common form of interaction in virtual environment (VE) simulations, especially since the commercial availability of high fidelity haptic devices such as the Phantom (Sensable Technologies Inc., Cambridge, MA) and Impulse Engine (Immersion Corp., San Jose,CA). This relatively new medium introduces some new challenges, which are being studied in the literature. Ensuring stability of haptic interaction with the virtual environment is an important problem. Several researchers have considered the effects of model sampling time on stability [70, 22]. Colgate *et.al.* point out the non-passive nature of the discrete implementations of virtual environments as a major source of instability [22], and propose a virtual coupling network to improve stability [23]. Adams and Hannaford give a design algorithm to ensure stability of the haptic interface coupled to arbitrary passive virtual environments, therefore separating the design of the virtual environment and the haptic interface [1]. Simulation of stiff walls and hard contact is another interesting research topic. The penalty based approach is the most common way to simulate stiff walls. Zilles and Salisbury propose using "god-objects" to eliminate problems with penetration into the virtual objects in a penalty based approach [112], and Salcudean and Vlaar report that using a braking pulse greatly improves the perception of a stiff wall [82].

In a VE simulation of interaction with deformable bodies, for example in a surgical simulator, typically the physical model is updated at the visual update rates of 10 Hz order

of magnitude. But haptic interfaces require much higher update rates, typically in the order of 1 kHz. It is not possible to increase the update rate of the physical model to the haptic rate with its full complexity due to computational limitations. The current practice is to apply the same force between the model updates, or to low-pass filter this generated force to the bandwidth of the model update rate. These effectively reduce the haptic update rate to the visual update rate, and therefore impair the fidelity of the haptic interaction. This is especially significant when the high frequency interaction forces are significant, for example in nonlinear phenomena like contact.

Astley and Hayward propose to use a multiscale multirate finite element model to address this problem. In their method, a coarse linear finite element mesh models the behavior of the overall object and a finer finite element mesh running at a higher update rate is used locally where there is an interaction [6]. Their work is based on decoupling the coarse mesh and the fine mesh by using the Norton equivalents as interfaces. This is only applicable to the linear finite element case, and the update rates reported were still significantly below 1 kHz required by the haptics.

In this chapter we propose a multirate simulation approach to handle the difference between the update rate requirements for the haptics and the physical model during haptic interaction in VE simulations, complete with theoretical and experimental verifications of the approach. The proposed method is justified by model reduction techniques from system theory, and the approach is applied to nonlinear physical models.

We will start our treatment with a demonstration of the problem. This will be followed by the description of the proposed method, analysis of the critical parts, implementation, a short discussion of stability implications, and concluding remarks.

The discussion here is limited to lumped element models (also referred to as mass-spring-damper models in the literature), but the arguments can easily be extended to deformable models based on finite element analysis.

6.1 Demonstration of the Problem

We first consider a haptic interface interacting with a simulated nonlinear spring in one dimension, and evaluate the fidelity of the force output of different simulation schemes for a given stimulus. This simple analysis demonstrates the problems that arise from the low model update rate and illustrates the basic motivation of the method proposed in this

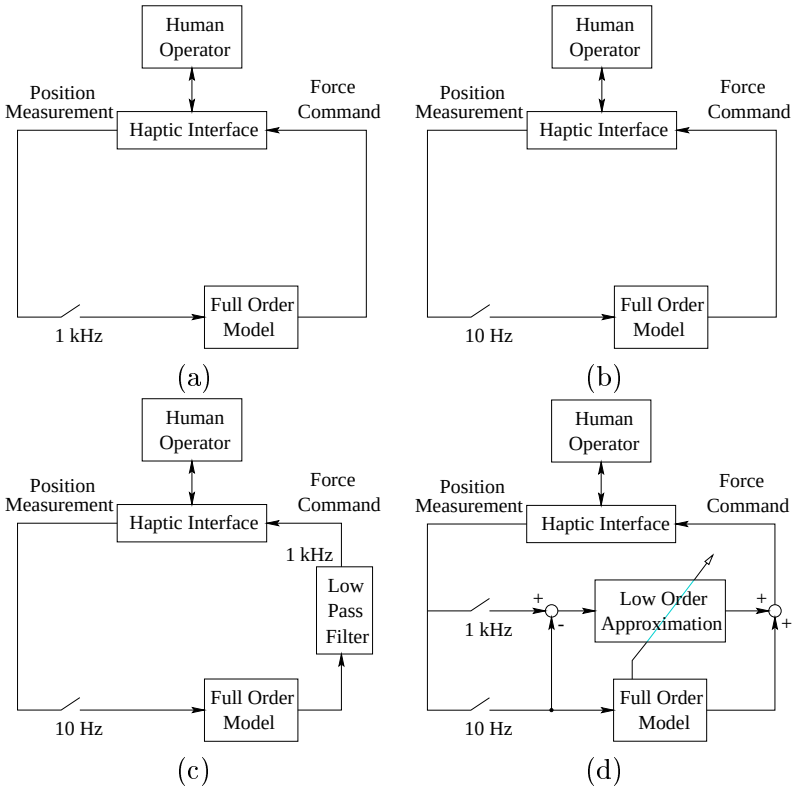

Figure 6.1: Simulation paradigms.

paper.

Four different simulation models, with 1kHz haptic update rates, are considered. In the first model, force feedback is generated by the nonlinear spring model updated at 1 kHz, which corresponds to the case where the model update rate is the same as haptic update rate. It is the baseline for the analysis as it is the ideal case. In the second model, the force is generated from the nonlinear spring model at an update rate of 10 Hz, and maintained constant in between the model updates. This is the counterpart of the case where there is interaction with a deformable model simulated at a larger step size than the haptic sampling time. The third simulation model is an improved version of the second one. In this case, the nonlinear spring model is updated at 10 Hz, but the applied force is a low pass filtered version of the piecewise constant force generated from the nonlinear model. The bandwidth of the low pass filter is 10 Hz, and it is running at the haptic update rate of 1 kHz. In the last model, the nonlinear model is again updated at 10 Hz, as in the second and third models. However, the force output in between the nonlinear model updates is

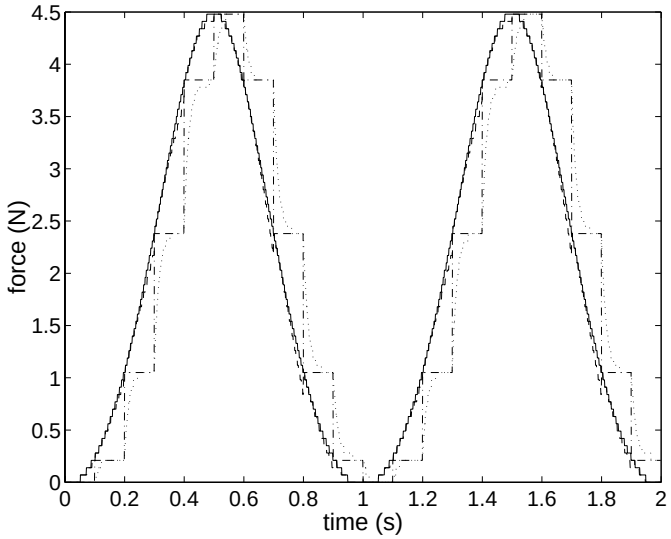

Figure 6.2: Interaction with a nonlinear spring in one dimension. Solid line is the 1kHz model, dash-dot line is the 10 Hz model, dotted line is the filtered 10 Hz model, and dashed line is the local tangent model.

calculated from a linear spring model based on the tangent of the nonlinear spring at the last model update. To summarize

$$force_1[n] = f(x[n]) \tag{6.1}$$

$$force_2[n] = f(x[N]) \tag{6.2}$$

$$force_3[n] = f(x[N]) * lpf[n] \tag{6.3}$$

$$force_4[n] = f(x[N]) + f'(x[N])(x[n] - x[N]) \tag{6.4}$$

where n and N are respectively the haptic and model samples and $lpf[n]$ is the impulse response of the 10 Hz low-pass filter. Note that n runs at 1 kHz, and N runs at 10 Hz.

The nonlinear force-position characteristic of the spring used is based on the experimentally determined force deformation characteristics of the skin of the thigh given in [30]:

$$f(x) = \frac{x}{5.4398 - 0.1418x} \tag{6.5}$$

In the simulations, quantization noise is added to the position measurements and the force output. The quantization step size used is 0.3 mm for position measurements and 0.07 Newtons for force output. These values are the typical quantization values for the Phantom(TM) version 1.5 haptic interface [83].

In the test simulations of Fig. 6.2, the haptic interface is following a sinusoidal path maintaining contact with the spring, and the interaction force generated by the simulation model versus time is shown in the plot.

If we look at the signal-to-noise ratios (SNR) for the different simulation models, we can see the difference more clearly. The SNR for the ideal case is 89 dB with lag less than 1 ms. The constant force output model has SNR of 43 dB and a lag of 49 ms, and its low pass filtered version has SNR of 53 dB and a lag of 65 ms. The local tangent model has 72 dB SNR and a lag less than 1 ms, which is significantly better performance than the other two approximate models.

The use of a low-pass filter to improve the performance of the constant output method seems to help by reducing contaminating noise at the harmonics of the model update rate. However, this approach has two main limitations. First, low pass filtering may eliminate useful high frequency force information as well, for example in the case of nonlinear stiffness. To avoid this, model update rate has to be higher than the bandwidth of voluntary hand movements, 5–10 Hz, times the harmonics generated by interaction with nonlinear stiffness. Second problem is in the case of contact, where there is significant amount of information in high frequency. Also, the lag introduced by the low pass filter tends to destabilize the haptic interaction, or introduce oscillations.

The performance of the local tangent model gives the motivation of the method proposed in this study for coping with the problems with the difference between the deformable model and haptic update rates.

6.2 Using a Low Order Linear Approximation to Model Intersample Behavior

When the instrument interacts with the deformable model in a VE simulator, the haptic interface will displace the node(s) it is touching and display the reaction force[1]. Therefore, from the haptic interfaces point of view, it will be interacting with a three-input three-output nonlinear dynamical system, considering the three components of translation as input and an three components of force as output. However, the underlying dynamical

[1]Here, we are not using a penalty based approach to model the contact forces. Rather, the instrument displaces the node it is in contact with and the interaction force is given by the internal deformation forces on the contact nodes.

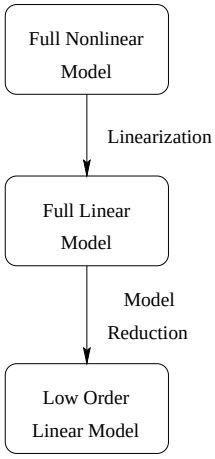

Figure 6.3: Construction of the low order model.

system has a very high order as it includes the deformation of the whole body. For example, when interacting with a $10 \times 10 \times 10$ deformable cube, a mid-sized deformable model, the deformation will have $1000 \times 3 \times 2 = 6000$th order dynamics. This very high order dynamical system, which cannot be simulated in real time, needs to be replaced with a low order approximation for real time haptic performance.

The method we are proposing follows the local tangent approach described in section 6.1, shown in Fig. 6.1(d). In this approach, a low order approximation, running at the haptic update rate, is used on top of the full order model to estimate the intersample behavior. The low order approximation is updated by the full model after each step.

To analyze the construction of the low order approximation, we start with the paradigm given in Fig. 6.3. Linearization is a basic step. The linearized model gives the tangential behavior of the full model. As we want to capture the behavior in between the model updates, the deformation will be small. As illustrated in section 6.1, use of local tangent instead of constant force output improves the response significantly.

The linearized system will have the same order as the full model, therefore the improvement is limited by just using a linear model, i.e. it will still be difficult if not impossible to simulate in real time. Therefore, model reduction is the critical step of the approach, as it is the means of getting a temporally local haptic model which can be simulated in real time.

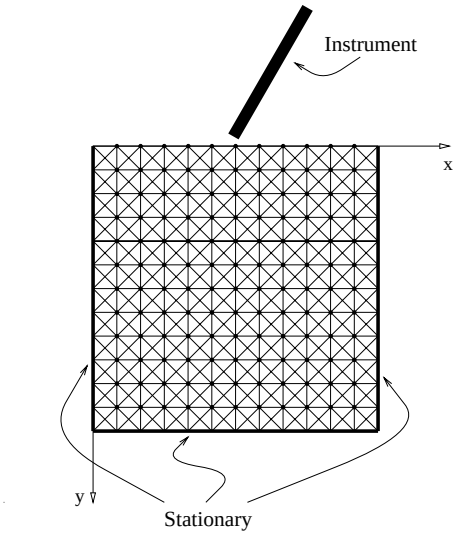

Figure 6.4: Two dimensional lumped element mesh.

6.3 Order Reduction

To evaluate the effectiveness of model reduction, consider a two dimensional 12×12 lumped element mesh being indented by an instrument (Fig. 6.4). Each node of the mesh has a lumped mass, which is connected to the neighboring nodes (diagonal as well as lateral neighbors) with spring and dampers. Three edges of the mesh are constrained to be stationary. Linearization of this system gives a two-input two-output 524th order linear dynamical system.

When we perform a balanced model reduction [110] on this model, we can approximate the system's input-output response with a 10th order system, with the infinity norm of the error resulting from the approximation being less than 1.6×10^{-3}, less than 1% of the full order model. This is a significant reduction in computational complexity while virtually maintaining the accuracy of the model. The frequency responses of the original and reduced order systems are shown in Fig. 6.5. The responses of the two systems are essentially indistinguishable except in normal-tangential interactions, where the response magnitudes in both conditions are very small (less than -200 dB).

The original states of the system before order reduction are the positions and velocities of the lumped masses at the vertices of the mesh. To visualize the spatial properties of the reduced model, the states of the new model are shown in Fig. 6.6. The figure shows

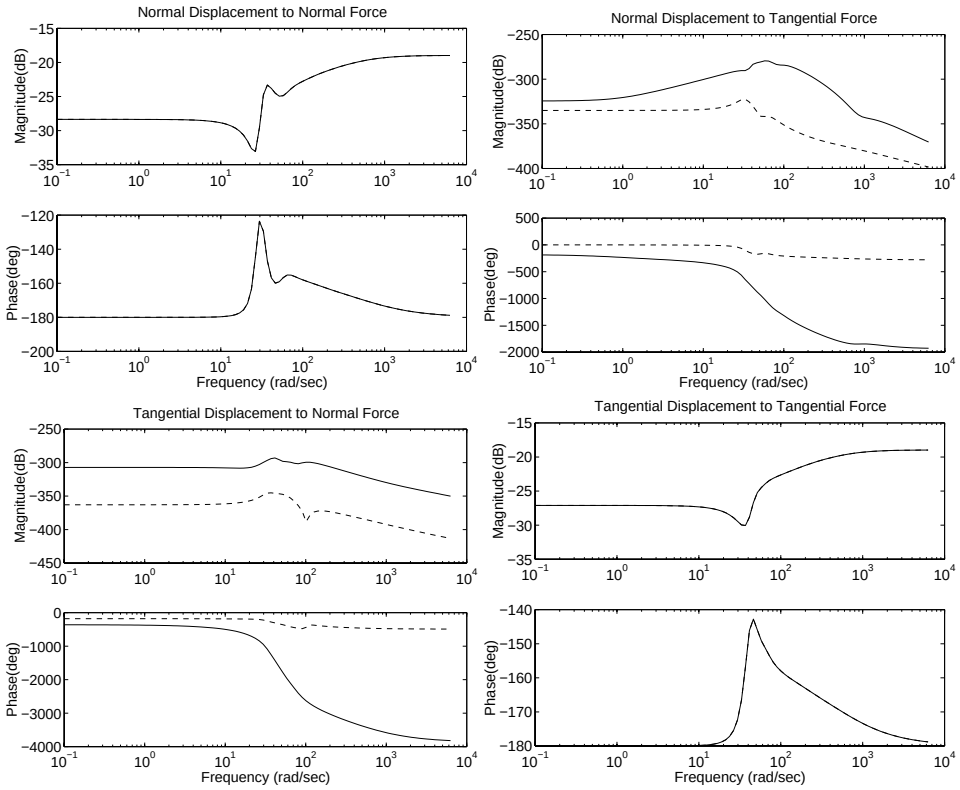

Figure 6.5: Frequency responses of the original and reduced order systems. Solid line is the reduced order model, dashed line is the full order model.

the magnitude of the components of the new states with respect to the location on the mesh. The input node is at coordinate $(50, 0)$, which is the top middle node.

The states of the new low order model show that it is a local approximation. This result is actually expected, because stress decays inversely proportional to the square of the distance from the load in a semi-infinite linear elastic body under a point load [99].

6.4 Towards a Real-Time Algorithm

It is important to note that balanced model reduction requires costly calculations as well, which prevents the use of this algorithm as a part of the on-line computation. However, the analysis in the previous section reveals that the approximation given by the balanced model reduction algorithm in a homogeneous medium is a local model, i.e. the force response depends mostly on the states spatially close to the interaction location. So, a natural way to construct a low order approximation with significantly less computation

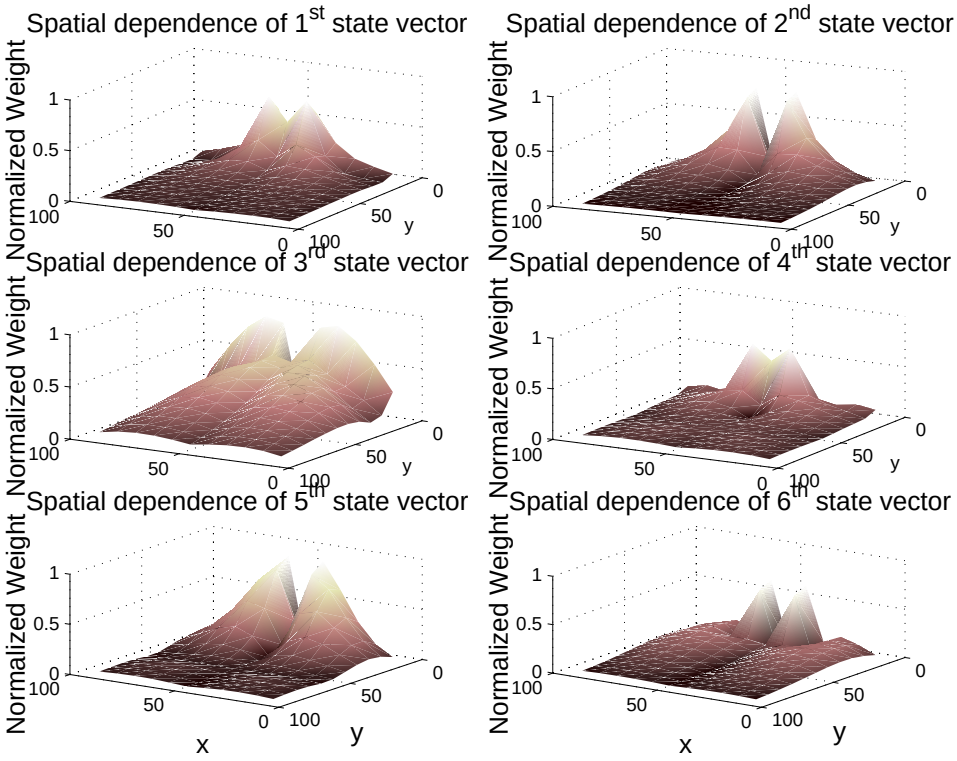

Figure 6.6: Spatial dependence of the states of the reduced order model.

is to construct a local linear model directly from the full order model (Fig. 6.7). The local linear approximation we will demonstrate here is shown in Fig. 6.8. It models the local behavior of the mesh with the nodes, springs and dampers near the instrument.

The frequency response of the local linear approximation, along with the frequency responses of the full linear model and a reduced order system with the same number of states as the local linear approximation calculated by balanced order reduction, are shown in Fig. 6.9. The local model approximates the behavior in the high frequency range, whereas its DC gain is significantly off. However, it is important to note that the local model is used only to estimate the intersample behavior of the full model, and therefore only needs to be close to the full model in the frequency range of around 10–1000 Hz, which is the case here. If necessary, it is possible to improve the low frequency accuracy by increasing the number of layers of nodes included around the instrument.

Another local linear approximation is shown in Fig. 6.10. This model approximates the behavior of the full order model over a wider frequency range. It includes the local

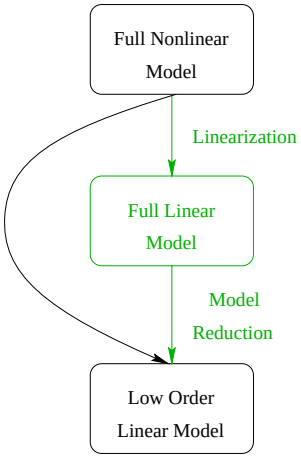

Figure 6.7: Construction of the low order model.

behavior of the mesh from the spring and dampers right around the instrument, and the steady state behavior from the outermost connection of spring and dampers. The interior springs and dampers have the same coefficients as in the original mesh. Coefficients of the outer elements are scaled to reflect the fact that the equivalent stiffness of a fixed sized block changes as the mesh density is changed. The mass parameters of the nodes are also scaled according to their distance to the end of the specimen. The scaling rules are generalized form the one dimensional case, as described in section 6.4.2. The square root of the scaling estimated from Fig. 6.16 is used for the surface elements. The frequency response of this local approximation is shown in Fig. 6.11. Qualitatively, this local approximation captures the first cut-off and the overall shape of the Bode plot of the full order model.

These results show that the local linear approximation is a suboptimal approximation, as expected. But it can be constructed on the fly with minimal computation and give sufficiently accurate behavior in the frequency range of interest.

6.4.1 One Dimensional Case — Motivation for the Construction of Local Approximations

Consider the lumped element chain shown in Fig. 6.12. The transfer function from displacement x to interaction force f of this model is

$$\frac{F}{X} = (k+bs)\left[1 - \frac{(k+bs)\left((ms^2+2bs+2k)^2-(k+bs)^2\right)}{(ms^2+2bs+2k)\left((ms^2+2bs+2k)^2-2(k+bs)^2\right)}\right]. \tag{6.6}$$

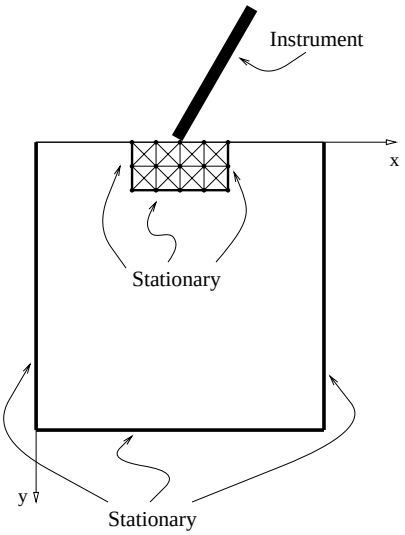

Figure 6.8: Local low order approximation.

The poles of this transfer function are at

$$\frac{-(2-\sqrt{2})b \pm \sqrt{((2-\sqrt{2})b)^2 - 4m(2-\sqrt{2})k}}{2m}, \tag{6.7}$$

$$\frac{-2b \pm \sqrt{4b^2 - 8mk}}{2m}, \tag{6.8}$$

$$\frac{-(2+\sqrt{2})b \pm \sqrt{((2+\sqrt{2})b)^2 - 4m(2+\sqrt{2})k}}{2m}. \tag{6.9}$$

It has high frequency asymptote $(k + bs)$ and DC gain $k/4$.

The first local model proposed considers only the pair of states closest to the interaction, i.e the position and velocity of the first mass, and assumes all the other masses stay stationary (Fig. 6.13). The transfer function of this model is given by

$$\frac{F}{X} = (k + bs)\left[1 - \frac{(k + bs)}{(ms^2 + 2bs + 2k)}\right] \tag{6.10}$$

which has poles at

$$\frac{-2b \pm \sqrt{4b^2 - 8mk}}{2m} \tag{6.11}$$

high frequency asymptote $(k + bs)$ and DC gain $k/2$.

The second local model shown in Fig. 6.14 tries to approximate the behavior of the full model over the low frequency range as well as the high frequency region by including the interior springs connected to the edge of the object. The coefficients of the interior

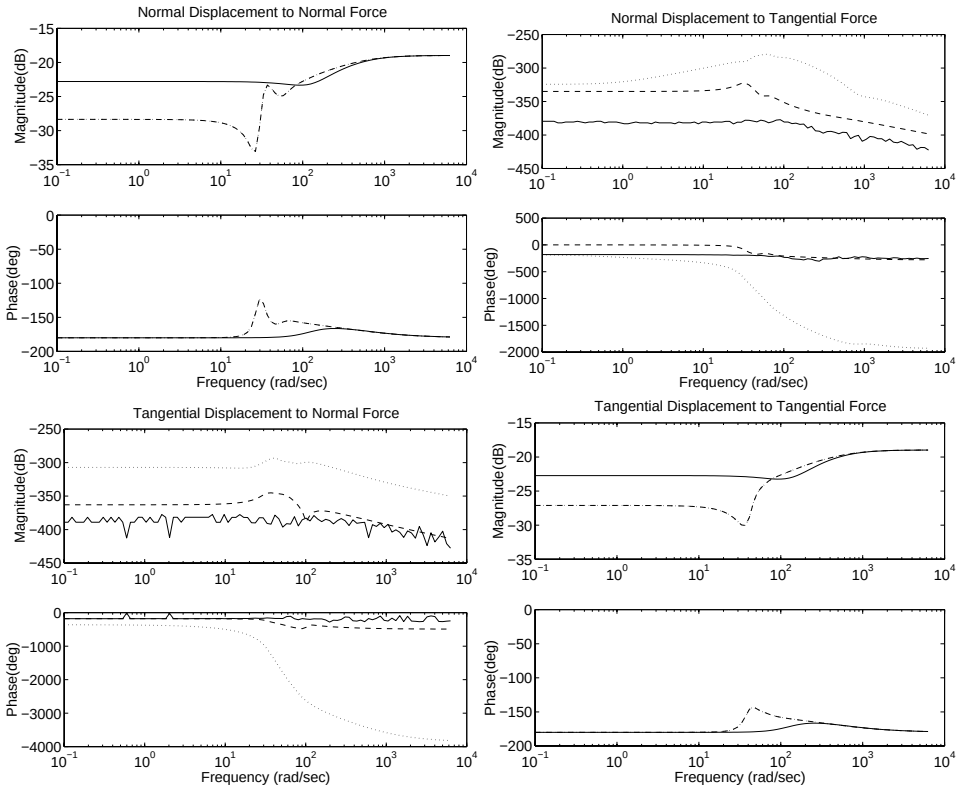

Figure 6.9: Frequency responses of the local linear approximation (solid line), full linear model (dashed line) and reduced order model (dotted line).

spring and damper are chosen to be the equivalents[2]of the three interior layers of the full model. The masses of the nodes removed form the full model to get to the two level model is equally distributed to the neighboring nodes in the two level model. The transfer function of this model is given by

$$\frac{F}{X} = (k + bs)\left[1 - \frac{(k + bs)}{(2ms^2 + \frac{4}{3}bs + \frac{4}{3}k)}\right] \tag{6.12}$$

which has poles at

$$\frac{-\frac{2}{3}b \pm \sqrt{(\frac{2}{3}b)^2 - \frac{8}{3}mk}}{2m} \tag{6.13}$$

high frequency asymptote $(k + bs)$ and DC gain $k/4$.

[2]Note that this spring damper configuration replacing the interior three layers is not exactly equal to the Norton equivalent of these as proposed in [6]. Rather the values used are the stiffness (damping) of the interconnection when only springs (dampers) are used. This results in a lower order approximation, whereas the Norton equivalent of the interconnection would have the same order as the network replaced.

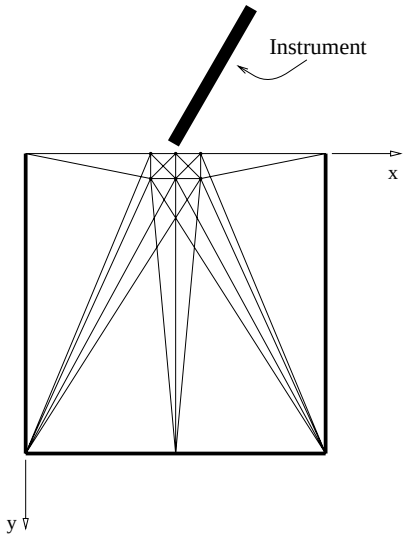

Figure 6.10: Local low order approximation with better low frequency response.

It can be observed from the frequency responses of these models shown in Fig. 6.15 that the first local model can only match the high frequency response, whereas the second local model can approximate the high and low frequency asymptotes as well as the two low frequency poles of the full model.

6.4.2 Element Coefficient Scaling in the Two and Three Dimensional Cases

In order to be able to generalize the local approximation shown in Fig. 6.14 to higher dimensions, we need to establish how the equivalent stiffness changes when the mesh density is changed. Fig. 6.16 shows the change in the largest singular value of the stiffness matrix of two and three dimensional lumped element mesh blocks as the interior mesh density is changed.

6.5 Implementation

We have implemented the paradigm explained above in a real time VE simulation of manipulation of a deformable object. The object used is a $6 \times 6 \times 6$ lumped element model. The local low order model used is the three dimensional extension of the model shown in Fig. 6.8. In the simulation, the full nonlinear model is updated at 20 Hz, whereas

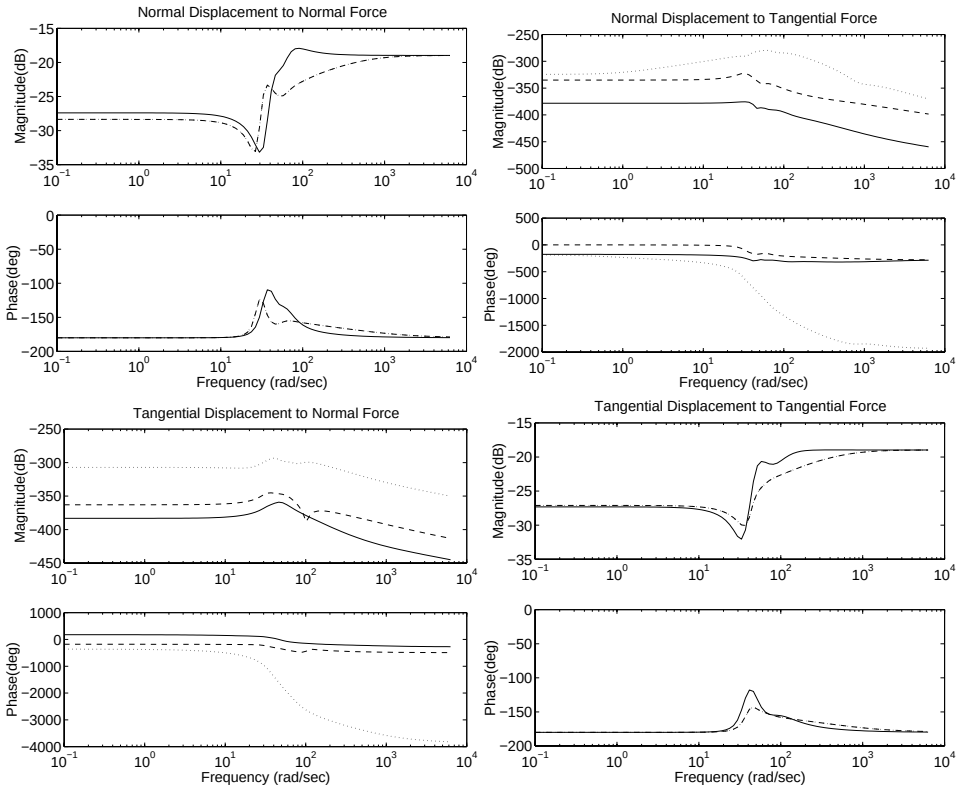

Figure 6.11: Frequency responses of the second local linear approximation (solid line), full linear model (dashed line) and reduced order model (dotted line).

the haptics and the local linear approximation is run at 1 kHz. It is important to note that the size of the full order nonlinear object model can be scaled without affecting the performance of the haptic interaction. The computational requirements of the construction of the local model and the haptic loop is fixed and independent of the size of the full order model.

It is also important to have a contact surface in the model. This is to insure that the linear model will be only pushing the instrument during contact. This is achieved simply by applying the interaction force feedback only if the component of the force in the surface normal direction is smaller than zero, and giving zero force otherwise.

The simulation is implemented in C++, using OpenGL as the graphics library. It is run on a dual processor SGI Octane computer. A Phantom(TM) version 1.5 manipulator is used as the haptic interface.

The force during interaction is shown in Fig. 6.17. The dashed line shows the

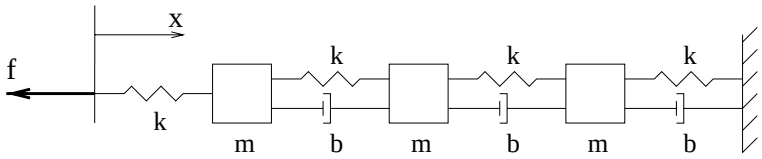

Figure 6.12: Four layer lumped element chain.

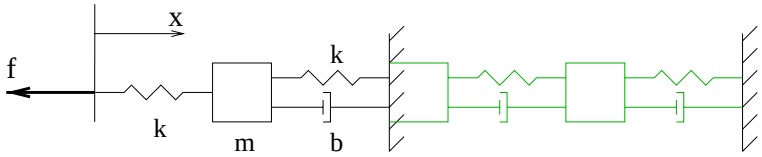

Figure 6.13: Approximation of the four layer lumped element chain. This local model approximates only the high frequency behavior of the full order model.

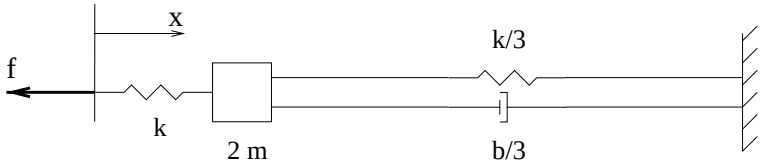

Figure 6.14: Second approximation of the four layer lumped element chain. This local model is constructed to approximate high and low frequency behavior of the full order model.

force calculated by the low update rate model, and the solid line shows the force displayed by the local linear model at the haptic update rate.

Stability Implications

Stability of haptic interaction with VEs is an important consideration for design of haptic interfaces and virtual objects. The update rate of the simulation is one of the critical determinants of the stability of interaction, where increasing the update rate of the model improves stability [70, 22]. In the method we are proposing, having the low order linear model running at a faster update improves the stability of the haptic interaction as the VE model runs at 1 kHz instead of 10 Hz.

This effect can also be observed in the implementation of our method described above. However, stability of our method is difficult to analyze theoretically because the resulting system is a multirate nonlinear sampled-data system. In the simulation, if the local linear approximation is not used, the haptic interface tends to have oscillatory behavior when the operator loosens his/her grip (Fig. 6.18). This oscillatory behavior is not present with the local linear approximation even when the operator completely releases the instrument.

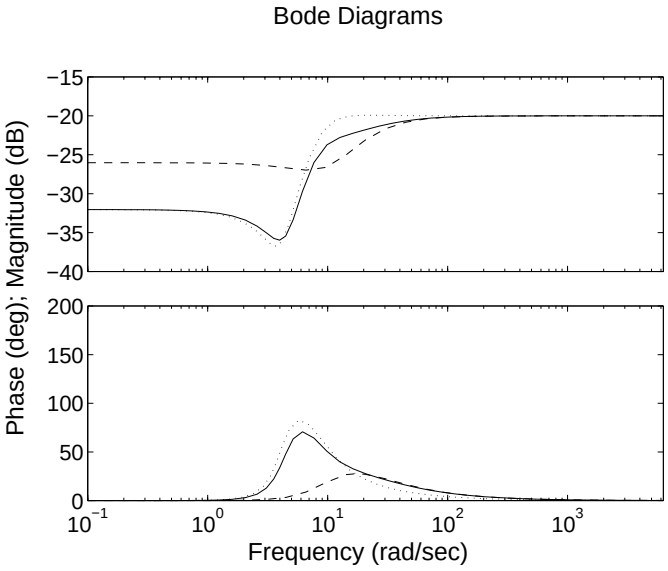

Figure 6.15: Frequency responses of the full order model (solid) and the first (dashed) and second (dotted) local models.

6.6 Discussion

In this chapter, a multirate simulation approach to handle the difference between the sampling rate requirements of the haptics and the possible update rates of the physical models during haptic interaction with deformable objects in VE simulations is presented. The proposed method uses a linear approximation to model the intersample behavior of the nonlinear full order model. The natural choice of the linear approximation is to use the linearization of the nonlinear dynamics, which gives the tangent behavior of the dynamical system. However, this linearization does not completely solve the computational complexity problem since the order of the linearized model is still very high. We performed balanced model reduction on the linearized model and showed that it is possible to use a low order local approximation and still get an accurate input output response. Based on this analysis, we proposed two simple local linear approximations which can be computed in real-time, and implemented one of them in a simulation to verify the method.

Among the two local linear approximations, the first one, shown in Fig.'s 6.8 and 6.13, is easier to construct and has good accuracy in high frequency behavior. It is therefore preferred over the second local approximation model.

The local states must be the dominant modes for this method to be applicable.

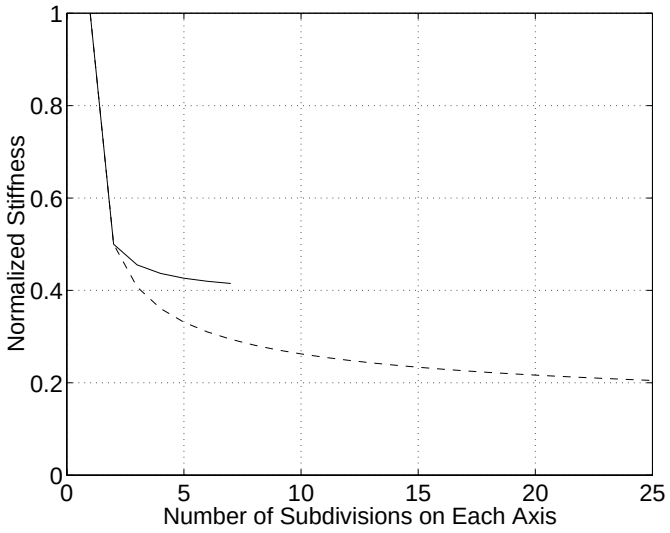

Figure 6.16: Change in stiffness of a block with change in mesh density for 3-D (solid) and 2-D (dashed) meshes.

This can be violated if the material is inhomogeneous, for example if the deep tissue is significantly more compliant than at the surface so that most of the deformation occurs in states far from the interaction. In this case, if the model is linear, Astley and Hayward's method [6] can be applied. Other effects that can violate the dominance of local modes include significant geometric nonlinearities or discontinuities in the tissue that produced large local stresses away from the instrument contact. Another important degenerate case is when the object being manipulated is stiff and there is rigid motion. In this case, the interaction forces generated are determined mostly by the inertia of the object, not the local deformations. However, the locality of the dominant modes can always be checked by performing off-line model reduction, as it is done here in section 6.3.

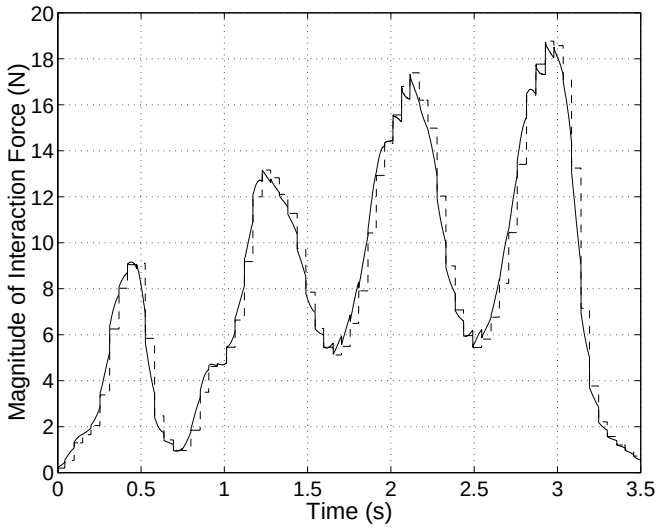

Figure 6.17: Interaction force during manipulation of a deformable virtual object.

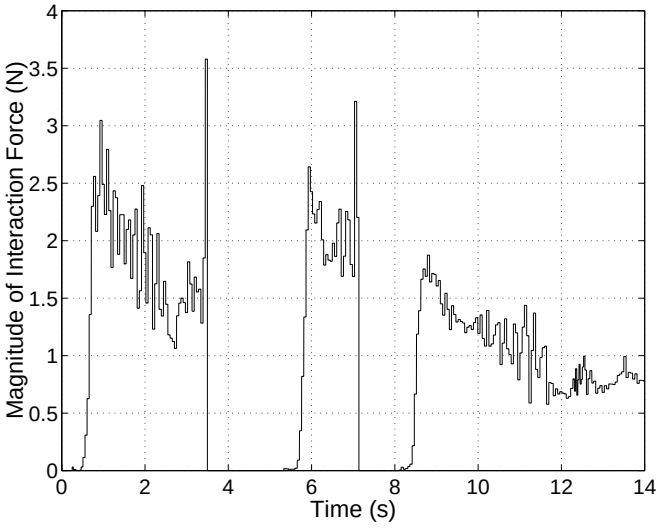

Figure 6.18: Oscillations observed when the local linear approximation is not used.

Chapter 7

Conclusion

The emphasis in this dissertation was on the application of systems and control engineering and robotics methodology to the research problems in telesurgery and surgical simulation. This gave a unified framework to approach all aspects of the problems shown in Fig. 7.1 from control design to manipulator design, tissue modeling and dynamical simulation, and even to as far as psychophysics issues.

The work on telesurgery was centered around the UC Berkeley/UC San Francisco Laparoscopic Telesurgical Workstation, focusing on the design and analysis of the system, with details of the design specifications, solution of the forward and inverse kinematics, and control issues, followed by a discussion on the experimental evaluation of the laparoscopic telesurgical workstation. We have also studied the high fidelity teleoperation controller design for the telesurgical system, establishing a theoretical and experimental framework developed for design and evaluation of teleoperation controllers for telemanipulation of deformable objects.

For the surgical simulation, we have discussed the general problems in dynamical simulation of deformable objects, with a critical look at the existing methodologies in the literature, mostly focusing on formulating the problem and putting the existing methodologies into a unifying framework, and studying the problem of high fidelity haptic interaction with deformable objects in virtual environments from a control theory point of view.

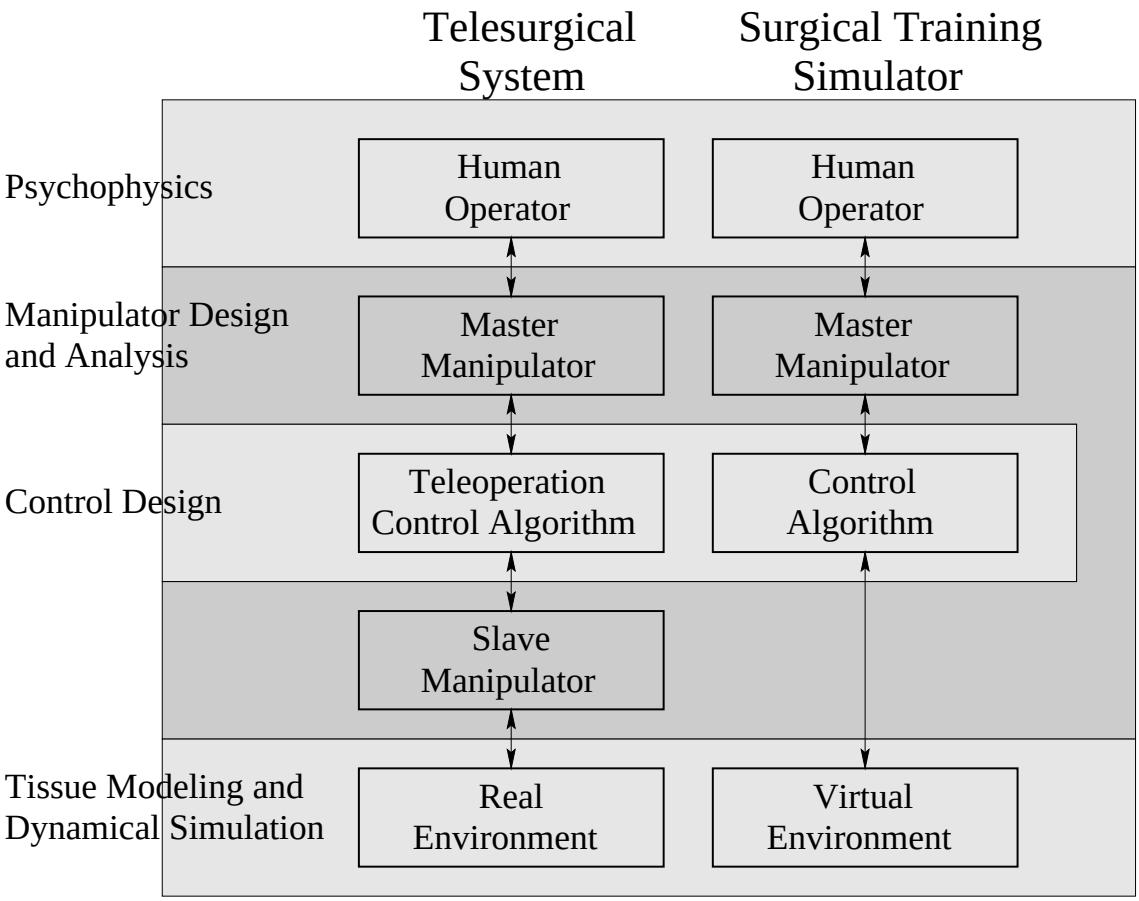

Figure 7.1: Telesurgery and surgical simulation are parallel research problems. Repeated form Fig. 1.4.

7.1 Future Research Problems for the Robotic Telesurgical Workstation

The research on the telesurgical workstation will proceed in several directions. First part will be on improving the master workstation. It has been reported that immersive displays for telesurgical applications improve performance. It is necessary to quantitatively evaluate the effect of using an immersive display. It is also important to study the effects of the camera motion and the discrepancies it causes between the haptic and visual spaces. This effect is more important for the immersive display system, but needs to be studied for both immersive and non-immersive user interfaces.

Further evaluation of the second generation system is necessary. Especially, it is

important to perform complete surgical procedures to have a comprehensive evaluation. This will give specifications for the design of the third generation system for human testing.

Another thrust of the research on robotic telesurgery will be the design of new manipulators for smaller scale procedures such as cardiac surgery and fetal surgery. It may be possible to go to the scale for some cardiac applications with the existing technology, i.e. with tendons, but for smaller scale it is necessary to have novel actuators and mechanical designs.

Continuation of the research on high fidelity teleoperation is important, because it is necessary to have a methodology to guide the design of manipulators at smaller scale. An interesting research problem here is looking at the mechanical design of teleoperation systems from a control point of view, to reveal the requirements on the mechanical design for better controllability and higher achievable closed loop performance.

A longer term research challenge is the development of a system for surgery on the beating heart, which has several interesting research problems. For such a system, tracking of the motion of the heart is critical, which includes modeling the motion and estimation of the motion from mechanical and biological signals, such as EKG and blood pressure. It is also necessary to build a manipulator with sufficient bandwidth and redundancy to track the motion, yet provide sufficient dexterity to be able to perform surgery. A macro-micro manipulator design might be required, where the macro motion stage will track the motion of the heart and the micro motion stage will be used for fine manipulation.

7.2 Future Research Problems for the Surgical Training Simulator

As discussed in the earlier chapters, real-time simulation of deformable tissue is an enabling technology for the development of surgical simulators. Therefore, for the surgical simulation project, the focus in the near future needs to be on deformable tissue modeling for dynamical simulation. It is necessary to construct fast, interactive and realistic models.

Clearly, part of the computational problem will diminish as increasing computing power becomes available. However, there is still need for genuine research to build realistic and efficient deformable tissue models and improving haptic interaction with these models. Understanding the mathematical and dynamical structure of these computational problems

offers alternative means of reducing the computational complexity. It is also important to continue the research on bridging the gap between finite element, finite difference, and lumped element models, i.e. computer scientists and mechanical engineers.

Development of teaching methodologies and verification of transfer of skills from the simulator to actual surgery are also critical parts of the research that need to be addressed.

Appendix A

Product of Exponentials Formulation of Robot Kinematics

For the kinematic analysis, the product of exponentials formulation is used. Here, this method will be briefly introduced, without proofs. Refer to [74] for a full treatment.

Fist we give a few definitions:

Definition 1 (Special Orthogonal Group)

$$SO(3) = \{R \in \mathbf{R}^{3\times 3} : RR^T = I, det(R) = +1\} \tag{A.1}$$

The special orthogonal group is the set of rigid body rotations in $\mathbf{R}^3$.

Definition 2 (Infinitesimal Rotations)

$$so(3) = \{S \in \mathbf{R}^{3\times 3} : S^T = -S\} \tag{A.2}$$

is the vector space of 3×3 *skew symmetric matrices.*

Lemma 1 *Given a skew symmetric matrix*

$$\hat{w} = \begin{bmatrix} 0 & -w_3 & w_2 \\ w_3 & 0 & -w_1 \\ -w_2 & w_1 & 0 \end{bmatrix} \in so(3) \tag{A.3}$$

and $\theta \in \mathbf{R}$, *the matrix exponential* $e^{\hat{w}\theta} \in SO(3)$, *which corresponds to the rotation of* $||w||\theta$ *radians around the axis* $w = \begin{bmatrix} w_1 & w_2 & w_3 \end{bmatrix}^T$. *The exponential map from* $so(3)$ *to* $SO(3)$ *is surjective.*

Definition 3 (Special Euclidean Group) *The space of rigid motions in* $\mathbf{R}^3$ *is a group, called the special Euclidean group, defined as*

$$SE(3) = \{(p, R) : p \in \mathbf{R}^3, R \in SO(3)\} \tag{A.4}$$

which can be represented by 4×4 *matrices of the form*

$$\begin{bmatrix} R & p \\ 0 & 1 \end{bmatrix} \tag{A.5}$$

operating on homogeneous coordinates of points and vectors.

Definition 4 (Infinitesimal Rigid Motions)

$$se(3) = \{(v, \hat{w}) : v \in R^3, \hat{w} \in so(3)\} \tag{A.6}$$

An element $\hat{\xi} = \begin{bmatrix} \hat{w} & v \\ 0 & 0 \end{bmatrix} \in se(3)$ *is called a twist and is parameterized by the vector* $\xi = \begin{bmatrix} v \\ w \end{bmatrix} \in \mathbf{R}^6$.

Lemma 2 *The generator of* $SE(3)$ *is* $se(3)$*, i.e., given* $\hat{\xi} \in se(3)$ *and* $\theta \in \mathbf{R}$, $e^{\hat{\xi}\theta} \in SE(3)$. *The exponential map from* $se(3)$ *to* $SE(3)$ *is surjective.*

In the product of exponentials formulation, the forward kinematics map ($Q \rightarrow SE(3)$) of an open chain manipulator is represented as a product of exponentials of the twists associated with the joint axis as

$$g_s t(\theta) = e^{\hat{\xi}_1 \theta_1} e^{\hat{\xi}_2 \theta_2} \ldots . e^{\hat{\xi}_n \theta_n} g_{st}(0) \tag{A.7}$$

where ξ_i is the twist associated with joint i and $g_{st}(0)$ is the rigid body transformation between the tool and spatial coordinate frames (T and S respectively) at the reference configuration where $\theta_i = 0$. The joints are numbered sequentially from the base to tool as $1 \ldots n$. ξ_i are the constant twists constructed by evaluating the screw motion for the i'th joint with all other joints fixed at $\theta_j = 0$.

Bibliography

[1] R. J. Adams and B. Hannaford. Stable haptic interaction with virtual environments. *IEEE Transactions on Robotics and Automation*, 15(3):465–474, June 1999.

[2] B. D. O. Anderson. *Optimal Filtering*. Prentice Hall, Inc., Englewood Cliffs, NJ, USA, 1979.

[3] R. J. Anderson and M. W. Spong. Bilateral control of teleoperators with time delay. *IEEE Transaction on Automatic Control*, 34(5):494–501, May 1989.

[4] R. J. Anderson and M. W. Spong. Asymptotic stability for force reflecting teleoperators with time delay. *International Journal of Robotics Research*, 11(2):135–148, April 1992.

[5] F. Arai, M. Tanimoto, T. Fukuda, K. Shimojima, H. Matsuura, and M. Negoro. Multimedia tele-surgery using high speed optical fiber network and its applications to intravascular neurosurgery — system configuration and computer networked implementation. In *Proceedings of the IEEE International Conference on Robotics and Automation*, volume 1, pages 878–883, 1996.

[6] O. R. Astley and V. Hayward. Multirate haptic simulation achieved by coupling finite element meshes through norton equivalents. In *Proceedings of the IEEE International Conference on Robotics and Automation (ICRA'98)*, pages 989–994, May 1998.

[7] J. Baillie, P. Jowell, H. Evangelou, W. Bickel, and P.Cotton. Use of computer graphics simulation for teaching of flexible sigmoidoscopy. *Endoscopy*, 23:126–9, 1991.

[8] K. Bathe. *Finite Element Procedures*. Prentice Hall, Inc., Englewood Cliffs, NJ, USA, 1996.

[9] D.J. Blezek, R.A. Robb, J.J. Camp, L.A. Nauss, and D.P Martin. Simulation of spinal nerve blocks for training anesthesiology residents. In *SPIE Conference 3262 on Surgical-Assist Systems*, pages 45–53, San Jose, CA, January 1998.

[10] D. H. Boehm, H. Reichenspurner, H. Gulbins, C. Detter, B. Meiser, P. Brenner, H. Habazettl, and B. Reichart. Early experience with robotic technology for coronary artery surgery. *Annals of Thoracic Surgery*, 68(4):1542–1546, October 1999.

[11] J. C. Bowersox and R. L. Cornum. Remote operative urology using a surgical telemanipulator system: preliminary observations. *Urology*, 52(1):17–22, July 1998.

[12] M. Bro-Nielsen. Fast finite elements for surgery simulation. In J.D. Westwood et al., editors, *Medicine Meets Virtual Reality: 5*, Amsterdam, 1997. IOS Press.

[13] M. Bro-Nielsen. Finite element modeling in surgery simulation. *Proceedings of the IEEE*, 86(3):490–503, March 1998.

[14] M. Bro-Nielsen, J.L. Tasto, R. Cunningham, and G.L. Merril. PreOp endoscopic simulator: a PC-based immersive training system for bronchoscopy. In J.D. Westwood et al., editors, *Medicine Meets Virtual Reality: 7*, pages 76–82, Amsterdam, 1999. IOS Press.

[15] G. B. Cadiére, J. Himpens, M. Vertruyen, J. Bruyns, and G G. Fourtanier. Fundoplicature selon nissen réalisée à distance du patient par robotique. [nissen fundoplication done by remotely controlled robotic technique]. *Annales de Chirurgie*, 53(2):137–141, 1999. In French.

[16] M. C. Çavuşoğlu, M. Cohn, F. Tendick, and S. S. Sastry. Laparoscopic telesurgical workstation. In *Video Proceedings of the IEEE International Conference on Robotics and Automation (ICRA 1999)*, 1999.

[17] M. C. Çavuşoğlu, F. Tendick, M. Cohn, and S. S. Sastry. A laparoscopic telesurgical workstation. *IEEE Transactions on Robotics and Automation*, 15(4):728–739, August 1999.

[18] F. J. Clark and K. W. Horch. Handbook of perception and human performance. In K. R. Boff, L. Kaufman, and J. P. Thomas, editors, *Kinesthesia*, volume I, Sensory Processes and Perception, chapter 13. John Wiley and Sons, Inc., 1986.

[19] K. R. Cleary, C. E. Lathan, and C. Carignan. Simulator/planner for CT-directed needle biopsy of the spine. In *SPIE Conference 3262 on Surgical-Assist Systems*, pages 218–224, San Jose, CA, January 1998.

[20] M. Cohn, L. S. Crawford, J. M. Wendlandt, and S. S. Sastry. Surgical applications of milli-robots. *Journal of Robotics Systems*, 12(6):401–416, June 1995.

[21] M. B. Cohn, M. Lam, and R. S. Fearing. Tactile feedback for teleoperation. In *Proceedings of the SPIE*, volume 1833, pages 240–254, 1993.

[22] J. E. Colgate. Robust impedance shaping telemanipulation. *IEEE Transactions on Robotics and Automation*, 9(4):374–384, August 1993.

[23] J. E. Colgate, M. C. Stanley, and J. M. Brown. Issues in the haptic display of tool use. In *Proceedings of the IEEE/RSJ International Conference on Intelligent Robotics and Systems (IROS'95)*, pages 140–145, 1995.

[24] K. D. Costa, P. J. Hunter, J. M. Rogers, J. M. Guccione, L. K. Waldman, and A. D. McCulloch. A three-dimensional finite element method for large elastic deformations of ventricular myocardium: Part i - cylindrical and spherical polar coordinates. *ASME Journal of Biomechanical Engineering*, 118:452–463, 1996.

[25] K. D. Costa, P. J. Hunter, J. M. Rogers, J. M. Guccione, L. K. Waldman, and A. D. McCulloch. A three-dimensional finite element method for large elastic deformations of ventricular myocardium: Part ii - prolate spherical coordinates. *ASME Journal of Biomechanical Engineering*, 118:464–472, 1996.

[26] S. Cotin, H. Delingette, and N. Ayache. Real-time elastic deformations of soft tissues for surgery simulation. *IEEE Transactions on Visualization and Computer Graphics*, 5(1):62–73, January–March 1999.

[27] R. W. Daniel and P. R. McAree. Fundamental limits of performance for force reflecting teleoperation. *International Journal of Robotics Research*, 17(8):811–830, August 1998.

[28] P. Dario, E. Guglielmelli, B. Allotta, and M. C. Carrozza. Robotics for medical applications. *IEEE Robotics and Automation Magazine*, 3(3):44–56, 1996.

[29] H. Das, H. Zak, W. S. Kim, A. K. Bejczy, and P. S. Schenker. Operator performace with alternative manual control modes in teleoperation. *Presence*, 1(2):201–218, Spring 1992.

[30] D. d'Aulignac, C. Laugier, and M. C. Çavuşoğlu. Towards a realistic echographic simulator with force feedback. In *Proceedings of the IEEE/RSJ International Conference on Intelligent Robotics and Systems (IROS'99)*, pages 727–732, October 1999.

[31] H. Delingette, S. Cotin, and N. Ayache. Efficient linear elastic models of soft tissues for real-time surgery simulation. In J.D. Westwood et al., editors, *Medicine Meets Virtual Reality: 7*, Amsterdam, 1999. IOS Press.

[32] N. Dhruv and F. Tendick. Frequency dependence of compliance contrast detection. In *Submitted to the Symposium on Haptic Interfaces for Virtual Environment and Teleoperator Systems , part of the ASME International Mechanical Engineering Congress and Exposition (IMECE 2000)*, November 2000.

[33] P. Dubois, P. Meseure, F. Peugnet, and J.-F. Rouland. Training simulator for retinal laser photocoagulation: a new approach for surgeons' apprenticeships. In *SPIE Conference 3262 on Surgical-Assist Systems*, pages 54–62, San Jose, CA, January 1998.

[34] R. S. Fearing, G. Moy, and E. Tan. Some basic issues in teletaction. In *Proceedings of the IEEE International Conference on Robotics and Automation*, volume 4, pages 3093–3099, 1997.

[35] Y. C. Fung. *Biomechanics : mechanical properties of living tissues.* Springer-Verlag, New York, NY, USA, 1981.

[36] A. Garcia-Ruiz, M. Gagner, J. H. Miller, C. P. Steiner, and J. F. Hahn. Manual vs robotically assisted laparoscopic surgery in the performance of basic manipulation and suturing tasks. *Archieves of Surgery*, 133(9):957–961, September 1998.

[37] S. Gibson, J. Samosky, A. Mor, C. Fyock, E. Grimson, and T. Kanade. Simulating arthroscopic knee surgery using volumetric object representations, real-time volume rendering and haptic feedback. In J. Troccaz, E. Grimson, and R. Mosges, editors, *Proc. First Joint Conf. Computer Vision, Virtual Reality and Robotics in Medicine*

and Medical Robotics and Computer-Assisted Surgery (CVRMed-MRCAS), pages 369–378, Berlin, 1997. Springer.

[38] E. Graves. *Vital and Health Statistics.* Data from the National Health Survey No. 122. U.S. Department of Health and Human Services, Hyattsville, MD, 1993.

[39] B. L. Gray and R. S. Fearing. A surface micromachined microtactile sensor array. In *Proceedings of the IEEE International Conference on Robotics and Automation*, volume 1, pages 1–6, 1996.

[40] M. E. Gurtin. *An Introduction to Continuum Mechanics.* Academic Press, New York, NY, USA, 1981.

[41] M. E. Gurtin. *Topics in Finite Elasticity.* Society for Industrial and Applied Mechanics, Philadelphia, PA, USA, 1981.

[42] B. Hannaford. A design framework for teleoperators with kinesthetic feedback. *IEEE Transactions on Robotics and Automation*, 5(4):426–434, August 1989.

[43] B. Hannaford. Stability and performance tradeoffs in bi-lateral telemanipulation. In *Proceedings of the IEEE International Conference on Robotics and Automation*, pages 1764–1767, 1989.

[44] B. Hannaford, L. Wood, D. A. McAffee, and H. Zak. Performance evaluation of a six-axis generalized force-reflecting teleoperator. *IEEE Transactions on System, Man, and Cybernetics*, 21(3):620–633, May/June 1991.

[45] J. W. Hill, P. S. Green, J. F. Jensen, Y. Gorfu, and A. S. Shah. Telepresence surgery demonstration system. In *Proceedings of the IEEE International Conference on Robotics and Automation*, pages 2302–2307, 1994.

[46] Z. Hu, S. E. Salcudean, and P. D. Loewen. Robust controller design for teleoperation systems. In *Proceedings of the IEEE International Conference on Systems, Man and Cybernetics*, volume 3, pages 2127–2132, 1995.

[47] K. Ikuta, M. Takeichi, and T. Namiki. Virtual endoscope system with force sensation. In W.M. Wells, A. Colchester, and S. Delp, editors, *Proc. Intl. Conf. Medical Image Computing and Computer-Assisted Intervention (MICCAI)*, pages 293–304, Berlin, 1998. Springer.

[48] D. L. James and D. K. Pai. ARTDEFO: Accurate real time deformable objects. In *Proceedings of SIGGRAPH 99: 26th International Conference on Computer Graphics and Interactive Techniques*, pages 65–72. ACM, 1999.

[49] L. A. Jones and I. W. Hunter. Influence of the mechanical properties of a maniplandum on human operator dynamics, i. elastic stiffness. *Biological Cybernetics*, 62(4):299–307, 1990.

[50] L. A. Jones and I. W. Hunter. A perceptual analysis of stiffness. *Experimental Brain Research*, 79(1):150–156, 1990.

[51] L. A. Jones and I. W. Hunter. Influence of the mechanical properties of a maniplandum on human operator dynamics, ii. viscosity. *Biological Cybernetics*, 69(4):295–303, 1993.

[52] L. A. Jones and I. W. Hunter. A perceptual analysis of viscosity. *Experimental Brain Research*, 94(2):343–351, 1993.

[53] L. A. Jones and I. W. Hunter. Analysis of the human operator controlling a teleoperated microsurgical robot. In *Proceedings of 6th IFAC/IFIP/IFORS/IEA Symposium on Analysis, Design and Evaluation of Man-Machine Systems*, pages 593–597, 1995.

[54] A. Joukhadar, F. Garat, and C. Laugier. Parameter identification for dynamic simulation. In *Proceedings of the IEEE International Conference on Robotics and Automation (ICRA'97)*, pages 1928–1933, April 1997.

[55] A. Joukhadar and C. Laugier. Dynamic simulation: Model, basic algorithms, and optimization. Preprint, 1998.

[56] H. Kazerooni, T.-I. Tsay, and K. Hollerbach. A controller design framework for telerobotic systems. *IEEE Transactions on Control Systems Technology*, 1(1):50–62, March 1993.

[57] W. S. Kim, B. Hannaford, and A. K. Bejczy. Force-reflection and shared compliant control in operating telemanipulators with time delay. *IEEE Transactions on Robotics and Automation*, 8(2):176–185, April 1992.

[58] D. A. Kontarinis, J. S. Son, W. Peine, and R. D. Howe. A tactile shape sensing and display system for teleoperated manipulation. In *Proceedings of the IEEE International Conference on Robotics and Automation (ICRA'95)*, volume 1, pages 641–646, 1995.

[59] U. G. Kuhnapfel, Ch. Kuhn, M. Hubner, H.-G. Krumm, H. Maass, and B. Neisius. The Karlsruhe endoscopic surgery trainer as an example for virtual reality in medical education. *Minimally Invasive Therapy and Allied Technologies*, 6:122–5, 1997.

[60] S. Lavallée, J. Troccaz, L. Gaborit, P.Cinquin, A. L. Benabid, and D. Hoffmann. Image guided operating robot: A clinical application in stereotactic neurosurgery. In R. H. Taylor, S. Lavallée, G. Burdea, and R. Mösges, editors, *Computer Integrated Surgery: Technology and Clinical Applications*. MIT Press, 1995.

[61] C. A. Lawn and B. Hannaford. Performance testing of passive communication and control in teleoperation with time delay. In *Proceedings of the IEEE International Conference on Robotics and Automation*, pages 776–783, 1993.

[62] D. A. Lawrence. Stability and transperancy in bilateral teleoperation. *IEEE Transactions on Robotics and Automation*, 9(5):624–637, October 1993.

[63] G. M. H. Leung, B. A. Francis, and J. Apkarian. Bilateral controller for teleoperators with time delay via mu-synthesis. *IEEE Transactions on Robotics and Automation*, 11(1):105–116, February 1995.

[64] F. L. Lewis. *Applied Optimal Control and Estimation, Digital Design and Implementation*. Prentics Hall, Inc., Englewood Cliffs, NJ, USA, 1992.

[65] K. Liu, J. M. Fitzgerald, and F. L. Lewis. Kinematic analysis of a stewart platform manipulator. *IEEE Transactions on Industrial Electronics*, 40(2):282–293, April 1993.

[66] A. J. Madhani, G. Niemeyer, and J. K. Salisbury. The black falcon: a teleoperated surgical instrument for minimally invasive surgery. In *Proceedings of the IEEE/RSJ International Conference on Intelligent Robots and Systems (IROS'98)*, volume 2, pages 936–944, 1998.

[67] J. E. Marsden and T. J. R. Hughes. *Mathematical foundations of elasticity*. Prentice-Hall, Inc., Englewood Cliffs, NJ, USA, 1983.

[68] A. McCarthy, P. Harley, and R. Smallwood. Virtual arthroscopy training: do the "virtual skills" developed match the real skills required? In J.D. Westwood et al., editors, *Medicine Meets Virtual Reality: 7*, pages 221–7, Amsterdam, 1999. IOS Press.

[69] D. N. Metaxas. *Physics-based deformable models : applications to computer vision, graphics, and medical imaging.* Kluwer Academic, Boston, USA, 1997.

[70] M. Minsky, M. Ouh-young, O. Steele, Jr. F. P. Brooks, and M. Behensky. Feeling and seeing: Issues in force display. In *Computer Graphics*, volume 24, pages 235–243, March 1990. ACM Symposium on Interactive 3D Graphics.

[71] B. Mirtich. *Impulse-based Dynamic Simulation of Rigid Body Systems.* PhD thesis, University of California, Berkeley, December 1996.

[72] G. Moy, C. Wagner, and R. S. Fearing. A compliant tactile display for teletaction. In *Proceedings of the IEEE International Conference on Robotics and Automation (ICRA 2000)*, 2000.

[73] W. Muller and U. Bockholt. The virtual reality arthroscopy training simulator. In J.D. Westwood et al., editors, *Medicine Meets Virtual Reality: 6*, pages 13–19, Amsterdam, 1998. IOS Press.

[74] R. M. Murray, Z. Li, and S. S. Sastry. *A Mathematical Introduction to Robotic Manipulation.* CRC Press, Inc., 1994.

[75] G. Niemeyer and J. J. E. Slotine. Stable adaptive teleoperation. *IEEE Journal of Oceanic Engineering*, 16(1):152–162, January 1991.

[76] J. W. Peifer, W. D. Curtis, and M. J. Sinclair. Applied virtual reality for simulation of endoscopic retrograde cholangio-pancreatography (ERCP). In S.J. Weghorst et al., editors, *Medicine Meets Virtual Reality: 4*, pages 36–42, Amsterdam, 1996. IOS Press.

[77] W. J. Peine, P. S. Wellman, and R. D. Howe. Temporal bandwidth requirements for tactile shape displays. In G. Rizzoni, editor, *Proceedings of ASME Dynamic Systems and Control Division*, pages 107–114, 1997.

[78] B. K. Poulose, M. F. Kutka, M. Mendoza-Sagaon, A. C. Barnes, C. Yang, R. H. Taylor, and M. A. Talamini. Human vs robotic organ retraction during laparoscopic Nissen fundoplication. *Surgical Endoscopy*, 13(5):461–465, May 1999.

[79] W. H. Press, S. A. Teukolsky, W .T. Vetterling, and B. P. Flannery. *Numerical Recipes in C : the Art of Scientific Computing*. Cambridge University Press, Cambridge, NY, 2nd edition, 1992.

[80] J. N. Reddy. *An Introduction to the Finite Element Method*. McGraw-Hill, Inc., 2nd edition, 1993.

[81] A. Rovetta, R. Sala, X. Wen, and A. Togno. Remote control in telerobotic surgery. *IEEE Transactions on Systems, Man, and Cybernetics—Part A:Systems and Humans*, 26(4):438–443, July 1996.

[82] S. E. Salcudean and T. D. Vlaar. On the emulation of stiff walls and static friction with a magnetically levitated input/output device. *Journal of Dynamical Systems*, 119:127–132, March 1997.

[83] SensAble Technologies, Cambridge, MA. *PHANToM(TM) Haptic Interface Hardware Installation and Technical Manual*, 1997. Revision 5.1.

[84] A. Sherman. Comparison of teleoperator control architectures for a compliance discrimination task. Master's thesis, Department of Mechanical Engineering, University of California, Berkeley, 2000.

[85] A. Sherman, M. C. Çavuşoğlu, and F. Tendick. Comparison of teleoperator control architectures for palpation task. In *Proceedings of the Symposium on Haptic Interfaces for Virtual Environment and Teleoperator Systems , part of the ASME International Mechanical Engineering Congress and Exposition (IMECE 2000)*, November 2000.

[86] M.J. Sinclair, J.W. Peifer, R. Haleblian, M.N. Luxenberg, K. Green, and D.S. Hull. Computer-simulated eye surgery: a novel teaching method for residents and practitioners. *Ophthalmology*, 102(3):517–521, 1995.

[87] S. Smith, A. Wan, N. Taffinder, S. Read, R. Emery, and A. Darzi. Early experience and validation work with Procedicus VA—the Prosolvia virtual reality shoulder arthroscopy trainer. In J.D. Westwood et al., editors, *Medicine Meets Virtual Reality: 7*, pages 337–343, Amsterdam, 1999. IOS Press.

[88] M. A. Srinivasan and R. H. LaMotte. Tactual discrimination of softness. *Journal of Nerophysiology*, 23(1):88–101, January 1995.

[89] P. S.Schenker, H. Das, and T. R. Ohm. A new robot for high dexterity microsurgery. In N. Ayache, editor, *Computer Vision, Virtual Reality and Robotics in Medicine. First International Conference, CVRMed'95. Proceedings.*, pages 115–122, Berlin, Germany, 1995. Springer-Verlag.

[90] J. C. Strikwerda. *Finite difference schemes and partial differential equations.* Chapman & Hall, New York, NY, 1989.

[91] G. T. Sung, I. S. Gill, and T. H. Hsu. Robotic-assisted laparoscopic pyeloplasty: a pilot study. *Urology*, 53(6):1099–1103, June 1999.

[92] G. Szekely, M. Bajka, Ch. Brechbuhler, J. Dual, R. Enzler, U. Haller, et al. Virtual reality based surgery simulation for endoscopic gynaecology. In J.D. Westwood et al., editors, *Medicine Meets Virtual Reality: 7*, pages 351–357, Amsterdam, 1999. IOS Press.

[93] R. H. Taylor, J. Funda, B. Eldridge, S. Gomory, K. Gruben, D. LaRose, M. Talamini, L. Kavoussi, and J. Anderson. A telerobotics assistant for laparoscopic surgery. *IEEE Engineering in Medicine and Biology Magazine*, 14(3):279–288, May–June 1995.

[94] R. H. Taylor, S. Lavallée, G. Burdea, and R. Mösges, editors. *Computer-Integrated Surgery: Technology and Clinical Applications.* MIT Press, Cambridge, MA, 1996.

[95] R. H. Taylor, B. D. Mittelstadt, H. A. Paul, W. Hanson, P. Kazanzides, et al. An image-directed robotics system for precise orthopaedic surgery. *IEEE Transactions on Robotics and Automation*, 10(3):261–275, June 1994.

[96] F. Tendick, M. C. Çavuşoğlu, N. Dhruv, and A. Sherman. Maximizing the sensation of compliance in teleoperative surgery. In *Proceedings of the Eighth International Symposium on Robotics with Applications, part of the World Automation Congress (WAC 2000)*, June 2000.

[97] F. Tendick, R. W. Jennings, G. Tharp, and L. Stark. Sensing and manipulation problems in endoscopic surgery: Experiment, analysis and observation. *Presence*, 2(1):66–81, 1993.

[98] D. Terzopoulos, J. Platt, A. Barr, and K. Fleischer. Elastically deformable models. In *Proceedings of SIGGRAPH 87: 14th Annual Conference on Computer Graphics*, pages 205–214. ACM, July 1987.

[99] S. Timoshenko and J. N. Goodier. *Theory of Elasticity.* McGraw-Hill Book Company, Inc., New York, USA, second edition, 1951.

[100] R. Tombropoulos, A. Schweikard, J. C. Latombe, and J. R. Adler. Treatment planning for image-guided robotic radiosurgery. In N. Ayache, editor, *Computer Vision, Virtual Reality and Robotics in Medicine. First International Conference, CVRMed '95. Proceedings.*, pages 131–137, Berlin, Germany, 1995. Springer-Verlag.

[101] U.S. Department of Health and Human Services, Public Health Service, Food and Drug Administration, Center for Devices and Radiological Health, Rockville, Maryland 20850. *Premarket approval manual*, January 1998. HHS Publication FDA 97-4214.

[102] I. Villanueva. Acquisition of surgical movement data and analysis using screw coordinates. Master's thesis, Department of Mechanical Engineering, University of California, Berkeley, 2000.

[103] L. W. Way, S. Bhoyrul, and T. Mori, editors. *Fundamentals of Laparoscopic Surgery.* Churchill Livingstone, 1995.

[104] P. S. Wellman, R. D. Howe, N. Dewagan, M. A. Cundari, E. Dalton, and K. A. Kern. Tactile imaging: a method for documenting breast masses. In *Proceedings of the First Joint BMES/EMBS Conference. 1999 IEEE Engineering in Medicine and Biology 21st Annual Conference and the 1999 Annual Fall Meeting of the Biomedical Engineering Society*, volume 2, page 1131, 1999.

[105] J. Wendlandt. Milli robotics for endoscopy. Memo M94/7, UC Berkley ERL, January 1994.

[106] J. Wendlandt and S. S. Sastry. Design and control of a simplified stewart platform for endoscopy. In *Proceedings of the IEEE Conference on Decision and Control*, volume 1, pages 357–362, 1994.

[107] G. J. Wiet, R. Yagel, D. Stredney, P. Schmalbrock, D.J. Sessanna, Y. Kurzion, et al. A volumetric approach to virtual simulation of functional endoscopic sinus surgery. In K. S. Morgan et al., editors, *Medicine Meets Virtual Reality: 5*, pages 167–179, Amsterdam, 1997. IOS Press.

[108] J. Yan and S. E. Salcudean. Teleoperation controller design using H-infinity optimization with application to motion-scaling. *IEEE Transactions on Control Systems Technology*, 4(3):244–258, May 1996.

[109] Y. Yokokohji and T. Yoshikawa. Bilateral control of master-slave manipulators for ideal kinesthetic coupling—formulation and experiment. *IEEE Transactions on Robotics and Automation*, 10(5):605–620, October 1994.

[110] K. Zhou, J. C. Doyle, and K. Glover. *Robust and Optimal Control*. Prentice-Hall, Inc., New Jersey, USA, 1996.

[111] Y. Zhuang and J. Canny. Haptic interaction with global deformations. In *Proceedings of the IEEE International Conference on Robotics and Automation (ICRA 2000)*, pages 2428–2433, 2000.

[112] C. B. Zilles and J. K. Salisbury. A constraint-based god-object method for haptic display. In *Proceedings of the IEEE/RSJ International Conference on Intelligent Robots and Systems (IROS'95)*, pages 146–151, 1995.